# CORROSION FATIGUE OF ENGINEERING ALLOYS IN AQUEOUS ENVIRONMENTS

by

Brian Dudley Harty



A thesis submitted to the Faculty of Engineering, University of Cape Town in fulfilment of the degree of Doctor of Philosophy.

Department of Materials Engineering
University of Cape Town

December 1989

# CORROSION FATIGUE OF ENGINEERING ALLOYS IN AQUEOUS ENVIRONMENTS

by

Brian Dudley Harty

A thesis submitted to the Faculty of Engineering, University of Cape Town in fulfilment of the degree of Doctor of Philosophy.

Department of Materials Engineering
University of Cape Town

December 1989

# ACKNOWLEDGEMENTS

I wish to express my appreciation to the following people who have assisted me during this research project:

My supervisor, Prof. A. Ball, and my co-supervisor, Mr. R.E.J. Noel, for their advice and support.

Mrs. Helgard Bohm, Mrs. Sue Betz and Mrs. Penny Park-Ross for their assistance and co-operation in the laboratory and in the final preparation of the manuscript. Miss Linda Charteris for her typing assistance and moral support.

Mr. Nick Dreze and Mr. Glen Newins for their technical assistance. Mr. Bernard Greeves and Mr. James Peterson for photographic assistance.

The staff and fellow students for their support and encouragement.

The CSIR and the Chamber of Mines Research Organisation are gratefully acknowledged for the provision of research bursaries and project support.

This thesis was based on the results of the collaborative programme of work undertaken as part of the research and development programme of the Research Organisation of the Chamber of Mines of South Africa.

# ABSTRACT

A comparative study of the fatigue crack growth rate (FCGR) behaviour of five alloys in air and in aqueous environments has been performed. The alloys tested include: mild steel as a reference material, a corrosion resistant dual phase steel, 3CR12, a proprietary martensitic stainless steel, AISI 431, a newly developed 8% Cr martensitic steel, Alloy 825, and a newly developed corrosion-abrasion resistant metastable austenitic alloy, 1210. Tests were conducted in laboratory air, distilled water at rest potential, 500 ppm chloride solution at rest potential, 1000 ppm chloride solution at rest potential, and 1000 ppm chloride solution at -1200 mV sce; solution temperatures were maintained at 25°C.

Crack growth rate tests were performed using sinusoidal loading at a load ratio R=0.1, a frequency of 3Hz in the laboratory air, and a frequency of 1 Hz in the aqueous environments. At the completion of testing, fracture surfaces were studied using a scanning electron microscope.

In air, the mild steel and 3CR12 display comparable rates of cracking and exhibit a greater resistance to fatigue crack propagation than the martensitic AISI 431 and Alloy 825; Alloy 825 shows the least resistance to fatigue crack propagation. The deformation induced transformation in 1210 gives this alloy the greatest resistance to fatigue crack propagation in air.

Fatigue crack growth rates were all enhanced in the aqueous environments. The greatest overall rate of environmentally assisted cracking was shown by alloy 825 while the lowest was shown by the mild steel. Although the rate of cracking of 1210 in the aqueous environments was less than that of Alloy 825, 1210 was influenced the most by the aqueous environments. An environmentally assisted cracking index shows that the rate of fatigue crack propagation in 1210 is increased by 32 times in the 500 ppm chloride solution at low stress intensities. The fatigue crack growth rates of mild steel and AISI 431 were significantly influenced by the cathodically polarised conditions in the 1000 ppm chloride solution, compared to the rest potential conditions. In these cases hydrogen was seen to be evolved from the specimen surfaces.

Changes in the fatigue crack growth rate behaviour were accompanied by changes in the fracture surface morphologies. The observed changes varied for each alloy and for each environment, and were manifest by the degree of intergranular cracking,

cleavage, quasi cleavage, and increased coarseness of the transgranular cracking. The fracture surface morphologies are reported and discussed in detail.

In general, the fracture surface morphologies could be directly related to the relative degrees of environmental influence on the rate of cracking; results are explained in terms of existing hypotheses. It is suggested that the environmentally assisted cracking of mild steel and AISI 431 at cathodic potentials in the 1000 ppm chloride solution could only be attributed to hydrogen assisted cracking. Similarly, it is suggested that the large crack growth rate acceleration of 1210 in the aqueous environments could also be attributed to hydrogen. The similar fracture surface morphologies observed on the other specimens after tests in the aqueous environments suggests that hydrogen could be responsible for the environmentally assisted cracking of all the steels in aqueous environments.

# NOTATION AND ABBREVIATIONS

| | |
|---|---|
| a | Crack length |
| a/W | Crack aspect ratio |
| $A^*$ | Normalised back face strain |
| B | Specimen thickness |
| b.c.c. | Body centred cubic |
| BFS | Back face strain |
| COD | Crack opening displacement |
| cpm | Cycles per minute |
| CT | Compact tension |
| da/dN | Crack growth rate |
| E | Young's modulus |
| EAC | Environmentally Assisted Cracking |
| f.c.c. | Face centred cubic |
| FCGR | Fatigue crack growth rate |
| K | Stress intensity factor |
| $K_{max}$ | Maximum stress intensity factor |
| $K_{min}$ | Minimum stress intensity factor |
| $K_c$ | Critical stress intensity/Fracture toughness |
| $K_{eff}$ | Effective stress intensity factor |
| $K_{cl}$ | Closure stress intensity factor |
| $K_{ISCC}$ | Threshold stress intensity for SCC |
| $K_{IC}$ | Plane strain fracture toughness |
| $\Delta K$ | Stress intensity factor range |
| $\Delta K_{th}$ | Threshold stress intensity factor range |
| $\Delta K_{eff}$ | Effective stress intensity factor range |
| N | Number of cycles. |
| $N_f$ | Number of cycles to failure |
| P | Load |
| $P_{open}$ | Load at which crack opens |
| $P_{min}$ | Minimum load |

| | |
|---|---|
| $\Delta P$ | Load range |
| ppm | Parts per million |
| PSB | Persistent slip band |
| $r_p$ | Plastic zone size |
| R | Load or stress ratio |
| S | Alternating stress |
| sce | Saturated calomel electrode |
| SEM | Scanning electron microscope |
| UTS | Ultimate tensile stress |
| W | Specimen width |
| Y | Geometrical factor |
| $\epsilon_{max}$ | Maximum strain |
| $\epsilon_{min}$ | Minimum strain |
| $\nu$ | Cyclic frequency. |
| $\sigma$ | Applied stress |
| $\sigma_m$ | Mean stress |
| $\sigma_{ys}$ | Yield stress or proof stress |

# CONTENTS

# CHAPTER 1

# INTRODUCTION

It has long been recognised that the profitability and productivity of the gold mining industry in South Africa could be improved by mechanising the stoping operation. A programme to mechanise the stoping methods was initiated by the Chamber of Mines more than a decade ago [1]. One of the issues considered was the choice of a power system for the stoping machinery. Hydraulic power was recognised as an efficient alternative to the traditional compressed air and electrical systems which were inefficient and required high levels of maintenance. However, the use of hydraulic mineral oils was discounted because of the high cost of the fluid, the aggressive nature of the mining environment, and the possible contamination of the ore resulting from fluid leakage. Instead, attention was focused on the use of oil-water emulsions (typically 5% additive in 95% water) as a fluid medium with the ultimate aim of using plain water [2].

It was recognised that long-term benefits could be gained from using high pressure water to power hydraulic machinery, since a system for transporting mine service water used for cleaning blasted faces, dust suppression, and cooling of deep mines was already in existence. The, so called, hydro-power involves the use of the hydrostatic pressure in a water column at the bottom of a deep shaft for driving stoping machinery. The main advantage of the hydro-power system is that only one reticulation system for the cooling of deep mines and the provision of power is required.

The use of high pressure water as a single power and service medium is novel and thus some initial difficulties are anticipated. It has brought about the need to develop suitable water powered devices such as rockdrills, impact hammers, stope cleaning water jets, and hydraulic props [3,4]. This approach to mining and has also necessitated research into the behaviour of engineering materials in underground environments.

Underground conditions are harsh. It has been reported [5] that corrosion rates in stoping areas are generally greater than elsewhere underground and often worse than marine and industrial environments. A survey of the mine service water has shown that the composition of the water varies widely from one mine to another. Variations were also detected in water samples at various points in one mine as well

as samples taken from a single point at different times [6]. The four main factors influencing rates of corrosion are temperature, humidity, blasting fumes, and the poor quality of mine service waters. As service water is recirculated in the mine the quality deteriorates progressively with an increase in the concentration of dissolved solids, especially chloride and sulphate ions. Furthermore, the water becomes contaminated with fine particles of quartz rock with a Vickers hardness of around 1100, providing an abrasive element to the problem. Hydro-powered stoping machinery would be exposed to these harsh conditions both externally and internally.

Early research was focused on the abrasive wear behaviour of materials in these environments and concluded that the abrasion problem was compounded by corrosion and, in fact, corrosion-abrasion wear was found to be the major factor contributing to the deterioration of mining equipment [7]. There are two means to reduce the deterioration of mining machinery in the aggressive environments at the stopes. Firstly, the quality of the mine service water can be controlled and, secondly, appropriate corrosion and wear resistant materials can be used.

The improvement of the quality of the large volumes of service water used in the mines is an important aspect of the research programme and has led to the formulation of guidelines for hydro-power mine water concentrations. Common water treatment practices include [8]: i) biocidal treatment, ii) water conditioning for neutralisation and clarification, iii) anti-fouling to reduce scaling, iv) addition of corrosion inhibitors, and v) filtration of abrasive solid particles. The feasibility of using desalination processes to reduce the amount of dissolved solids in mine waters has been considered [9]. One method, freeze desalination, is particularly advantageous since it also provides ice for cooling the environment in deep level mines [10].

From the investigation of commercially available engineering alloys it was discovered that proprietary abrasion resistant alloys were not suitable for use in all situations [11]. The corrosion resistant 3CR12 steel proved to be useful in that it fulfilled many of the requirements, but still had limited applications because of unsatisfactory wear resistance. The use of stainless steels was considered to be impractical because they are expensive and often do not possess the necessary anti-abrasive properties for use in underground machinery. Consequently, it became necessary to consider the development of a range of economical engineering alloys with the right combinations of strength, toughness, corrosion resistance, and wear resistance. This brought about the initiation of a programme for the development of improved materials specifically for use in the South African gold mining industry.

Research has indicated that attention must be given to developing a microstructure which has the ability to accumulate strain produced under abrasive wear conditions,

which in turn promotes a high resistance to particle indentation and scratching [12]. A microstructure which was considered to possess the necessary properties is a dual phase consisting of about 95% martensite and 5% retained austenite [13]. This led to the development of Alloy 825, an alloy containing 8% chromium, for corrosion resistance, and 5% retained austenite at martensite lath boundaries, to impart toughness. Note that this alloy should not be confused with a North American nickel based alloy of the same designation. Another microstructure possessing the ability to accumulate strain was recognised as that of the metastable stainless steels which can develop high hardness while maintaining good toughness, but these were not considered to economically viable. This led to the development of a corrosion resistant metastable austenitic alloy, designated 1210 [14-16]. Brief overviews of the development of corrosion-abrasion resistant steels for use in the gold mining industry are given by Protheroe et al [17] and Metcalfe et al [18].

As a result of continuous exposure of mining machinery to the aggressive mine waters, and the working internal and external stresses, it is reasonable to assume that phenomena such as stress corrosion cracking and corrosion fatigue may be a problem. This reasoning, plus the need to fully characterise the alloys, has promoted the investigation of the corrosion fatigue and stress corrosion behaviour of the recently developed alloys, and to compare this to the behaviour of materials currently in use underground .

This thesis reports the investigation of the corrosion fatigue crack growth rate behaviour of mild steel, corrosion resistant 3CR12, proprietary AISI 431, and two recently developed engineering alloys, namely Alloy 825 and 1210. The primary aim was to compare the fatigue crack growth rate behaviour of these steels in a series of aqueous environments. Owing to the complex nature of mine waters, the specific influence of chloride ions on the rate of cracking has been investigated. Tests were to be performed in distilled water with additions of chloride up to a concentration of 1000 ppm, which was expected to comply to guidelines for mine service water quality.

# CHAPTER 2

# LITERATURE REVIEW

## 2.1 METALLIC FATIGUE

### 2.1.1 Introduction

Metallic fatigue can be defined as the progressive deterioration of a metal due to alternating or repeated stresses that may be well below the macroscopic yield strength of the metal. Fatigue cracking is often insidious and may only become evident when failure occurs.

The fatigue process can generally be characterised by two stages [19]: stage I, initiation, and stage II, crack propagation (fig. 2.1). So called stage I growth features microcracks oriented at around 45° to the maximum principal stress. During stage II growth, the plane of the crack is normal to the direction of the maximum tensile stresses. The stage I to stage II transition is generally considered to result from the reduction in the ratio of shear to direct stress at the crack tip, as it moves from the weakly constrained surface crystals into the interior where slip may be inhibited.

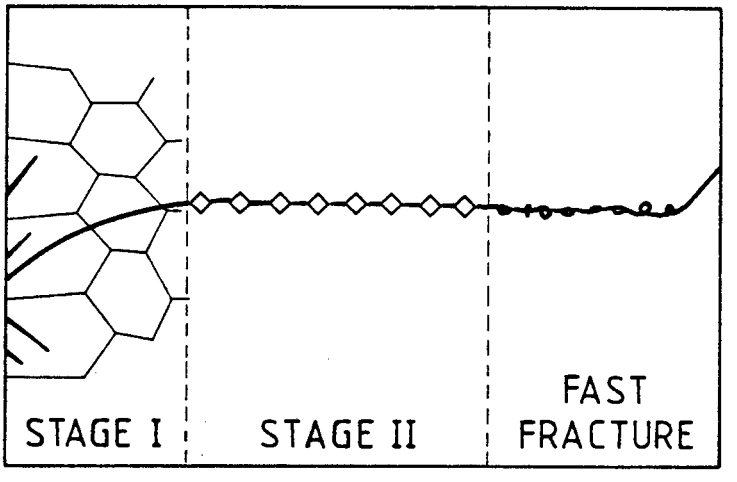


Figure 2.1 Schematic illustration of the various stages of fatigue (after Tomkins [20]).

### 2.1.2 Fatigue Crack Initiation

Fatigue crack initiation is generally a surface phenomenon. Common nucleation sites are inhomogeneities at or near the metal surface. These inhomogeneities, which act as stress raisers, include second phase particles, such as inclusions and precipitates. Rough surface finish may also provide localised stress conditions for crack nucleation. In addition, design often incorporates complex sections which give rise to complex states of surface stress which may initiate fatigue.

In engineering components, especially those containing welds, cracks may originate from internal or surface defects. These defects may lead directly to stage II crack growth, bypassing the slower stage I process, i.e. the defects behave as embryo cracks. In the absence of surface stress concentrators, initiation may occur by any one of a number of hypothetical mechanisms. The most widely accepted mechanism is that of fatigue slip band type nucleation, involving the formation of extrusions and intrusions [21-23].

During the tensile ramp of a load cycle, dislocation slip occurs on a favourably oriented slip plane. On load relaxation, slip occurs on a parallel plane, since slip on the first plane is inhibited by strain hardening. These slip bands are often referred to as persistent slip bands (PSBs). The presence or creation of slip steps on the surface of a metal acts to localise or concentrate the stress and facilitate the formation of PSBs [24]. The dislocation motion within the whole PSB is not fully reversible and leads to the formation of surface extrusions and intrusions (fig. 2.2). There exists a lot of documented evidence which supports the formation of a unique surface topography as a consequence of cyclic stressing that facilitates the

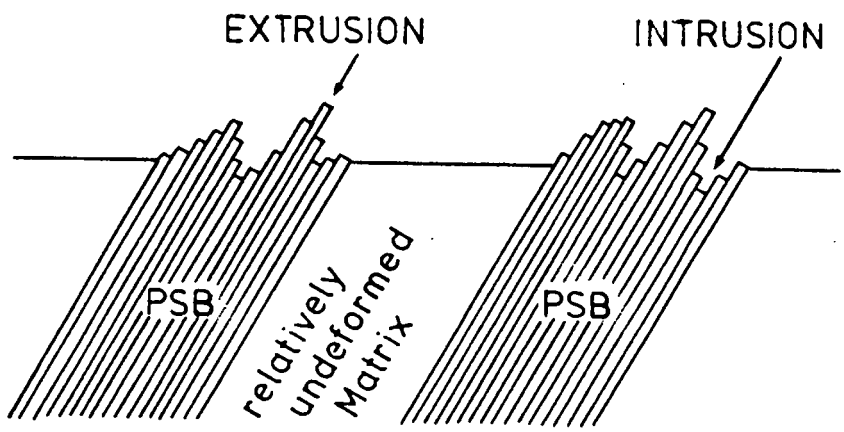


Figure 2.2 Schematic representation of extrusions and intrusions formed at PSBs (after Ewalds and Wanhill [27]).

nucleation of microcracks. The model assumes that the formed intrusions act as stress raisers and promote further slip at the intrusions during subsequent cycles. This leads to the formation of microcracks. In support of the model, it has been shown that microcracks are associated with sharp intrusions, and that they follow the primary slip plane [25]. Present models for the development of extrusions and intrusions are qualitative in that they do not account for dislocation impedance in polycrystalline materials. The emergence of extrusions and intrusions are dependent on the formation of slip bands which in turn are influenced by metallurgical defects [26].

### 2.1.3 Fatigue Crack Propagation

At ambient temperatures, and in the absence of aggressive environments, stage II fatigue crack growth generally occurs transgranularly by a mechanism of reversed slip. A number of models have been proposed to explain stage II cracking, one of which is the plastic blunting process model first suggested by Laird and Smith [28] and subsequently modified by Laird and co-workers [29,30].

This model, described in fig. 2.3, shows an initially sharp crack loaded in tension. Shear deformation is concentrated at the planes of maximum shear stress, which are at an angle of 60-70° to the crack plane (fig. 2.3a). With increasing tensile stress, the crack tip becomes rounded, and 'ears' form in the apex of the rounded region (fig. 2.3c). On compression, the rounded off crack comes to a sharp point by complete closure of the two crack surfaces. The deformation 'ears' close up and form the microcracks or troughs of the fractographic ripples, referred to as striations.

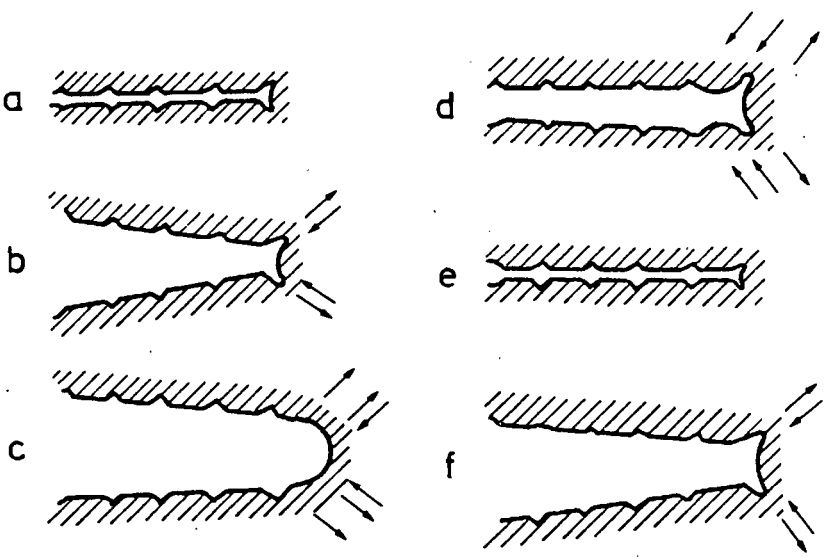


Figure 2.3 Schematic of stage II crack propagation (after Laird [29]).

The deformation produced at the crack tip during each tensile cycle results in the extension of the crack, and the resharpening of the crack tip on unloading ensures favourable conditions for continued crack growth.

The reversed slip mechanism, involving the opening and closing of a crack with the formation of 'ears', provides a good explanation of the formation of striations. This model confirms the one-to-one relationship between the number of striations and number of load cycles that has been observed by several workers [31,32]. Although it is generally accepted that each striation is formed during one cycle, under complex loading conditions there may be 'deaf' cycles, during which the crack does not propagate [33].

Forsyth et al [34] have identified two types of striation: ductile and brittle striations. Ductile striations lie on irregular non-crystallographic plateaux or planes whilst brittle striations lie on crystallographic facets. Garrett and Knott [35] suggest that brittle striations in aluminium alloys result from a similar process to that giving ductile striations, rather than the cleavage mechanism forwarded by Forsyth [19]. In addition, Laird [29] has cited a number of arguments against the possibility of cleavage being responsible for brittle striation formation.

Classic striations are not always observed on fracture surfaces (especially in ferritic and martensitic metals), even though the reversed slip mechanism may be in operation [36]. The morphology of fatigue striations differs widely [37] and depends on symmetry and number of available slip systems and the material strength level [38]; striation formation is favoured in f.c.c. materials because cross slip is more difficult than in b.c.c. materials. Since plastic deformation involves the generation and motion of dislocations, it is reasonable to expect that the dislocation behaviour at or near the crack tip influences the crack propagation behaviour [39]. In f.c.c. metals, cross slip is thought to be important in the development and propagation of fatigue cracks; f.c.c alloys of low stacking fault energies in which cross slip is difficult are more resistant to fatigue. Boettner [40] has shown a dependence of fatigue crack propagation rates on stacking fault energies.

Fatigue cracking may not always take place by the reversed slip mechanism. Cracking, especially in high strength steels, may occur by mechanisms of micro-cleavage, intergranular cracking or void coalescence. These alternative modes of crack propagation are thought to be environmentally controlled but may also be a function of microstructure and impurity element content [36].

### 2.1.4 Characterisation of Fatigue Behaviour

In the engineering context, the total fatigue life of a structural material is defined as the number of cycles to failure, $N_f$. This number is the sum of the cycles required for microcrack nucleation plus the cycles necessary to propagate this crack to an unstable size prior to failure.

Conventionally, fatigue behaviour has been characterised by the laboratory testing of plain specimens with the results presented in the form of an S-N curve. This curve represents the number of cycles to failure for a range of applied stresses (fig. 2.4).

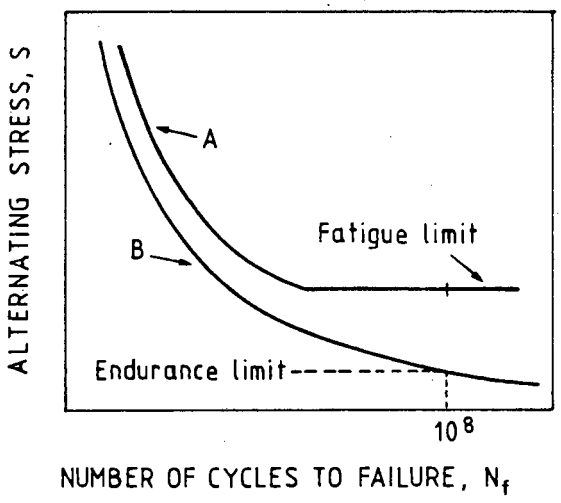


Figure 2.4 S-N fatigue curves showing two types of behaviour. Type A is typical of alloys which strain age and type B is typical of non-ageing alloys (after Knott [41]).

However, fatigue cracking in structural elements and large engineering components often originates from pre-existing manufacturing or fabrication defects, so that the major part, if not all, of the fatigue lifetime will be spent in propagating the crack. The S-N information obtained for smooth specimens (where initiation may account for up to 90% of the total fatigue life) is clearly not applicable under conditions of pre-existing flaws. The incidence of pre-existing flaws in engineering products has brought about extensive research into the **fatigue crack growth rate** (FCGR) behaviour of materials. Here, the analytical approach involves the use of fracture mechanics principles.

### 2.1.5 Fracture Mechanics Considerations in Fatigue Crack Propagation

Linear elastic fracture mechanics postulates a dependence of the macroscopic crack behaviour on the local characteristics at the crack tip. In the elastic solution, the stress and strain fields around the crack tip are fully described by the **stress intensity factor**, K. The local stress and strain fields are assumed to control the crack behaviour thus making the stress intensity factor the basis for describing the crack propagation behaviour. This means that the behaviour of a cracked body can be determined for arbitrary shape and for random geometry of externally applied forces. The practical importance lies in the fact that results obtained from laboratory specimens can be related to real engineering components of the same material, provided the relevant K calibration or geometrical factor is known.

In metals there is always a zone at the crack tip which undergoes plastic deformation. However, provided this region is small, the elastic solution may still give a good approximation of the behaviour of real cracks [42].

The stress intensity factor is given by:

$$K_I = Y\sigma\sqrt{\pi a}$$

where Y = geometrical factor,
$\sigma$ = applied stress,
a = crack length,
and the subscript I indicates a tensile opening mode.

In fatigue, the cyclic stress intensity factor is described by the stress intensity factor range, $\Delta K$:

$$\Delta K = K_{max} - K_{min}$$

where $K_{max}$ and $K_{min}$ are the maximum and minimum stress intensity factors respectively. $K_{min}$ is, by convention, taken as zero if the minimum load is compressive.

The characteristic dependence of the fatigue crack growth rate on the stress intensity factor range is represented schematically in fig 2.5, where the fatigue crack growth rate (da/dN) is the crack length increment per load cycle.

The change of da/dN with $\Delta K$ is sigmoidal. $\Delta K_{th}$ represents the threshold stress intensity, below which the crack is essentially non-propagating. Above this value the FCGR increases rapidly with increasing $\Delta K$ into region II, which is often

represented by a linear relationship between log da/dN and log ΔK. In region III the FCGR curve reaches an asymtotic value, $K_c$, which is a critical value of stress intensity, tending towards that of the fracture toughness of the material.

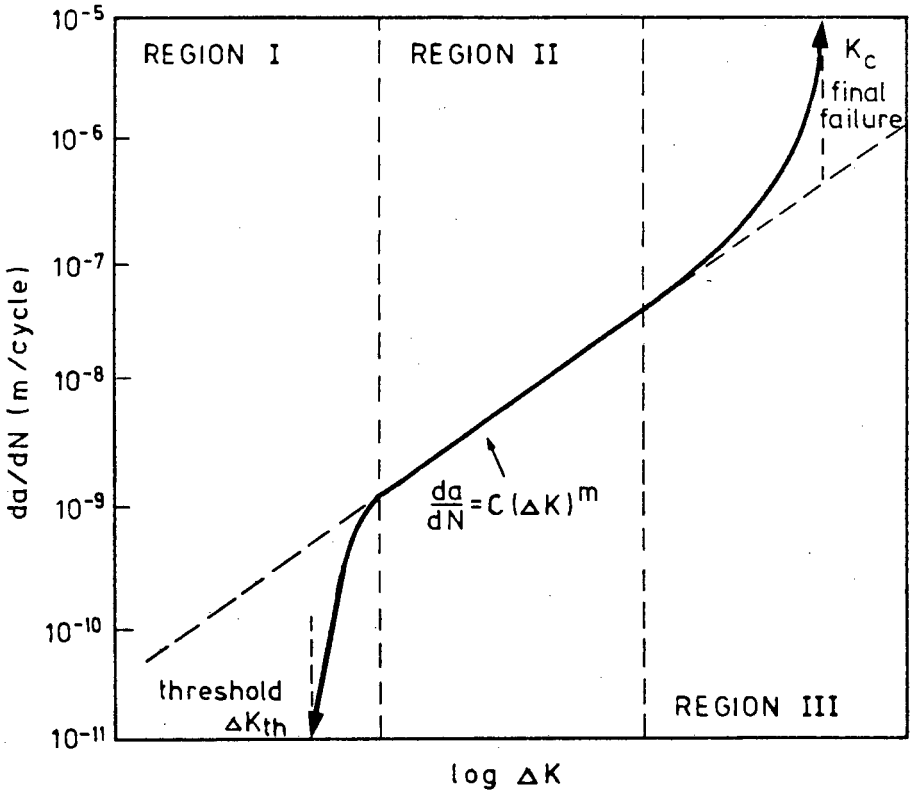


Figure 2.5 Schematic drawing of the log da/dN and log ΔK dependence.

The linear relationship of region II can be described by empirical formulae such as:

$$da/dN = C(\Delta K)^m \quad \text{- Paris equation [43]}$$

$$da/dN = \frac{C(\Delta K)^m}{(1-R)K_c - \Delta K} \quad \text{- Forman equation [44]}$$

where C and m are materials constants,

R = load ratio

$K_c$ = material fracture toughness

The Paris equation describes only the linear behaviour of region II, whereas the Forman equation describes the region II and region III behaviour as well as taking

into account the effects of load ratio on FCGRs. Richards and Lindley [36] have suggested that these simple relationships between da/dN and ΔK hold only for describing fatigue crack growth by striation mechanism and that variations in C and m result from changes in the crack growth mechanism.

### 2.1.6 Factors Affecting Fatigue Crack Initiation

#### 2.1.6.1 Surface conditions

Crack initiation is a surface related phenomenon and, as a result, fatigue strength is largely dependent on surface conditions such as finish, hardness, and residual stresses. In general; i) fatigue strength decreases with an increase in surface roughness due to the stress concentration effect at sharp geometrical discontinuities, ii) surface hardening inhibits the microplastic deformation processes thought to initiate fatigue, and iii) residual compressive stresses tend to offset the damaging effect of applied tensile stresses.

#### 2.1.6.2 Loading conditions

For a given material at a given stress amplitude, the fatigue life of the material will decrease with an increase in the mean stress level (fig. 2.6). The effect of mean stress can be predicted in two ways; i) specific testing to obtain S-N curves, or ii) the use of empirical relationships, such as the Goodman, Gerber or Soderberg models.

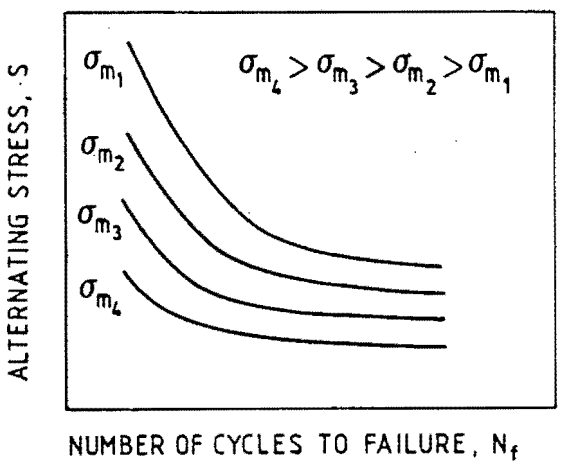


Figure 2.6 Schematic representation of the dependence of fatigue life on the mean stress, $\sigma_m$ (after Hertzberg [45]).

In an inert environment at ambient temperatures, the fatigue limit of a material is expected to remain uninfluenced by changes in frequency. However, at testing speeds greater than 200 Hz, the fatigue limit of a material may increase [46,47].

#### 2.1.6.3 Environment

Exposure to aggressive environments generally decreases the resistance of a material to fatigue crack initiation; aqueous environments have been shown to incur the most severe effect. Possible mechanisms of crack initiation in aqueous environments include [24]: i) assistance with the formation of persistent slip bands, ii) the formation of pits by localised dissolution, iii) destruction of thin, protective oxide films which may result in electrochemical activity, iv) electrochemical attack at plastically deformed regions of the metal, and v) the reduction of surface energy by the adsorption of an aggressive ionic species.

The extent of the influence that an environment has on the fatigue crack initiation behaviour of a metal is dependent on the complex interaction between mechanical, chemical and metallurgical factors. A recent review by Srivatsan and Sudarshan [48] deals with the subject of fatigue crack initiation in greater detail.

### 2.1.7 Factors Affecting Fatigue Crack Propagation

#### 2.1.7.1 Loading conditions

Pook [49] has suggested that, in most steels at ambient temperatures and in inert environments, stage II FCGRs are largely independent of factors such as mean stress, waveform and frequency. This is true for propagation rates associated wholly with striation formation. Note that the mean stress is usually expressed in terms of R, where R is the stress ratio and is the quotient of the minimum and maximum stresses in the load cycle. Richards and Lindley [36], and Ritchie and Knott [50] have shown that R does have an effect on FCGRs when additional modes of fracture occur during the fatigue process. Barsom [51] investigated the effect of the cyclic waveform on the rates of fatigue crack propagation of a maraging steel in a room temperature air environment and concluded that there was no effect.

#### 2.1.7.2 Thickness

A two dimensional theoretical model predicts that thickness will influence FCGRs. The plastic zone size can be given by the following equations:

$$\text{Plane stress: } r_p = 1/2\pi\,(K/\sigma_{YS})^2$$

$$\text{Plane strain: } r_p = 1/6\pi\,(K/\sigma_{YS})^2$$

This suggests that the plastic zone size in the plane stress condition is three times larger than that in the plane strain condition. The specimen surface is always in a state of plane stress, while the interior tends to be in a state of plane strain; plane stress conditions will prevail in thin specimens whilst the plane strain conditions will prevail in thicker sections. This argument leads to an expected dependence of FCGR on specimen thickness. Contrary to theoretical predictions, it has been shown that, if growth occurs by striation mechanism, there is a negligible influence of thickness on FCGR [52]. Richards and Lindley [36] have shown that an increase in FCGRs results from an increase in thickness of a 1% carbon pearlitic steel, but they attributed this increment to an increase in the incidence of microcleavage resulting from greater constraint. Reviewing diverse results, Klesnil and Lucas [25] deduced that an influence of thickness on FCGRs may be expected mainly for thin specimens and for high amplitude loading. They also suggest that the thickness effect disappears in specimens with a thickness exceeding 10 mm.

#### 2.1.7.3 Inclusions

The effect of inclusions on the rate of propagation may depend on the number of inclusions and on the extent of the voids generated by these inclusions. Barbangelo [53] has shown that inclusions have the greatest influence on subcritical crack propagation at high alternating stress intensities. The higher stress concentrations may cause particles in front of the crack to cleave or loose cohesion with the matrix, thus initiating larger voids. The remaining material between the void and the crack tip may now rupture, producing a localised jump of the crack front [31].

#### 2.1.7.4 Crack closure

The concept of crack closure was first introduced by Elber [54]. This was recognised as plasticity induced closure, where the plastic deformation in the wake of a growing fatigue crack interferes with subsequent opening and closing cycles. Since the crack cannot propagate whilst it is physically closed, the stress intensity range at the crack tip is reduced to some effective value, $K_{eff}$, given by the equation:

$$K_{eff} = K_{max} - K_{cl}$$

where $K_{max}$ is the maximum stress intensity and $K_{cl}$ is the stress intensity at which the crack closes.

Three main closure mechanisms have been identified by Suresh and Ritchie [55] and are represented schematically in fig. 2.7; i) plasticity induced closure is operative over the whole of the FCGR curve and is more evident in conditions of plane stress, ii) oxide induced closure results from a wedging effect of the oxides formed inside the crack in aggressive environments. Since the thickness of the oxide layers will be small, this mechanism is generally expected to be operative at small crack tip opening displacements in the near threshold region of the FCGR curve, iii) roughness induced closure results from the wedging effect of fracture surface asperities. This mechanism is again expected to be most evident at small crack tip opening displacements.

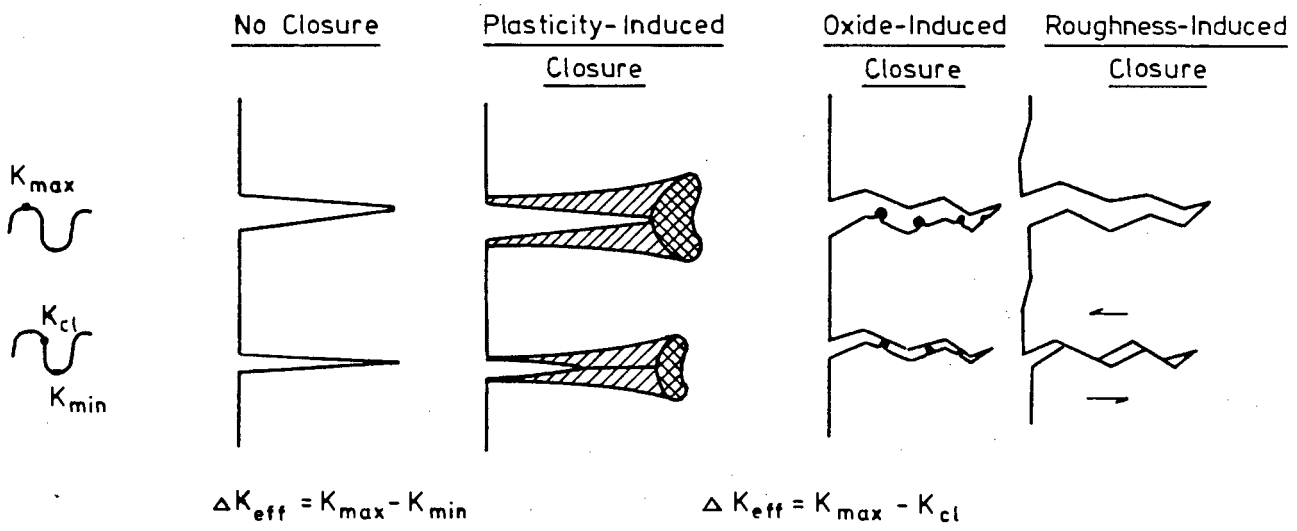


Figure 2.7 Schematic illustration of the mechanisms of fatigue crack closure (after Suresh and Ritchie [55]).

More recently, the term crack closure has given way to one of crack tip shielding which is recognised as a mechanism of extrinsic toughening. Mechanisms identified in this respect are illustrated in fig. 2.8 and a comprehensive review on crack tip shielding in fatigue is given by Ritchie in reference 56.

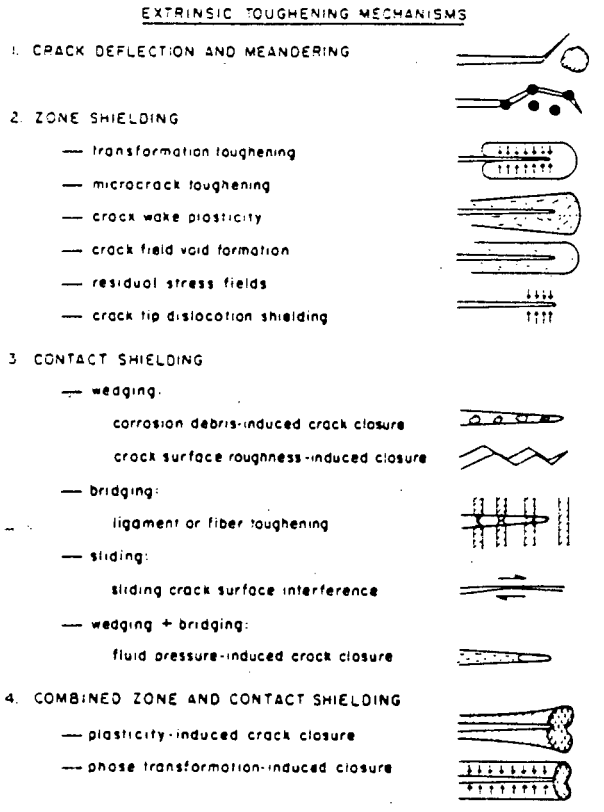


Figure 2.8 Schematic representation of the classes and mechanisms of crack tip shielding (after Ritchie [56]).

### 2.1.7.5 Environment

The effect of environment on FCGRs is extremely complex and will be covered separately, and in some detail, in the section on environmentally assisted cracking of metals.

## 2.2 ENVIRONMENTALLY ASSISTED CRACKING IN METALS

Many engineering components and structures are subjected to corrosive environments as well as the stresses and strains, for which they are designed. The propagation of cracks in metals may be assisted by the environment giving rise to the well known phenomena of corrosion fatigue, stress corrosion cracking and hydrogen embrittlement, jointly referred to as **environmentally assisted cracking** (EAC). The phenomenon of EAC results from the complex interplay of

mechanical, microstructural and environmental factors. In addition there may be an interaction of the various phenomena (fig 2.9) [57]. This section will focus on the EAC of metals in aqueous environments and will provide the basis of the arguments used in the discussion. Once again, the effects of temperature and variable amplitude loading will be omitted for the sake of brevity.

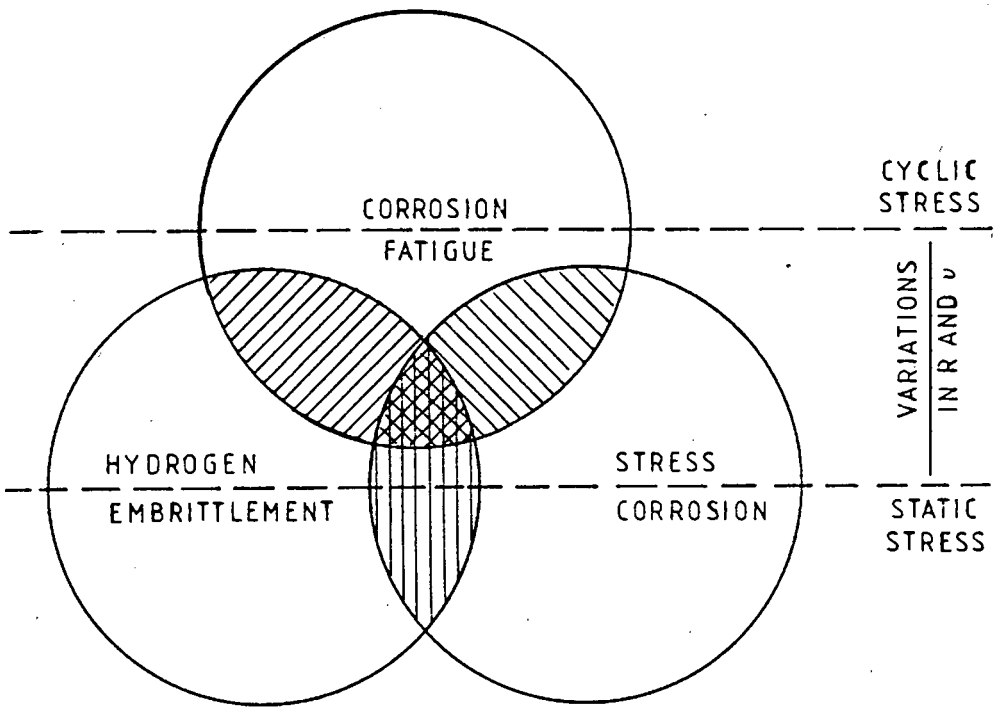


Figure 2.9 The interaction of cracking modes under static and cyclic loading (after Ford [57]).

### 2.2.1 Introduction

Corrosion fatigue results from the synergistic action of a corrosive environment and cyclic stresses. Data is generally compared against results obtained in air although laboratory air may not, in reality, constitute an inert environment. Many researchers have shown FCGRs in air to be accelerated with respect to data obtained in dry, inert gases (e.g. Argon) or in vacua. For example Stewart [58] observed FCGR rates of a 2NiCrMoV steel to be three times faster in air than in a vacuum, at low $\Delta K$ levels. Atkinson and Lindley [59] observed rates three to six times faster in air compared to data obtained in vacuum for an En56C steel.

Corrosion fatigue has often been classified, somewhat arbitrarily, according to whether $K_{max}$ is below or above $K_{ISCC}$ [60-63], where $K_{ISCC}$ is the stress intensity

level, below which, no significant stress corrosion cracking will occur under sustained loading. The EAC process in high strength steels may be broadly characterised by three different types of behaviour, represented schematically in fig. 2.10 [64].

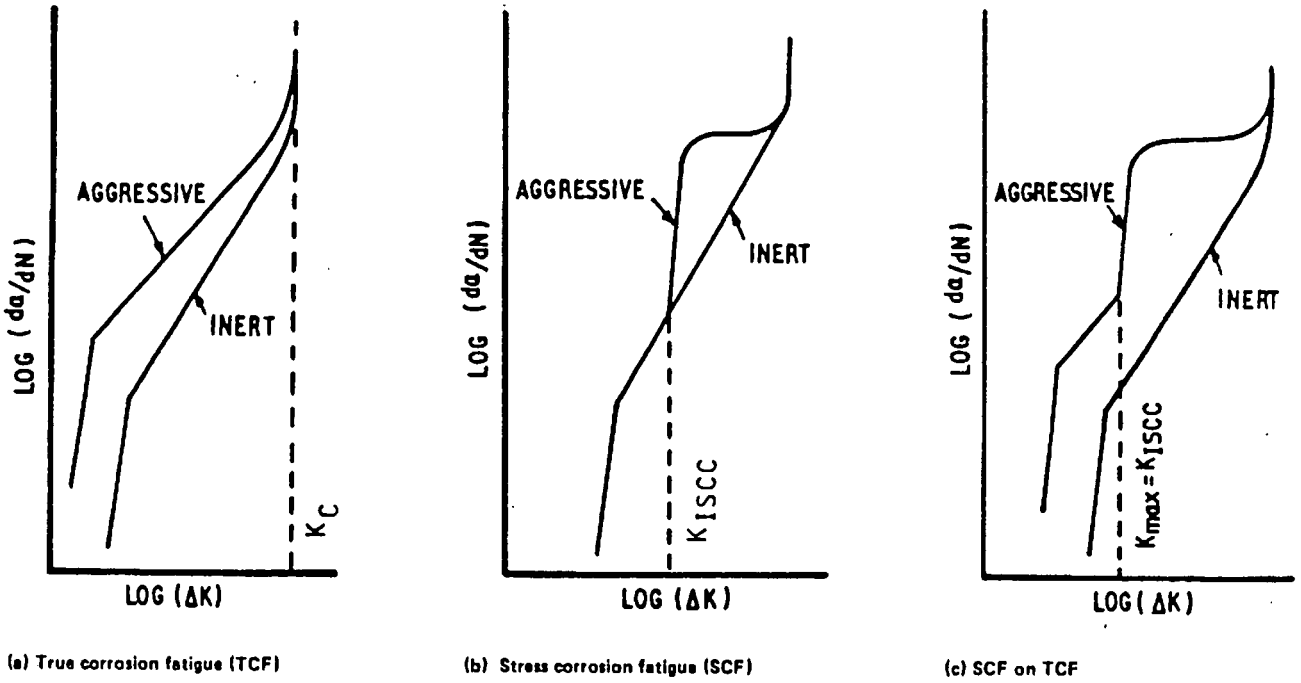


Figure 2.10 Schematic illustrations of the basic types of corrosion fatigue crack growth behaviour (after McEvily and Wei [64]).

(a) True corrosion fatigue: identifies the behaviour where FCGRs are enhanced by the presence of an aggressive environment through the synergistic action of corrosion and cyclic loading. The environmental effect is illustrated by a decrease in the apparent threshold stress intensity, $K_{th}$ (see fig. 2.5) and an increase in the rate of crack growth at given levels of K below $K_c$. As K approaches $K_c$, the mechanical component overshadows any effect of the environment as a result of the rate limiting nature of corrosion processes. This is essentially 'below $K_{ISCC}$' behaviour, and applies to materials which do not stress corrode, i.e. $K_{ISCC} \geq K_{IC}$.
(b) Stress corrosion fatigue: describes systems where there is a substantial environment enhanced sustained load crack growth component under fatigue conditions, which can only occur whenever the stress intensity in the cycle is above $K_{ISCC}$.
(c) Stress corrosion fatigue and True corrosion fatigue: indicates the most common type of behaviour which pertains to systems exhibiting stress corrosion fatigue above $K_{ISCC}$ and also true corrosion fatigue at all levels of stress intensity.

The separation point for the classification of corrosion fatigue in terms of below and above $K_{ISCC}$ behaviour cannot be taken literally because of the strain rate sensitivity of $K_{ISCC}$. The $K_{ISCC}$ value, commonly determined under fixed load conditions, can be expected to be reduced under cyclic straining. It is therefore not to be taken as a material constant for any particular alloy/environment system

### 2.2.2 Electrochemical Reactions Within a Crack

According to Scott [65], the formation of slip steps at the tip of a stressed crack gives rise to a band of active metal surface. In aqueous solutions the fresh metal surface reacts with the environment setting up an electrochemical reaction. Portions of the active surface may dissolve and pass into solution:

$Fe \rightarrow Fe^{2+} + 2e^-$ (anodic reaction)

A corresponding cathodic reaction must take place at local cathodic sites. The two most common cathodic reactions in aqueous solutions are the reduction of dissolved oxygen to hydroxyl ions or the reduction of hydrogen ions to atomic hydrogen:

$\frac{1}{2}O_2 + H_2O + 2e^- \rightarrow 2OH^-$ (Oxidation Reduction Reaction)

or

$H^+ + e^- \rightarrow H$ (adsorbed) (Hydrogen Evolution Reaction)

If chloride ions are present in solution, they migrate toward the crack tip and react with the metal ions in solution:

$Fe^{2+} + 2Cl^- \rightarrow FeCl_2$ (insoluble)

$FeCl_2 + 2H_2O \rightarrow Fe(OH)_2 + 2HCl$

The acid produced in the reaction enhances the acidity of the solution which will further favour the hydrogen evolution reaction. The presence of chromium ions can also have a significant effect on the pH within a crack:

$2Cr + 3H_2O \rightarrow Cr_2O_3 + 6H^+ + 6e^-$ [66]

$Cr \rightarrow Cr^{3+} + 3e^-$

$Cr^{3+} + H_2O = Cr(OH)^{2+} + H^+$ [67]

The hydrogen atoms produced can combine to form molecular hydrogen or may be adsorbed onto the metal surface and diffuse into the metal. This would suggest that chromium containing steels are more susceptible to hydrogen cracking.

### 2.2.3 Factors Affecting Corrosion Fatigue

In general, the following factors may be responsible for accelerated crack propagation [68]:

1. Cathode reactions in the crack:

$$e^- + H^+ \rightarrow H$$
$$Ze^- + M^{z+} \rightarrow M$$

where rates will depend on reaction kinetics and reactant concentrations.

2. Anodic reactions in the crack:

$$M \rightarrow M^{z+} + Ze^-$$

where rates will depend on reaction kinetics, amount of reactive phase (e.g. hydride) and size of plastic zone (deformed material acts as the anode).

3. Crack tip stress field, which is dependent on five factors:

- Stress intensity
- Plastic zone size
- Ratio of triaxial stress component
- Load ratio
- Crack length

and the crack tip stress field in turn affects hydrogen solubility and diffusivity.

Cracking processes, which are influenced by a deleterious environment, are time dependent and these phenomena are governed by a number of factors. The processes which enhance the rate of crack growth of metals in hydrogen or hydrogenous gases (such as water vapour) have been identified by Wei and co-workers [69] and are illustrated schematically in fig. 2.11. They are as follows:

1. Transport of the gases to the crack tip.
2. Reactions of the gas or the gases with newly produced crack surfaces to evolve hydrogen (physical and dissociative chemical adsorption).
3. hydrogen entry (or absorption).

4. Diffusion of hydrogen to the fracture or embrittlement site.
5. Partitioning of hydrogen among the various microstructural sites.
6. Hydrogen-metal interactions leading to embrittlement.

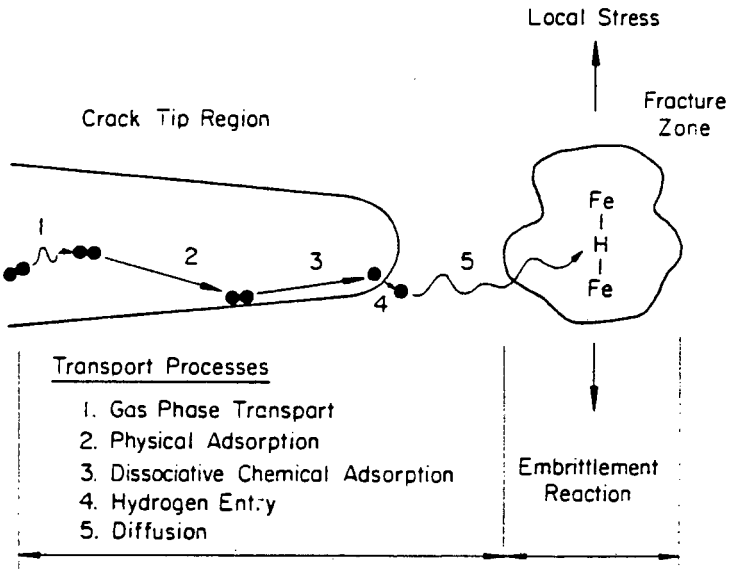


Figure 2.11 Schematic of the various processes involved in embrittlement of ferrous alloys by external environments (after Wei et al [69]).

For aqueous environments, the first step in the sequence is replaced by mass transport of the fluid or transport of the various species (such as chloride ions) in the electrolyte. The second step is replaced by the reactions of the newly created crack surfaces with the electrolyte [70]. Should hydrogen embrittlement be responsible for assisting crack growth in aqueous environments, this step serves as the hydrogen source and the sequence continues from step 3 of the gaseous environment processes; should anodic dissolution be responsible, this step will directly assist crack growth.

Any one of these steps may be rate determining. Furthermore, the rate determining step may change with crack length, i.e. at short fatigue cracks, the electrochemical reaction may determine the degree of enhancement, whereas at long fatigue cracks, the mass transport of the deleterious environment may be rate determining.

### 2.2.3.1 Load conditions.

In general, FCGRs are increased with a decrease in cyclic load frequency. This is shown clearly in fig. 2.12 which represents Barsom's data [60] for a 12Ni-5Cr-3Mo steel tested in 3% sodium chloride solution. The results show a marked increase in FCGRs with a change in frequency from 600 to 60 cpm. The effect results from the time dependence of corrosion fatigue; at low frequency loading, FCGRs are accelerated in the presence of aqueous environments simply because there is sufficient time per cycle for the environment to react with the material at the crack tip. Stewart [58] studied the influence of cyclic frequency on the EAC of a 2NiCrMoV rotor steel in hydrogen and showed that the degree of FCGR enhancement is at a maximum for frequencies between 0.1 and 1 Hz. Data of Atkinson and Lindley [59] show a maximum enhancement of about five times at a frequency of approximately 0.03 Hz for an A533B steel at 90°C in distilled water.

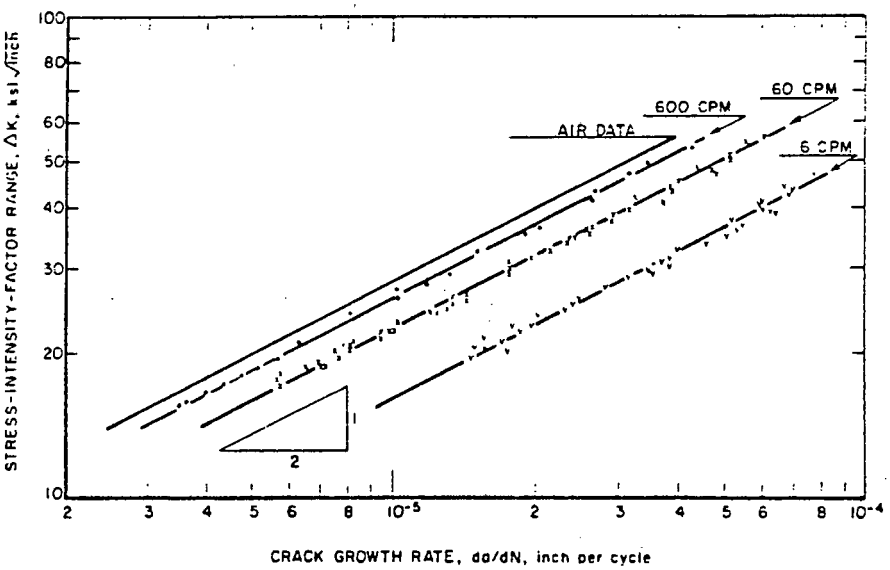


Figure 2.12 Corrosion fatigue crack growth data as a function of test frequency (after Barsom [60]).

In another study, Barsom [51] investigated the effect of waveform on the below $K_{ISCC}$ corrosion fatigue behaviour of a 12Ni-5Cr-3Mo steel. This study showed that sinusoidal, triangular, and positive sawtooth waveforms had an identical influence on FCGRs, whereas square and negative sawtooth waveforms had no effect; this clearly shows a time dependent behaviour which led to the conclusion that EAC only occurs during the rising portion of the load cycle. Further investigation by Scott and co-workers [71] using a BS4340 grade 50D steel in seawater led to the same conclusions. Similar results were also obtained by Atkinson and Lindley [59]. It is

generally accepted that, for systems exhibiting below $K_{ISCC}$ behaviour, those waveforms with significant rise times enhance FCGRs and that growth rates are independent of hold time. FCGRs in systems exhibiting above $K_{ISCC}$ behaviour are expected to be influenced by hold times.

The contribution to crack growth from corrosion fatigue depends upon $\Delta K$ and, since $\Delta K/K_{MAX}$ = 1-R, it is not surprising that many corrosion fatigue data show an R dependence [72]. Generally an increase in the R value results in enhanced FCGRs. This may result from the dependence of 'static' modes of fracture on mean stress [50] or by possible reduction of crack tip shielding effects.

#### 2.2.3.2 Transport of deleterious species

In general the concentrations and diffusion rates of the reactive species in fluids are sufficiently high that supply of the reactant is not the rate limiting step for reactions occurring on free surfaces of metals. However, within a crack, supply of reactant may become rate limiting and the composition of the environment within the crevice will differ from that of the bulk.

In cyclic fatigue, the mass transport of the environment in a crack is dependent on a number of processes which will control transport rates [73], these are namely diffusion, ion migration and advection. Advection results from the cyclic displacement of the crack walls, while diffusion and ion migration are a consequence of electrode reactions on the walls and tip of the crack which, by generating or removing ionic species, create concentration and potential gradients.

Turnbull [74] predicts that, for relatively shallow cracks, the mass transport is dominated by diffusion and that the fluid flow contribution by advection becomes important with increased crack depths. The critical crack depth, $l_{crit}$, at which the rate of mass transport by advection will be equivalent to the rate of transport by diffusion from the bulk solution may be estimated by the equation for a trapezoidal crack [74]:

$$l_{crit} = \frac{(D/\nu)^{1/2}}{1-R^{1/2}}$$

where D = diffusion coefficient
$\nu$ = cyclic frequency
R = load ratio

Taunt and Charnock [75] suggest that for liquids, where the diffusion coefficient is low, advection always dominates, while Wei and co-workers [76] have suggested that for small cracks the rate limiting step for crack growth rate enhancement is the rate

of the reaction between the environment and the freshly produced metal surfaces at the crack tip, whereas in long cracks the rate limiting step is the mass transport of the environment to the crack tip.

The effect of crack depth on the electrochemistry in a corrosion fatigue crack is extremely difficult to determine because of the contribution of fluid flow and crack closure. Gangloff [77] has shown that small (0.1 - 2mm) cracks in a high strength 4130 steel in saltwater grow up to 500 times faster than long cracks (15 - 40mm) at constant $\Delta K$. He suggests that small cracks grow at extremely rapid rates because of enhanced hydrogen production resulting from increased hydrolytic acidification and reduced oxygen inhibition within the occluded cell. The size effect is attributed to crack geometry dependent mass transport.

#### 2.2.3.3 Local crack tip chemistry

It is well known that the solution chemistry and electrode potential within a crack can vary markedly to that of the bulk solution as a result of restricted mass transport. Reaction rates cannot, therefore, be predicted from the bulk chemistry. The restricted geometry of a crack also makes experimental measurement of the local solution and potential difficult, although a number of techniques have been developed by researchers to cope with this.

Brown [78] proposed that the conditions within an occluded corrosion cell were acidic; the acidity caused by the hydrolysis of one or more components of the metal or alloy and maintained by restricted mass transport. After studying the electrochemical conditions at the crack tip of an advancing stress corrosion crack in an AISI 4340 steel, Brown and co-workers [79] showed that the conditions at the crack front favoured hydrogen evolution under conditions of free corrosion, anodic polarisation and cathodic polarisation. This led to the proposition of a mechanism depicting the cracking process of stress corrosion cracking as one of degradation of the metal by hydrogen; a process independent of external potential or pH of the bulk solution.

It has been shown that the potentials in cracks are usually less than the bulk potential and that the potential drop in low alloy and stainless steels is generally $\leq$150 mV SCE under free corrosion potentials in various conducting environments [80]. In a review on the progress of the understanding of the electrochemistry in cracks, Turnbull [80] has concluded that for structural steels and low alloy steels in marine environments the potential drop is small for potentials between -700 mV and -1000 mV SCE but increase significantly outside this range. In view of cathodic protection there is little virtue in depressing the bulk potential below -1000 mV SCE since there is little extra protection gained, hydrogen cracking is more likely and hydrogen bubbles could interfere with transport of current into the crack.

### 2.2.3.5 Crack paths or fracture modes

EAC may often lead to a change in the mode of cracking from the reverse slip mechanism prevalent in inert environments to low energy mechanisms such as intergranular cracking, cleavage, quasi cleavage and enhanced micro void coalescence. A change in the cracking mode is usually accompanied by significant increases in FCGRs.

It has been demonstrated that the presence of segregated impurity elements promotes intergranular decohesion under static loading conditions [81-83]; the intergranular decohesion is considered to be the most common hydrogen induced fracture mode in quenched and tempered steels, and usually occurs along prior austenite grain boundaries. Wei and co-workers [84,85] confirm the tendency for intergranular separation along prior austenite grain boundaries in quenched and tempered steels but suggest that the impurity element segregation is not a necessary precursor to intergranular EAC, although it most certainly assists the process.

Dissolved hydrogen has been found to produce brittle fracture by decohesion of grain boundaries already weakened by impurity segregation and to cause glide plane decohesion in iron and steel, a phenomenon apparently uniquely due to hydrogen [86]. It occurs in the plates or laths of tempered martensite steels. McMahon [86] goes on to say that the most commonly observed hydrogen-induced fracture mode in quenched and tempered steels is intergranular decohesion, usually along prior austenite grain boundaries.

It has been shown [87,88] that carbides can act as a trap for hydrogen in bcc Fe-Cr alloys. Since the great majority of chromium carbides in the thermally treated samples tested lie on the grain boundary, hydrogen trapping by carbides will increase the grain boundary hydrogen concentration.

Thompson and Bernstein [89] have reported that hydrogen induces prior austenite intergranular fracture in tempered martensite steels as a result of sulphur segregation to the prior austenite grain boundaries. They have also shown that there is a tendency for hydrogen induced cleavage in pearlitic structures. After work performed on a 1045 steel in conditions of martensite, pearlite and spheroidised carbides, Thompson and Bernstein [89] conclude that fatigue crack propagation can be assisted by hydrogen without having a major effect on the crack path or mode. Furthermore, they suggest that there may not even be a direct correlation between the severity of the embrittlement and the occurrence of a brittle fracture mode. Where the crack path does change, the contribution to differences in cracking rate arises from differences in the hydrogen trapping strength of the various microstructural features.

Although a complex mixture of fracture modes are possible under conditions of hydrogen evolution at the crack tip, Hinton and Proctor [90] suggest that the intergranular and cleavage modes have the greatest influence on the cracking behaviour.

### 2.2.4 Mechanisms and Models for Environmentally Assisted Cracking

When a cracked metal is placed in an aqueous environment an electrochemical cell will be set up within the crack; the rate of the anodic reaction will be equivalent to the rate of the cathodic reaction. It is therefore reasonable to assume that corrosion fatigue crack growth may occur as a result of either localised anodic dissolution or embrittlement by hydrogen produced by the cathodic reaction.

As a result of investigations into fatigue behaviour of aluminium alloys in aqueous environments, Lin and Starke [91] suggest that there are a number of possible mechanisms for corrosion fatigue;

(a) fracture due to a surface energy reduction at the crack tip associated with the preferential adsorption of environmental species,
(b) fracture associated with dissolution of active slip bands at the crack tip, and
(c) fracture associated with hydrogen embrittlement phenomena.

More generally, two basic mechanisms have gained acceptance. These are namely anodic dissolution at the crack tip, or hydrogen embrittlement of the metal lattice ahead of the propagating crack. What has become clear, however, from recent literature reviews is that hydrogen embrittlement plays a significant role in enhancing FCGRs when the material is subjected to predominantly aqueous environments.

Although the anodic component is essential to the complete electrochemical reaction, many workers believe that anodic dissolution is not responsible for assisting the cracking process. Others believe that the anodic dissolution and hydrogen embrittlement mechanisms are mutually competitive and that, under given conditions, one process may become more dominant than the other [92], while others believe that the sole contributing factor to EAC is in fact anodic dissolution. Hodgkiess [93] suggests that the similar microstructural features associated with crack processes in air and seawater, and the accelerated crack growth under anodic polarisation conditions points to the validity of the anodic dissolution model.

Lynch [94] suggests that in aqueous environments, anodic dissolution could not produce the high crack velocities that are observed since solvated ions would be unable to diffuse away from crack tips sufficiently rapidly to allow for continued reaction. Furthermore, moist air or water vapour environments, where dissolution

cannot occur, often have very similar effects to aqueous environments suggesting that dissolution is not responsible for embrittlement.

In aqueous environments, including moist air, and in hydrogen bearing environments, the mechanism of environment enhancement of rates, particularly in high strength steels, is seen as a result of hydrogen embrittlement [63,95,96]. According to Scott and co-workers [71], the evidence for a hydrogen embrittlement mechanism for corrosion fatigue cracking in medium and high strength structural steels immersed in salt water solutions is now very strong. After parallel fracture mechanics and surface chemistry studies Wei and co-workers [84] concluded that environmentally assisted crack growth is the result of embrittlement by hydrogen, produced by the reaction of the environment with the freshly produced crack surfaces. This was concluded from comparing fracture surface morphologies of a 4340 steel tested in both aqueous and gaseous hydrogen environments; fracture morphology features were common to all fracture surfaces. The result was attributed to the common denominator of the two environments, hydrogen [85,97]. Similarly, Lynch [98] has compared fractures resulting from stress corrosion cracking, hydrogen assisted cracking and adsorption induced liquid-metal embrittlement and has concluded that the apparently common fracture mechanism was due to an adsorption-induced localised slip process. This logic stems from the liquid-metal embrittlement process, in which chemisorption is the only reaction which generally occurs. A fractographic investigation of fracture surfaces after tests conducted on a 12Ni-5Cr-3Mo steel in a 3% solution of sodium chloride showed hydrogen embrittlement features in all specimens tested under either anodic or cathodic potentials [60]. The consistency with pH results, where a pH of 3 was measured at the crack tip for all specimens, led Barsom [60] to conclude that the accelerated fatigue crack propagation observed by this steel in the 3% sodium chloride solution and in distilled water is caused by hydrogen embrittlement. Hinton and Proctor [90] concluded that the faster FCGRs observed for an API X65 pipeline steel in sodium chloride solution at -1.0 V sce, compared to those observed in air, are due to the presence of hydrogen which is cathodically evolved at the crack tip. Results of McIntyre and Priest [99] indicate some strong similarities between stress corrosion cracking in aqueous solutions and crack growth in both hydrogen and hydrogen sulphide gases. These observations suggest that a common embrittling species, namely hydrogen, may be responsible for the cracking observed. Jacko and Duquette [100] suggest that the rate determining process in environmental fatigue of high strength aluminium alloys is the absorption of hydrogen into the plastic zone ahead of the growing crack.

In inert environments, nucleation of dislocations at crack tips is probably difficult relative to general matrix slip and, hence, significant crack growth does not occur until large strains develop ahead of the crack such that extensive egress of dislocations occurs at crack tips [94]. Rice and Thompson [101] note that the

spontaneous dislocation generation at the crack tip enable the crack to propagate in a ductile manner; brittleness is promoted if the dislocation generation at the crack tip becomes restricted. Lynch [94] suggests that so called 'embrittlement' would result simply because chemisorption of deleterious species at the surface reduces the shear strength of interatomic bonds and facilitates the nucleation of dislocations at the crack tip. Any process which facilitated fracture at reduced loads would decrease the extent of associated plasticity.

Beachem [102] advocates the hydrogen reaction at the crack tip for steels in aqueous environments but prefers to refer to the effect as hydrogen assisted cracking as opposed to hydrogen embrittlement. He suggests that hydrogen diffuses into the lattice ahead of the crack tip and assists whatever deformation processes the matrix will allow, the processes themselves depending upon the stress intensity and the concentration of the hydrogen in solution at the crack tip. Beachem's model [102] differs from previous models in that it suggests that hydrogen does not impede the motion of dislocations but allows dislocations to move or multiply at reduced stresses.

McIntyre and Priest [99] suggest that fresh metal surfaces at the crack tip provide active sites for corrosion and hydrolysis with an accompanying decrease in the pH so that water becomes thermodynamically unstable and dissociates according to the following reactions:

$$Fe \rightarrow Fe^{2+} + 2e^{-}$$

$$3Fe^{2+} + 4H_2O \rightarrow Fe_3O_4 + 8H^{+} + 2e^{-}$$

The hydrogen ions thus evolved can either recombine into molecules or be adsorbed at local cathodic areas of the metal surface and diffuse inwards to facilitate crack nucleation and growth. The influence of the environment on the rate of subcritical crack growth may be governed by the rate of supply of the atomic hydrogen to the specific lattice sites where cracking occurs [99].

In a postulated unified mechanism for stress corrosion and corrosion fatigue cracking, Jones [103] suggests that in many metals and alloys, anodic dissolution and corrosion relieves strain hardening at the crack tip surface and reduces the fracture stress, thus facilitating the nucleation of brittle cracks; hydrogen embrittlement is discounted. The model may be summarised as follows (fig. 2.13):

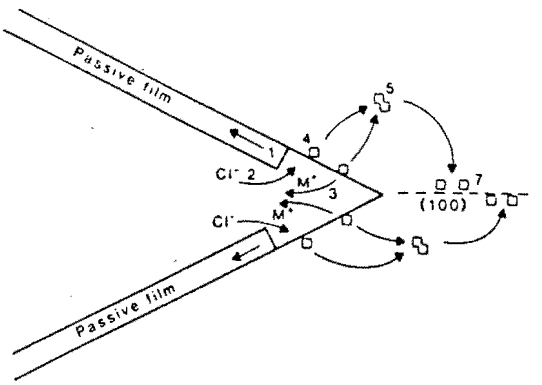


Figure 2.13 Schematic summary of steps in proposed mechanism of stress corrosion and corrosion fatigue cracking (after Jones [103]).

1. **Film rupture**, when mechanical stress is applied to an alloy in the passive state exposed to a corrosive environment.
2. **Retarded repassivation** of rupture sites caused by competitive adsorption of a critical dissolved species for stress corrosion cracking (e.g. chloride ions), or by repeated cyclic loading for corrosion fatigue.
3. **Anodic dissolution** at rupture sites intensified by coupling to large adjoining passive surfaces (galvanic corrosion).
4. **Vacancy formation** at the rupture sites from anodic dissolution.
5. **Divacancy formation** from a supersaturation of surface vacancies followed by migration to critical lattice sites. During corrosion fatigue, divacancies may be formed at internal bulk vacancy sources.
6. **Initiation of surface cracks** by film rupture and slip dissolution on close packed planes with enhanced slip due to dislocation climb induced by reaction with divacancies which have migrated from the surface (omitted from diagram).
7. **Brittle crack propagation** under plane strain conditions by cleavage-like fracture due to the accumulation of divacancies on so called 'prismatic planes'.

A corrosion fatigue model forwarded by Masuda and co-workers [104] analyses results of a number of structural steels tested in 3% sodium chloride aqueous solutions. The model, based on the striation formation mechanism, is proposed as follows (fig 2.14):

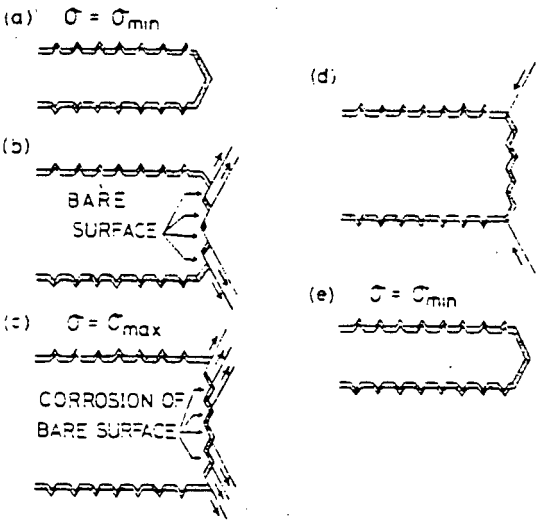


Figure 2.14 Masuda's model of corrosion fatigue crack growth [104].

(a) the crack exhibits a certain crack tip opening displacement at minimum load;
(b) slip occurs with an increase of load and bare surface is produced in succession;
(c) corrosion reaction proceeds on the bare surface;
(d) after the load has reached maximum, reverse slip may occur during unloading on the slip plane where no corrosion has taken place, but not on the corroded plane;
(e) finally, buckling occurs at the crack tip to result in the crack propagation.

Masuda and co-workers [104] suggest too that FCGRs are controlled by three main factors: crack closure, corrosion and reverse slip at the crack tip. They have shown that when crack closure is taken into account, FCGRs are enhanced by a fixed ratio, compared to those in air, according to test frequency. It is noted that this is true only for cracking by the striation mechanism; discrepancies were observed where alternate cracking mechanisms resulted. The main corrosion reaction considered is the adsorption reaction of water molecules:

$$Fe + H_2O = Fe(OH)ads + H^+ + e^-$$

In conclusion, by assuming that the adsorption of the water molecules on the slip plane prevents reverse slip, it is possible to predict the effect of the environment on the FCGRs by calculating the amount of corrosion reaction at the slip plane.

Wei and Landes [105] proposed that the corrosion fatigue propagation rate is equal to the sum of the individual contributions of the environmental rate of attack and the cyclic dependent mechanical fatigue crack propagation rate. Note that this model ignored contributions from environmental cyclic dependent behaviour and did not take into account enhanced rates of subcritical cracking below $K_{ISCC}$.

Austen and Walker [63] proposed a Process Competition Model which assumes that the processes of stress corrosion cracking and corrosion fatigue are mutually competitive, not additive as in the Wei and Landes model. Consequently, the crack will propagate by the fastest available mechanism pertinent to the applied stress intensity.

It has subsequently been recognised [106] that mechanical, or 'pure', fatigue and cyclic dependent corrosion fatigue can proceed by different micromechanisms and that they can occur concurrently or in parallel. The modified Superposition Model can be described by the following equation [106]:

$$(da/dN)_e = (da/dN)_r(1-\phi) + (da/dN)^*_{cf,s}\phi$$

or

$$(da/dN)_e = (da/dN)_r + \{(da/dN)^*_{cf,s} - (da/dN)_r\}\phi$$

where $(da/dN)_e$ is the measured rate of cracking,
$(da/dN)_r$ is the mechanical fatigue rate,
$(da/dN)^*_{cf,s}$ is the 'pure' corrosion fatigue rate, and
$\phi$ is the fractional area of the crack that is undergoing pure corrosion fatigue, with $0 \leq \phi \leq 1$.

In the limit, for a test in an inert environment ($\phi = 0$), the measured rate of cracking is equivalent to the mechanical fatigue rate.

### 2.2.5 Hydrogen Assisted Cracking

There are three main proposals for the mechanism by which hydrogen influences cracking behaviour in metals:

(a) Hydrogen may affect the bonding forces between the metal atoms giving rise to decohesion [107],
(b) Adsorbed hydrogen may lower the surface energy, affecting the Griffith criterion [86,108], and
(c) Hydrogen may induce changes in the dislocation mobility, lower stresses are required to move dislocations [94].

In a keynote paper , McMahon [86] suggests that hydrogen reduces the cohesive energy of the crystal lattice in iron and steel by reducing the work to fracture; this is further reduced by segregation of impurities. This is confirmed by Oriani [107] who suggests that hydrogen reduces the ductility of low strength steels and increases the

cracking of high strength steels by reducing the cohesive strength of atom-atom bonds. Atomically, it is suggested that the 1s electron of hydrogen is delocalised in the valence band of iron which results in an increase in the average local ion-core separation to maintain a constant volume per valence electron. The observed lattice dilation due to hydrogen confirms the suggestion. The overall effect would be to reduce the bonding effect due to the formation of the d-orbital and valence orbital [86].

It is presently believed that molecular hydrogen is produced from the reaction between iron and water where it is dissociated by chemisorption onto the iron allowing liberated atomic hydrogen to diffuse internally thus embrittling the material. The atomic hydrogen can diffuse rapidly through the metal lattice because of its small size where it accumulates at "hydrogen traps" such as grain boundaries, inclusions, voids, dislocation arrays and solute atoms. It has also been shown that the rate of hydrogen transport in association with dislocation motion can be several orders of magnitude greater than that associated with lattice diffusion [109]. This becomes extremely important when considering the reactions taking place at the crack tip, a region of localised plasticity. Much of the literature on transport of hydrogen by dislocations has been reviewed by Hirth [110] and the effect of enhanced diffusion is well established.

It is generally accepted that hydrogen assisted cracking results from hydrogen transported to susceptible sites but it is becoming increasingly evident that a single mechanism does not exist, and that failure can occur by different mechanisms that are dependent on composition, microstructure, density and type of trap sites, and test conditions [111]. Thompson [111] suggests that although hydrogen may induce a more brittle mode of fracture than the usual mode, it does not induce a 'characteristic' mode.

The hydrogen embrittlement process depends on a number of important factors:-

(a) Original location and form of hydrogen (eg. gas or water).
(b) Transport processes.
(c) Reaction between the gas or water and the metal surface.
(d) Transport of the deleterious hydrogen into the material bulk.
(e) Stress levels at the crack tip
(f) Interaction between the hydrogen and metal in the embrittlement zone.

A schematic representation of the possible paths involved in an embrittlement process is presented in fig. 2.15.

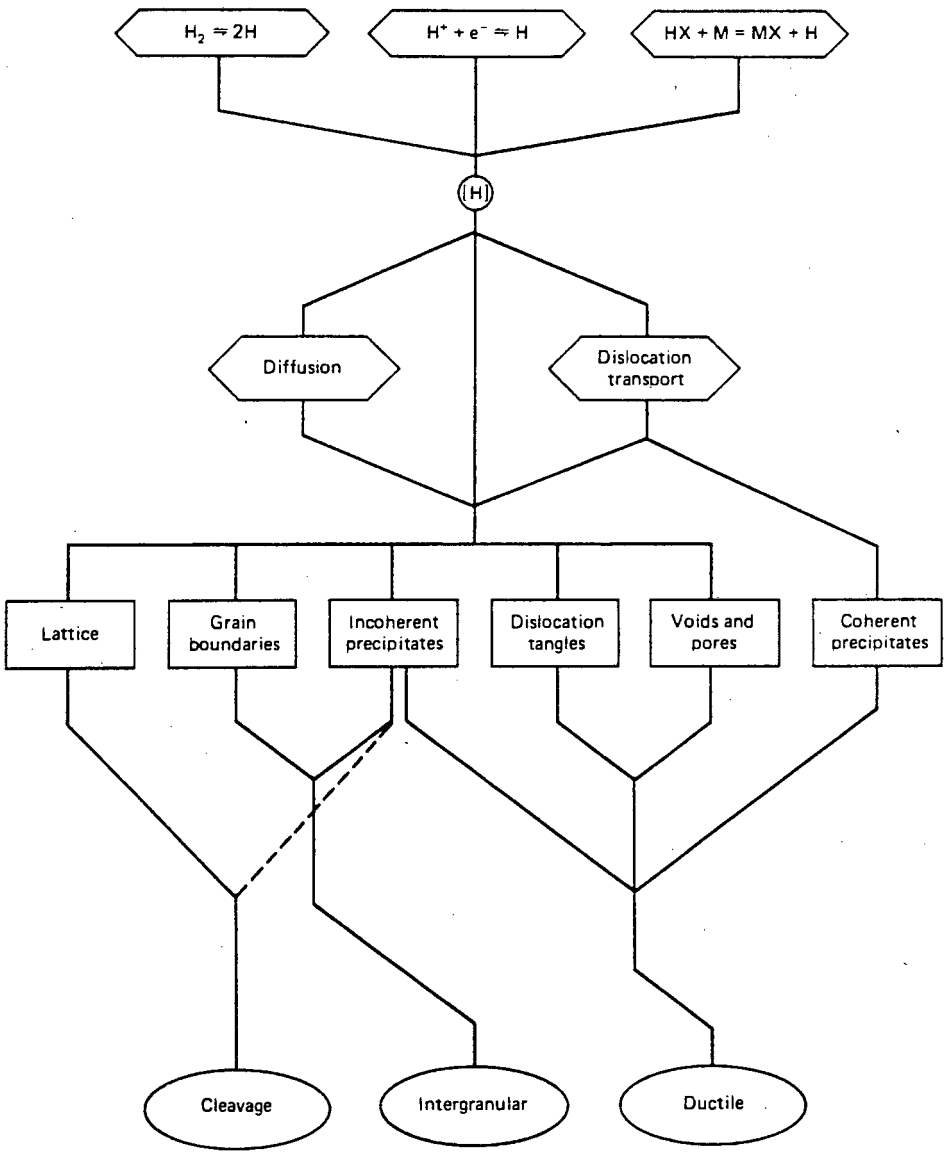


Figure 2.15 Flow diagram depicting hydrogen sources, transport paths, destinations, and induced fracture micromechanisms (after Thompson et al [112]).

It is well known that the susceptibility of steels to hydrogen embrittlement is generally enhanced as their strength increases; it is generally accepted that martensitic microstructures are embrittled by hydrogen and that their susceptibility increases with increased carbon content and hardness [113].

It is important to recognise that the fracture mode in the presence of hydrogen often depends on the level of stress intensity, because as stress intensity decreases, the

associated local plasticity at the crack tip is decreased and only less plastic fracture modes are possible [102].

In a review on the experimental manifestations of hydrogen embrittlement, Thompson and Bernstein [89] highlight a number of major points:
1. Well-defined sharp intergranular and transgranular cracks can be induced by hydrogen, even in materials of very high intrinsic ductility.
2. For transgranular cracks in ferrous materials, produced at room temperature, the crack plane can be an operative slip plane in ductile materials, and an operative cleavage plane in more brittle iron alloys.
3. The partitioning of solutes such as carbon determine whether cracking will be intergranular or transgranular in nature.
4. In multi-phase iron alloys, the presence of traps control the type and extent of hydrogen-induced damage. Traps can either promote or reduce hydrogen effects.
5. Alloys which in air fail by dimpled rupture can be severely embrittled by hydrogen, either with or without a fracture mode change.
6. The failure of hydrogen embrittled materials often occurs along crack paths sensitized by thermal treatment; such paths are followed by other embrittling phenomena.
7. The presence of an aqueous solution can promote cracking, while dimpled rupture would occur if dissolved hydrogen or an external gas environment was the embrittling agent. In both cases, however, a loss in toughness occurs.

In high strength steels which are prone to hydrogen embrittlement, cathodic polarisation may be of little benefit in reducing corrosion FCGRs and overprotection may in fact be detrimental [80] as mentioned in section 2.2.3.3. This has been observed even for an API X65, low strength pipeline steel which is not usually regarded as being susceptible to hydrogen embrittlement [114].

Many papers in past years [115] have strongly advocated that the presence of deformation induced martensite greatly increases the susceptibility of austenitic stainless steels to hydrogen cracking. Andriamiharisoa and co-workers [116] suggest that hydrogen introduced via the environment (e.g. hydrolysis of water) only enhances FCGRs of those stainless steels (e.g. 304L) that undergo an austenite to martensite transformation. They have also shown hydrogen impedes the austenite to $\alpha'$-martensite by promoting $\epsilon$-martensite formation.

# CHAPTER 3

# MATERIALS AND EXPERIMENTAL METHODS

## 3.1 MATERIALS

### 3.1.1 Specifications

The alloys investigated include a mild steel reference, a proprietary stainless steel, AISI 431, a relatively new corrosion resistant steel, 3CR12, and two development alloys, Alloy 825 and 1210. The chemical analyses of the five steels are as shown in Table 1.

TABLE 1. Compositions of the five steels used in this investigation, in weight percent.

| | C | S | P | Mn | Si | Cu | Co | Ti | Mo | Cr | Ni | N |
|---|---|---|---|---|---|---|---|---|---|---|---|---|
| MILD STEEL 070M20 | 0.143 | 0.020 | 0.024 | 0.86 | 0.21 | 0.07 | 0.005 | NIL | NIL | 0.06 | 0.05 | 0.0055 |
| 3CR12 | 0.028 | 0.004 | 0.021 | 1.22 | 0.28 | 0.09 | 0.011 | 0.54 | 0.01 | 11.33 | 0.64 | 0.0130 |
| AISI 431 | 0.147 | 0.012 | 0.021 | 0.42 | 0.27 | 0.21 | 0.061 | NIL | 0.06 | 16.11 | 1.89 | 0.0231 |
| ALLOY 825 | 0.262 | 0.005 | 0.011 | 0.34 | 0.18 | 0.07 | 0.018 | NIL | NIL | 8.73 | 3.34 | 0.0274 |
| 1210 | 0.046 | 0.007 | 0.016 | 10.02 | 0.46 | 0.01 | 0.003 | NIL | NIL | 11.85 | 0.08 | 0.1786 |

### 3.1.2 Thermal Treatments

The mild steel, 3CR12 and 1210 were all tested in an 'as received' condition. Bright mild steel was received from stock in plate form, 25 mm thick. The mechanical behaviour suggests that the plate has been cold worked to some degree, but the microstructure shows no evidence of this. The 3CR12 was received as commercial plate, 30 mm thick, which is supplied in a hot rolled and annealed condition. This

treatment is performed at a temperature not exceeding 750°C. A 26 mm thick plate of 1210 was received from a commercial melt and was expected to have undergone some cold working; the extent of working was not documented. The electropolished samples of 1210 show evidence of transformed martensite, confirming that the material has undergone some cold working treatment. The Alloy 825 was received in 28 mm thick plate form and finished specimens underwent the following thermal treatment:

1. preheat at 775°C for 45 minutes,
2. soak at 1100°C for 45 minutes,
3. oil quench,
4. temper at 200°C for 2 hours.

The proprietary AISI 431, cut from a large billet, was given a specific thermal treatment to obtain the properties required for particular applications, and is as follows:

1. preheat at 540°C for 30 minutes,
2. soak at 775°C for 30 minutes,
3. soak at 1040°C for 30 minutes,
4. marquench to 175°C and hold for 12.5 minutes,
5. air quench,
6. hot alkaline wash,
7. sub-zero treatment, -75°C for 30 minutes,
8. double temper at 200°C, 2 hours per temper,
9. passivate.

Note that the treatment durations are expressed for the actual specimen geometries reported in section 3.2.2.

### 3.1.3 Microstructures

Samples from each material were cut and prepared for a microstructural investigation in which they were polished to a 0.25 micron finish before an etching or electropolishing treatment. The respective microstructures of the materials are illustrated in figs 3.1 to 3.5. The specific etchants or electropolishing solutions used are reported in the respective figure captions along with approximate grain sizes. The reported grain sizes are the average grain sizes estimated using the ring analysis method and, where applicable, refers to prior austenite grain boundaries.

The mild steel consists of a fine grain structure of ferrite grains and pearlite colonies with a normalised appearance. 3CR12 shows a fine grain structure consisting predominantly of ferrite with regions of low carbon lath martensite; titanium

carbonitride inclusions are also evident. AISI 431 exhibits a lath martensite structure with a large incidence of retained δ-ferrite. Alloy 825 shows a large grain, lath martensite structure and is expected to contain approximately 5% retained austenite situated at the lath boundaries. The electropolished sample of 1210 reveals the metastable austenite structure of this alloy with regions of transformed martensite. Note that preparation by pure mechanical polishing revealed a microstructure comprising almost entirely of transformed martensite.

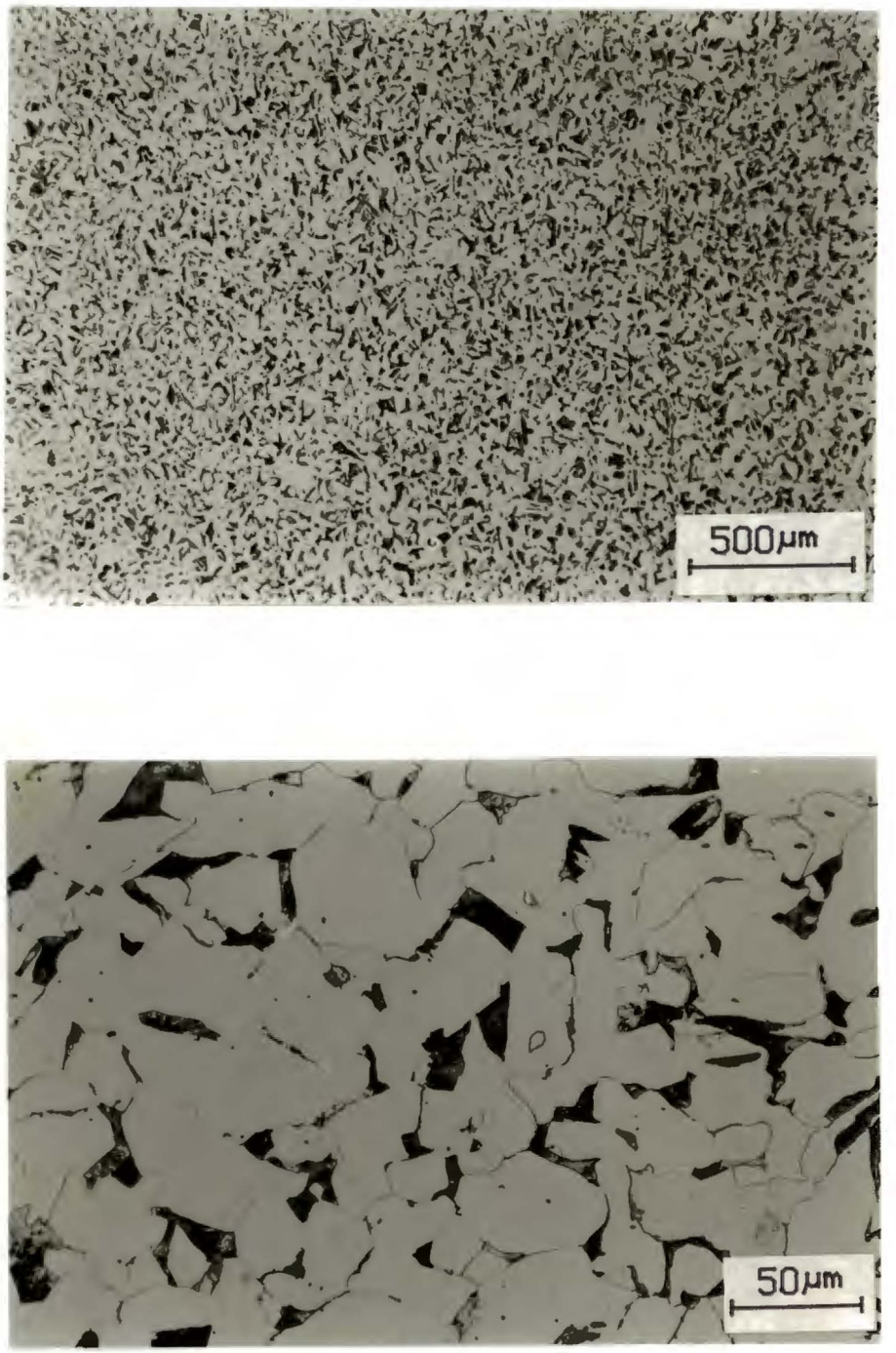


Figure 3.1 Optical micrographs of the cold rolled mild steel, showing ferrite grains and pearlite colonies, etched in a 2.5% Nital solution. The steel has an approximate grain size of 21 μm.

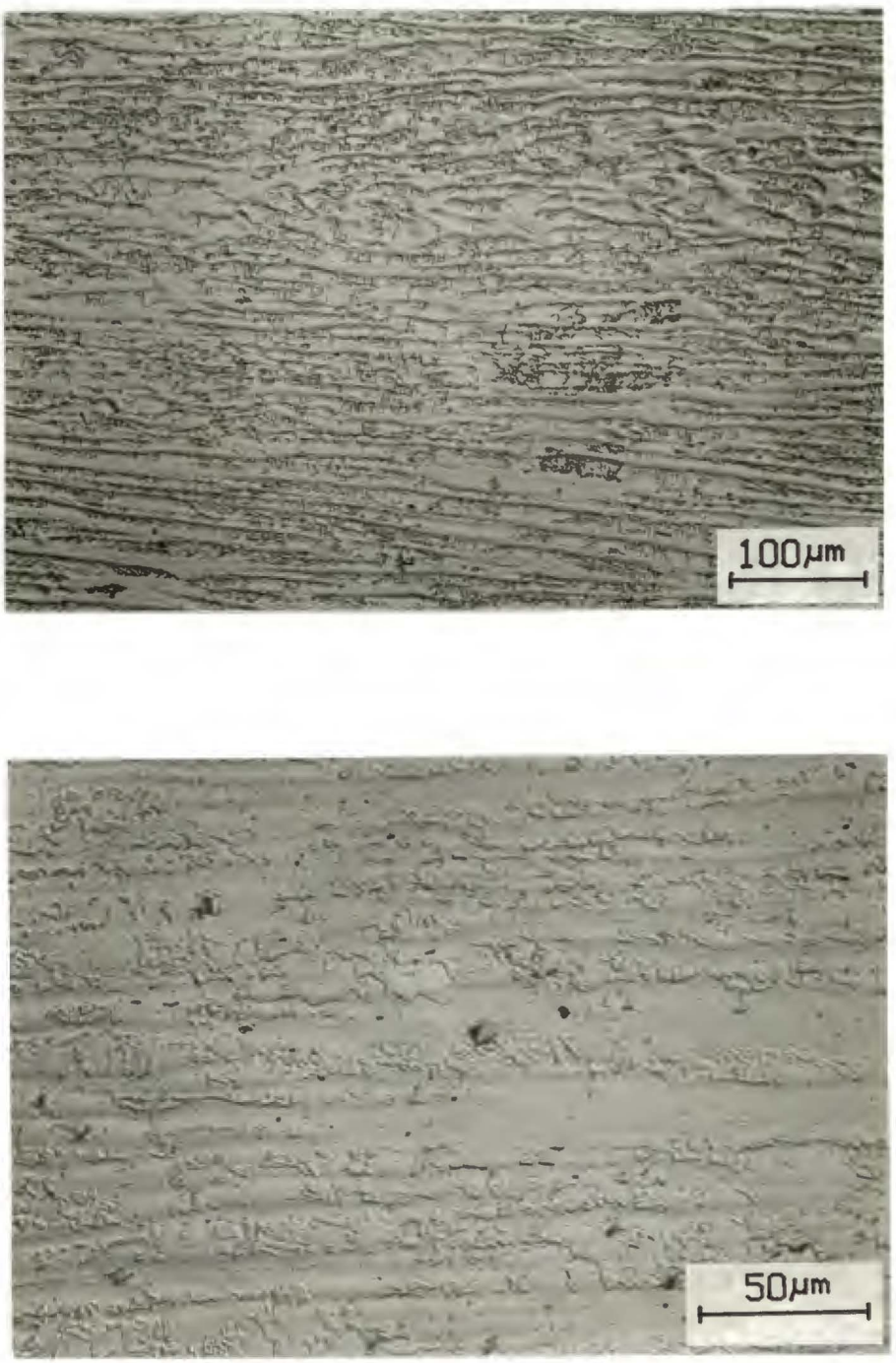


Figure 3.2 Optical micrographs of 3CR12, showing the dual phase ferrite/low carbon lath martensite structure, etched in a solution consisting of 20 ml conc. HCl, 100 ml water, 2g ammonium biflouride and 1g potassium metabisulphite. Approximate grain size is 25 μm.

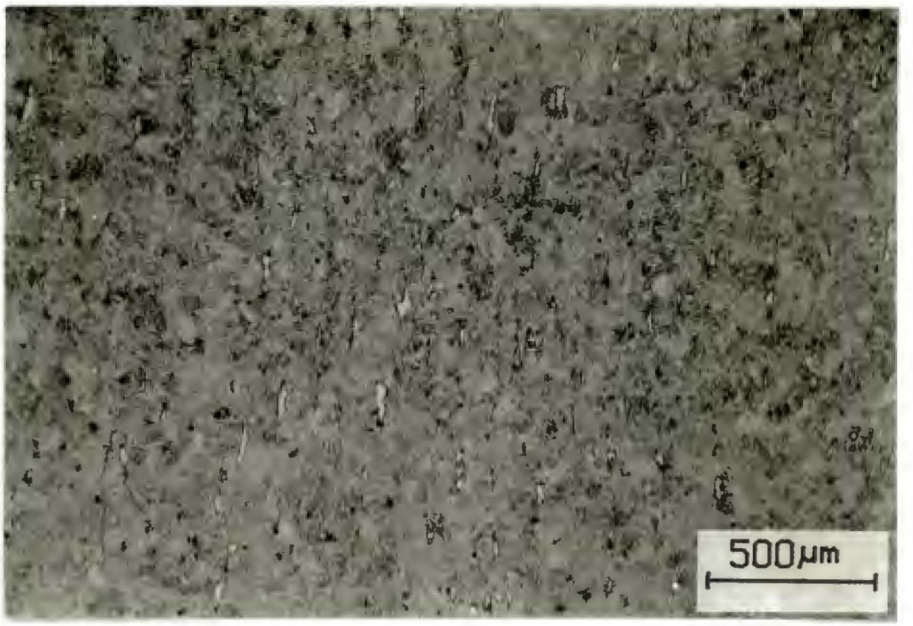


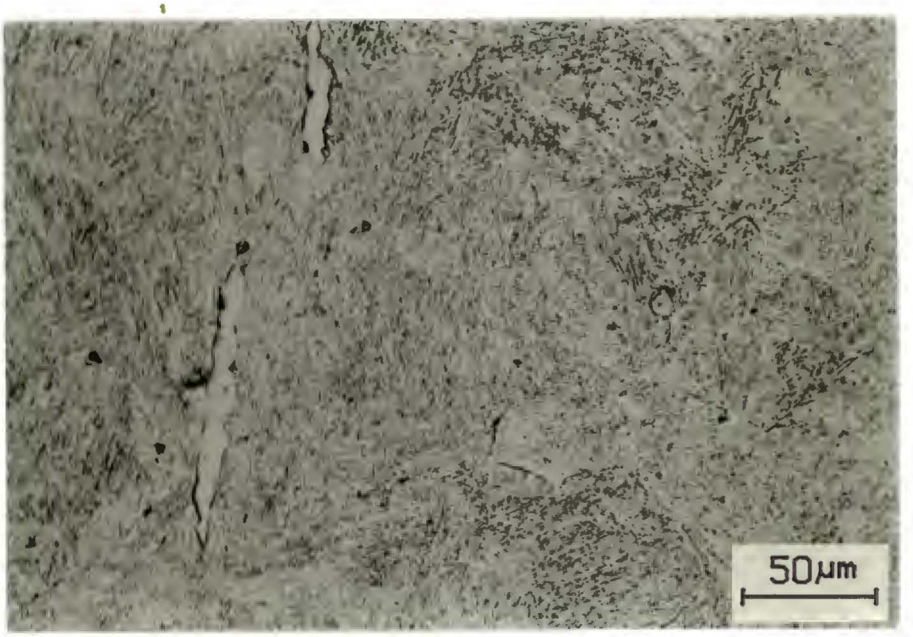


Figure 3.3 Optical micrographs of the martensitic structure of AISI 431, showing regions of retained $\delta$-ferrite. Etched in a solution consisting of 10ml nitric acid, 20ml hydrochloric acid, and 30ml distilled water. Approximate grain size is 50 $\mu$m.

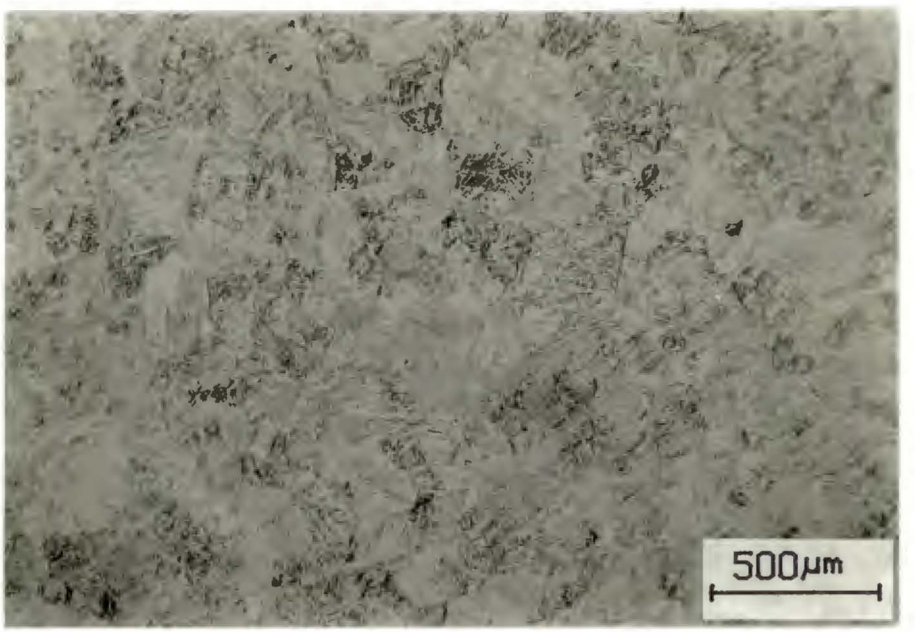


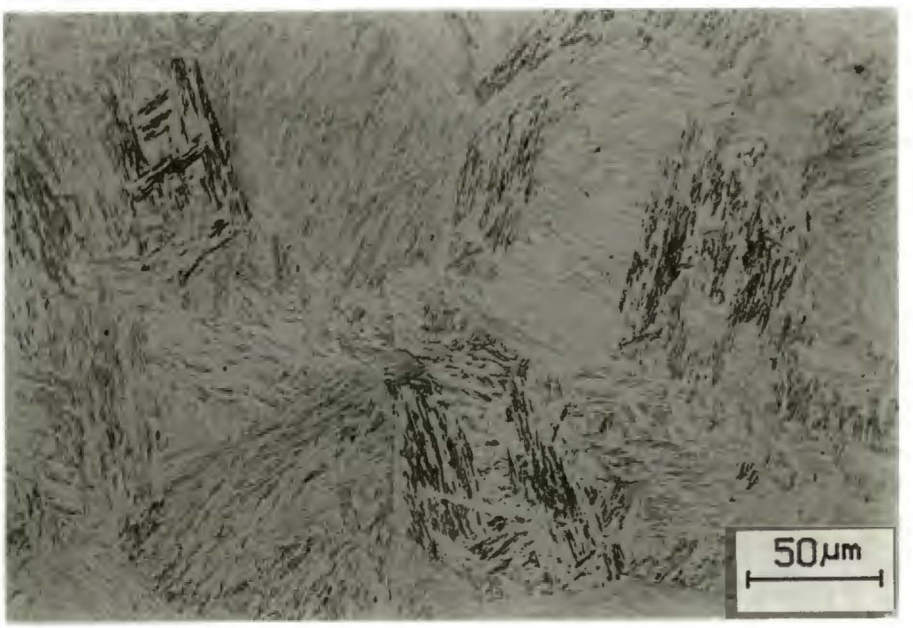


Figure 3.4 Optical micrographs showing the martensitic structure of Alloy 825. Etched in Vilella's reagent, comprising 1g picric acid and 5 ml concentrated hydrochloric acid in 100 ml methanol. Approximate grain size is 80 μm.

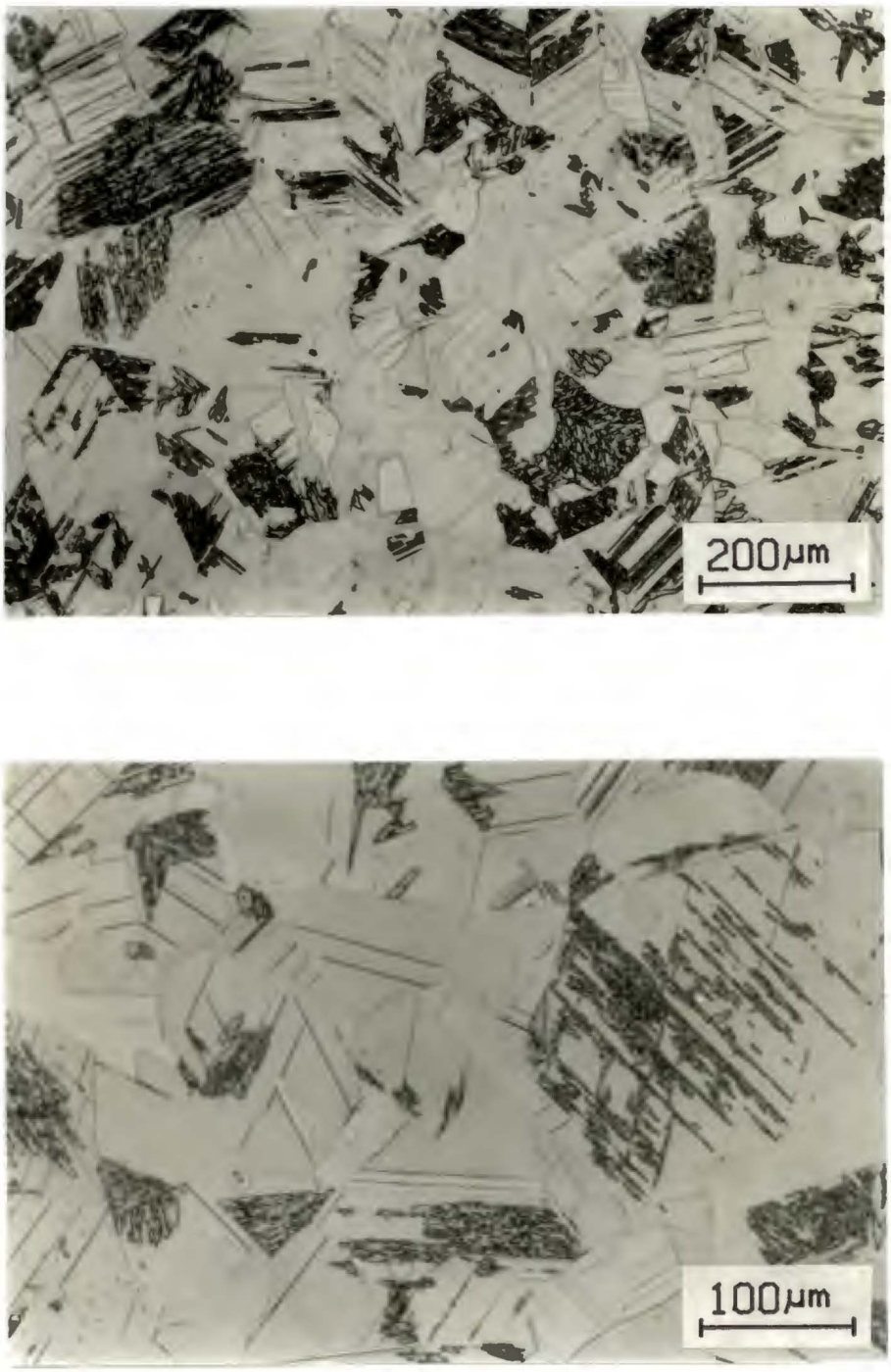


Figure 3.5 Optical micrographs showing the metastable austenite and transformed martensite structure of the cold worked 1210 electropolished and etched in a solution comprising of 60 ml lactic acid, 20 ml phosphoric acid, 30 ml sodium acetate, 15 ml hydrochloric acid and 20 ml sulphuric acid. Approximate grain size is 90 μm.

### 3.1.4 Mechanical Properties

Typical tensile curves of engineering stress vs. engineering strain for the five materials used in this investigation are illustrated and compared in fig. 3.6. The mechanical properties derived from tensile, hardness and Charpy V notch tests are listed in Table 2.

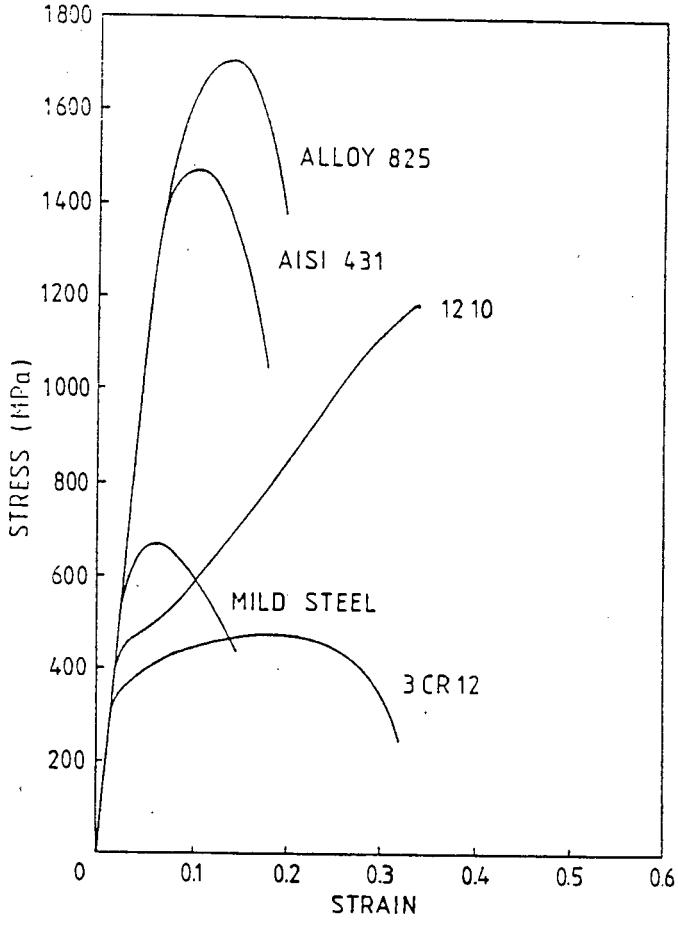


Figure 3.6 Typical stress strain behaviour of the steels.

The relatively low elongation shown by the mild steel can be attributed to the extent of cold working of the material in the as received condition. The fine dual-phase microstructure of 3CR12 consisting of ferrite grains and regions of low carbon lath martensite confer good ductility and toughness on this material. The medium carbon martensite of AISI 431 and the relatively high carbon martensite of Alloy 825 result in characteristic high strength, low elongation properties. The presence of a stable retained austenite at the martensite lath boundaries in Alloy 825 (which has not been confirmed in this study) is expected to confer a measure of toughness to this high strength alloy. The 1210 exhibits extreme work hardening behaviour

through the transformation of metastable austenite to nitrogen-strengthened martensite during deformation, and displays good mechanical properties. A detailed study on the structure and properties of 1210 has been reported in references 14-16.

Table 2 Mechanical properties of the steels used in the investigation.

| | Hardness $VHN_{30}$ | 0.2% Proof Stress MPa | UTS MPa | %E (25mm Gauge Length) | CVN J |
|---|---|---|---|---|---|
| BSS 070M20 | 190 | 529 | 653 | 12 | 21 |
| 3CR12 | 167 | 340 | 459 | 34 | 80 |
| AISI 431 | 449 | 1200 | 1480 | 13 | 6 |
| Alloy 825 | 540 | 1200 | 1710 | 14 | 63 |
| 1210 | 309 | 411 | 1231 | 30 | 110 |

## 3.2 EXPERIMENTAL APPARATUS AND PROCEDURES

### 3.2.1 Equipment

FCGR tests were carried out in accordance with ASTM standard E647-78T [117] using a servo-hydraulic universal testing machine under load control. The servo-hydraulic testing machine and the ancillary equipment used is shown in fig. 3.7.

Crack lengths were monitored via a strain gauge on the back face of the specimen in conjunction with a Hewlett Packard 3497A Data Aquisition/Control Unit that was fitted with a strain gauge card configured so as to complete a 1/4 bridge arrangement. Similarly a temperature compensating gauge attached to an independent sample of the same material was accessed through the data aquisition unit and strain gauge card. Details on the back face strain technique are given in section 3.2.3.1. The data aquisition unit was controlled with an HP 85 microcomputer, using software specifically developed for this programme (detailed in section 3.2.3.3). The use of the data aquisition unit in conjunction with the strain gauges removes the requirement for balancing the bridge, compensates for non-linearities in output and handles switching and data storage in multichannel applications. Thus measurement accuracy is increased and the handling of large quantities of data from a number of channels is facilitated.

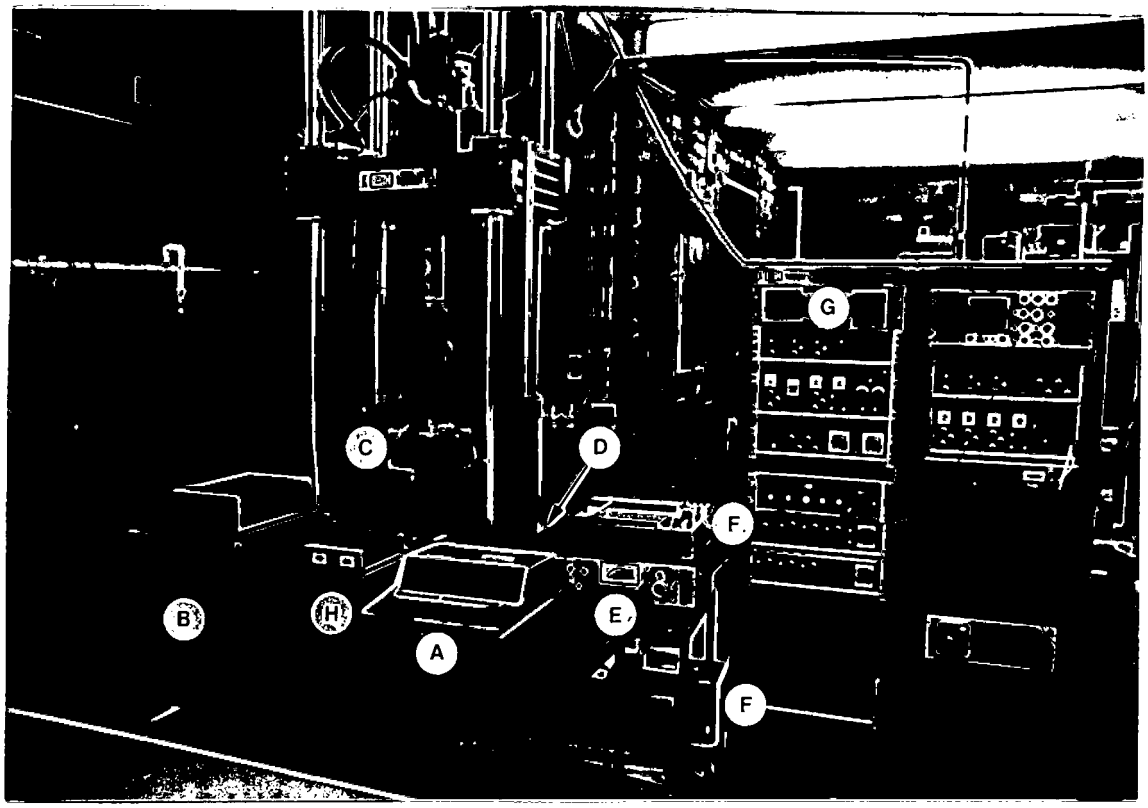


Figure 3.7 The ESH servo-hydraulic universal testing machine and ancillary equipment; A - microcomputer; B - data aquisition/control unit; C - corrosion cell; D - reservoir and thermoregulator (hidden from view); E - potentiostat; F - recorders; G - UTM control panel; H - strain gauge voltage supply.

The aqueous environment was contained around the specimen in a transparent polymethyl methacrylate (PMMA) cell that was continuously replenished from a thermally regulated reservoir.

A Wenking LT-78 potentiostat was used to either monitor the free corrosion potential and the current density of the material/environment reaction, or to impose a cathodic potential on the specimen. Counter electrodes were provided by rods of inert graphite; potential and current densities were measured against a Saturated Calomel Electrode (sce) standard. Note that further reference to potentials will not be accompanied by the letters sce since this was the only reference electrode used. A close-up of the environmental chamber is shown in figure 3.8.

For all FCGR tests in air, the strain gauge was protected against atmospheric humidity using a commercial gauge coating. The strain gauges on specimens intended for environmental testing were protected with the same commercial coating followed by several layers of wax. This treatment ensured trouble-free submersion in an aqueous environment for up to 150 hours (longest test duration).

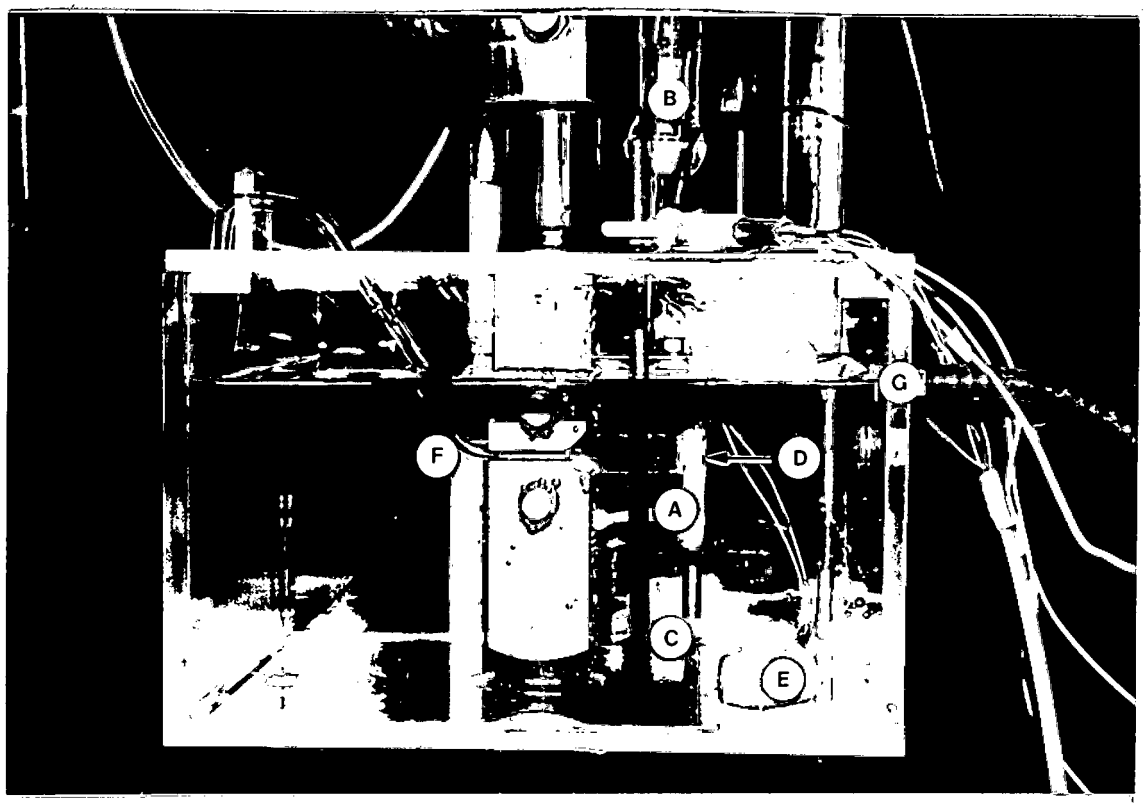


Figure 3.8 Details of the corrosion cell; A - coated specimen; B - reference electrode; C - counter electrodes; D - protected strain gauge; E - temperature compensator; F - water inlet; G - water outlet.

### 3.2.2 Procedure

Experiments utilised 25 mm thick compact tension specimens with the notch perpendicular to the rolling direction (longitudinal-transverse orientation). Specimens were machined with a chevron notch and, prior to precracking, a sharp groove was made with a thin fretting saw (0.2 mm) or by spark erosion (0.35 mm) to ensure an even crack initiation. The dimensions of the specimens are as shown in fig. 3.9.

All tests were conducted using tension-tension, sinusoidal cyclic loading with a load ratio, $R = 0.1$ and a load range, $\Delta P = 14.4$ kN. Prior to testing, a fatigue crack was initiated and the specimen was precracked in accordance with the ASTM standards, at a load range necessary to arrive at a specified $\Delta K$ after propagating the crack for a minimum of 2 mm.

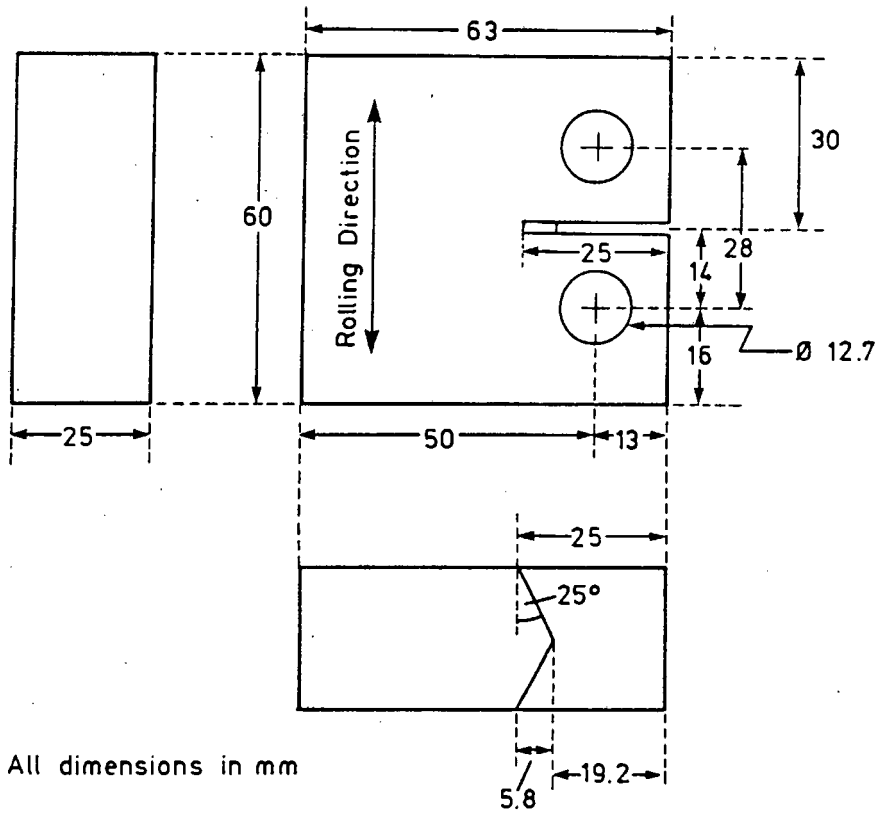


Figure 3.9 A schematic of the compact tension specimen geometry and dimensions.

Tests performed in air were carried out at a frequency of 3 Hz and all tests in aqueous environments were conducted at 1 Hz. The choice of 1 Hz for the environmental testing was made for a number of reasons : i) 1 Hz is used extensively by other researchers, ii) it is a frequency at which test durations will not be excessively long, but will still guarantee a significant environmental effect on the measured FCGRs, and iii) the effect of frequency on FCGRs has been shown to reach a maximum between 1 and 0.1 Hz [58]. The choice of 3 Hz for the tests in air was influenced by the limitations of the data aquisition system, and is discussed in more detail in section 3.2.3.2.

The environmentally-assisted FCGR testing was undertaken in three different aqueous solutions: distilled water, water containing 500 ppm chloride (so called 500 Cl on the legends of the FCGR curves), and water containing 1000 ppm chloride (1000 Cl). Tests in these environments were performed at the free corrosion potential and, for each material, further tests were conducted at a potential of -1200 mV in the 1000 ppm chloride solution (indicated as -1200 mV in the legends of the of the FCGR curves). All chloride containing solutions were made up using analytical reagent grade sodium chloride salt in distilled water.

Specimens intended for the environmental tests were coated with a lacquer, leaving a 1cm wide strip of exposed metal on each side of the specimen, along the expected crack path. The purpose of the coating was to limit the corrosion activity to these exposed regions and the crack itself.

During testing the crack length and the time were monitored continuously and measurements were collected approximately every 0.25 mm of crack growth. At the conclusion of each test the specimen was fractured to facilitate both the measurement of crack curvature and a study of the fracture surfaces. The accuracy of crack length measurement was limited by the 0.1mm resolution of the vernier mounted on an optical microscope.

A detailed examination of the fracture surfaces was made using a Cambridge S200 scanning electron microscope (SEM) once the fracture surfaces had been cleaned.

### 3.2.3 Data Aquisition

This section describes the methodology behind the automated collection of data during the FCGR tests and the work done in evaluating proposed techniques and procedures.

A reliable automated method of data aquisition was sought for two reasons : i) test durations at a frequency of 1 Hz may exceed several days, and ii) optical methods of measuring crack length may result in numerous interruptions of the fatigue loading which may in turn lead to transient effects on the FCGRs. This was highlighted at the start of the investigation, where a replication technique was used to monitor the crack length. Other optical methods, such as the travelling microscope method, were not suited to this study where the solution often became discoloured as a result of the corrosion activity.

Crack lengths have been successfully monitored by other workers using a number of alternative techniques, such as potential drop, specimen compliance, and back face strain (BFS). In this investigation, potential drop was not considered due to equipment unavailability, but both the compliance and BFS techniques were evaluated. The BFS technique proved to be the most reliable and the most suitable method, and the work of evaluating this technique is discussed in the following subsection.

### 3.2.3.1 Back Face Strain

Crack lengths were monitored using the Back Face Strain (BFS) technique [118,119] in which the uncracked ligament of the compact tension specimen is regarded as a beam in bending. Richards and Deans [118,119] have shown that the compressive stresses set up in the back face of the specimen increase linearly with crack length for constant stress intensity conditions, and increase exponentially with crack length for constant load conditions, although some deviation is expected to occur for crack length to width ratios, $a/W > 0.6$. The normalised strain, $A^*$, as a function of $a/W$ is given by the equation :

$$A^*(a/W) = \frac{(BFS)B.W.E}{P} \quad \text{.....(1)}$$

where P is the load, B is the specimen thickness, W is the specimen width and E is the Young's modulus of the material.

A number of preliminary fatigue tests were performed using mild steel specimens to test the validity of the BFS method as applied to the equipment and procedures adopted for this investigation. This involved interrupting the fatigue test periodically to enable optical measurement of the crack length and to record the corresponding peak strain at the back face of the specimen. During these interruptions, the strain as a function of load was plotted for loads from 0 to 16 kN and the linearity of the strain gauges was confirmed. The results are illustrated in fig. 3.10.

For all crack lengths, a , the strain varies linearly with load. It is clear, however, that the mild steel specimen displays some residual plastic behaviour at zero loads for $a/W > 0.36$. This behaviour becomes quite significant at $a/W > 0.6$, as predicted by Richards and Deans [118,119]. The initial crack length/peak strain readings were used to construct a plot showing the exponential relationship of the normalised strain as a function of a/W. This was compared to the normalised data published by Richards and Deans [119] and is presented in fig. 3.11. A listing of the normalised strain data from reference 119 is given in Table 3.

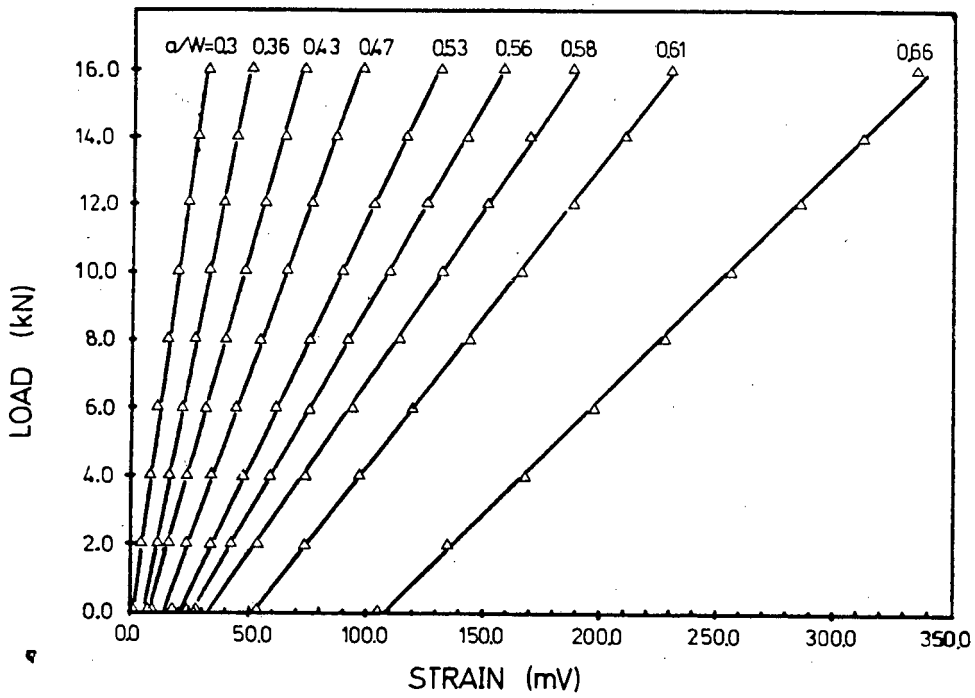


Figure 3.10 Graph illustrating the linear variation of strain with load and the changing compliance of the specimen with a change in crack length.

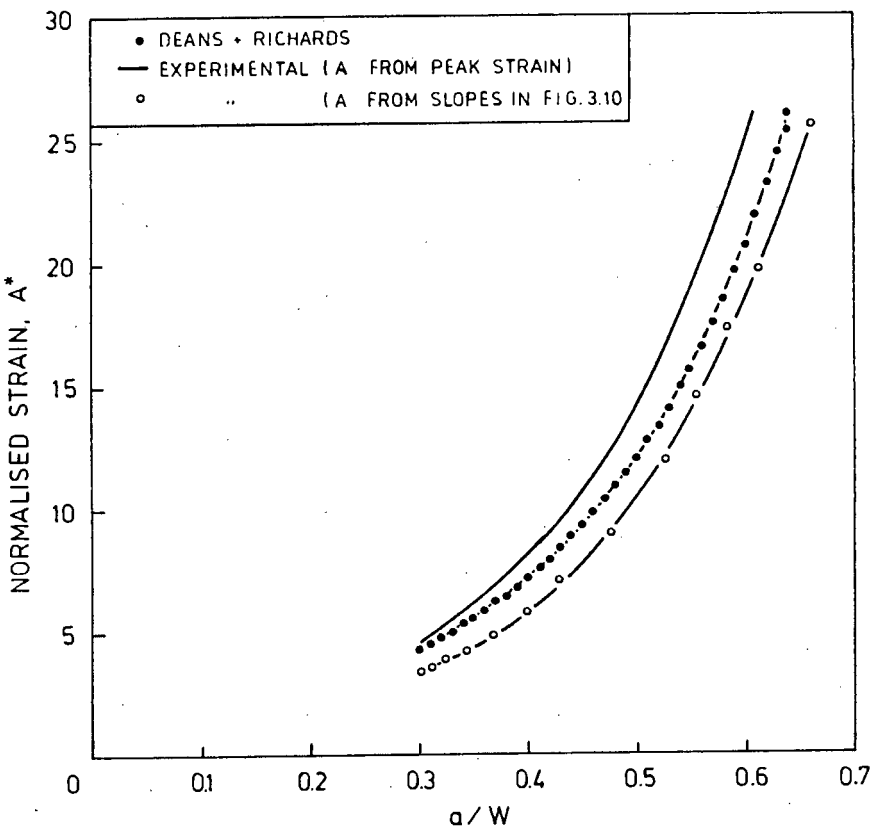


Figure 3.11 Normalised strain as a function of a/W comparing data from table 3 with experimental data obtained from; (i) the peak strain values, and (ii) the slopes of the lines in figure 3.10.

TABLE 3 Variation in compressive BFS with a/W in CT specimens normalised for specimen dimensions, B, W and Young's Modulus, E (after Richards and Deans [119]).

| a/W | $A^* = \frac{(BFS).BWE}{P}$ | a/W | $A^* = \frac{(BFS).BWE}{P}$ |
|---|---|---|---|
| 0.30 | 4.26 | 0.50 | 12.0 |
| 0.31 | 4.49 | 0.51 | 12.7 |
| 0.32 | 4.74 | 0.52 | 13.3 |
| 0.33 | 5.00 | 0.53 | 14.0 |
| 0.34 | 5.28 | 0.54 | 14.8 |
| 0.35 | 5.56 | 0.55 | 15.6 |
| 0.36 | 5.84 | 0.56 | 16.5 |
| 0.37 | 6.15 | 0.57 | 17.5 |
| 0.38 | 6.45 | 0.58 | 18.4 |
| 0.39 | 6.81 | 0.59 | 19.5 |
| 0.40 | 7.17 | 0.60 | 20.6 |
| 0.41 | 7.55 | 0.61 | 21.8 |
| 0.42 | 7.96 | 0.62 | 23.1 |
| 0.43 | 8.39 | 0.63 | 24.4 |
| 0.44 | 8.85 | 0.64 | 26.0 |
| 0.45 | 9.31 | | |
| 0.46 | 9.79 | | |
| 0.47 | 10.3 | | |
| 0.48 | 10.9 | | |
| 0.49 | 11.4 | | |

Initially, the experimental relationship compares well with that from the literature , but deviates at higher values of a/W. The peak strain readings were expected to give errors at higher a/W ratios due to the increased residual strains experienced. To reduce this error, the slopes of the strain/load lines of fig. 3.10 were used in the calculation of the normalised strain, $A^*$. When plotted against a/W and compared to the data from Table 3, a relatively constant displacement is observed (fig. 3.11). These results were preferable, since a constant error can be more readily corrected.

A decision was taken then, to utilise the generalised Richards and Deans relationship (equation 1) and the exponential fit of the data of Table 3:

$$A^* = 0.884e^{5.239a/W} \quad \text{.....(2)}$$

The error between the optical and calculated crack lengths could be recorded at the beginning and the end of a test, crack curvature taken into account, and the calculated crack lengths adjusted accordingly.

On introducing a new method of recording the strain (see section 3.2.3.2) which involved the estimation of the maximum and minimum strains, a further trial was conducted, this time using AISI 431 in the as received condition. When compared to the Richards and Deans relationship, a similar trend to that exhibited by mild steel was observed (fig. 3.12).

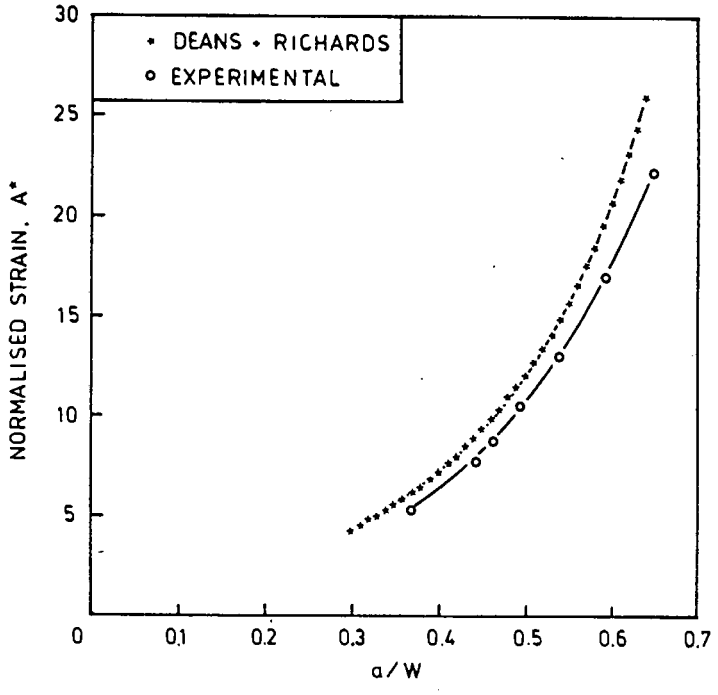


Figure 3.12 Normalised strain as a function of a/W comparing the standardised data of table 3 to the experimental data obtained from estimates of the minimum and maximum strains recorded in a load cycle.

To test the consistency of over or under-estimation of the crack length by the strain gauge method, a plot was made, comparing the calculated crack length to the corrected optical crack length (optical crack length plus curvature correction). The results are illustrated in fig. 3.13.

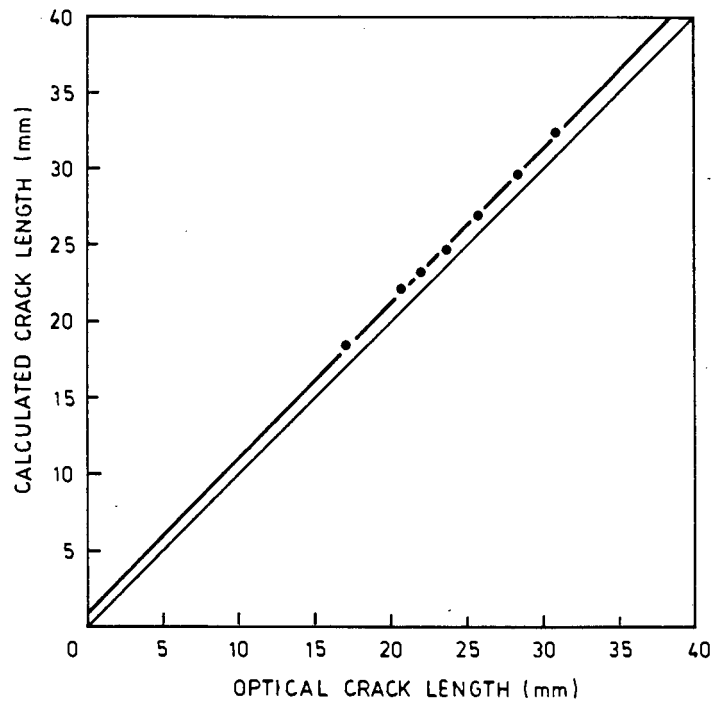


Figure 3.13 Graph showing the relationship between the calculated crack length and the corrected optical crack length for the test conducted on AISI 431. The uninterrupted line represents a 1:1 relationship.

A least squares fit on the data resulted in a slope of 1.002 and a correlation coefficient of 0.999 proving that the error was indeed consistent and, as a result, confidence in this method was gained.

In summary, although the BFS technique is not considered to be the most reliable method of monitoring crack lengths, it is a relatively inexpensive and simple method and proved to give adequate results. Sufficient confidence was gained in this method to continue its use.

### 3.2.3.2 Frequency vs. Data Aquisition Buffer

The data aquisition unit is capable of recording a buffer of 60 readings in approximately 3 seconds. A sinusoidal trace of the cyclic strain was to be constructed from a buffer of 60 strain values and was to supply estimates of the maximum and minimum strains for the final calculation of the crack length. The effect of cyclic frequency on the resultant trace was investigated and the results are illustrated in fig. 3.14.

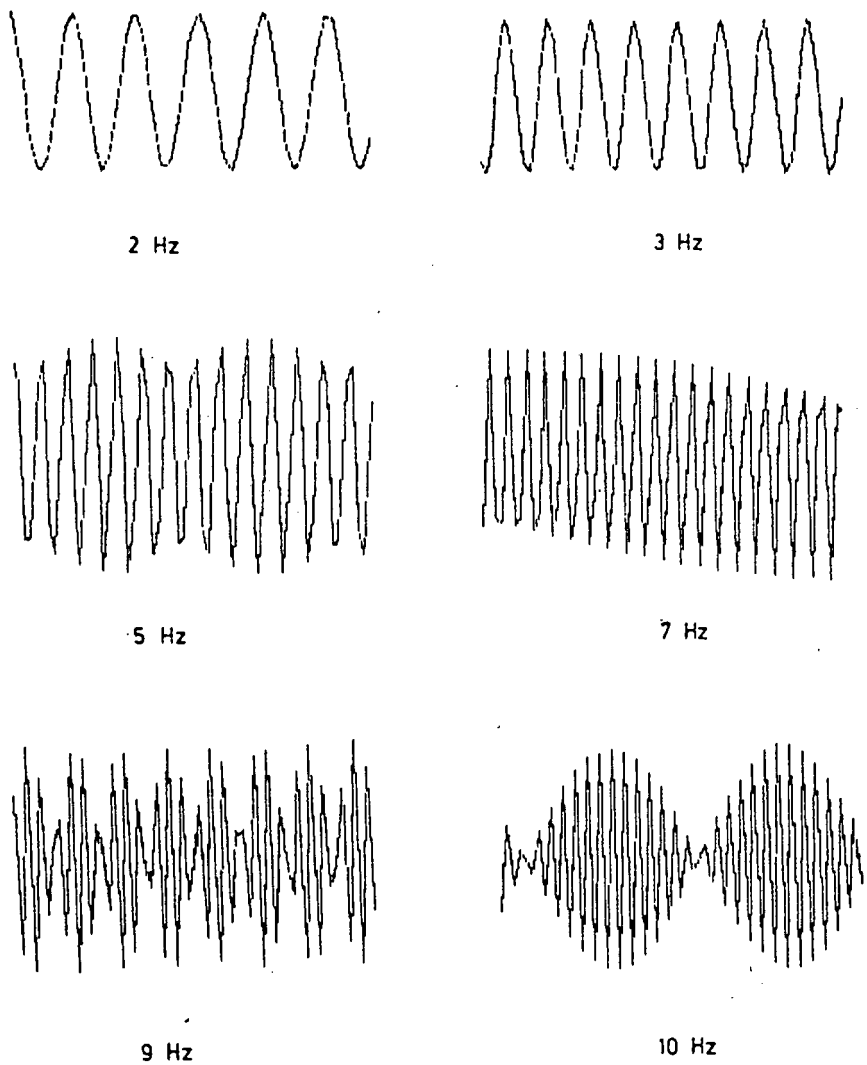


Figure 3.14 Resultant cyclic strain traces, recorded in one buffer, as a function of the cyclic frequency.

It is clear that the estimation of a maximum and minimum value of strain would not be reliable at frequencies greater than 3 Hz. Since a perfectly acceptable trace is obtained at 1 Hz, the test frequency for the environmental tests was not influenced. However, the greater frequency of 10 Hz, used to reduce testing durations in air (rate of cracking in 'inert' environments is independent of frequency), could not be employed with this particular data aquisition system. A frequency of 3 Hz proved to give a reasonable trace and consistently accurate maxima and minima and, since a frequency higher than that employed for the environmental testing was sought so as not to increase the test durations more than was necessary, all air fatigue tests were performed at this frequency.

### 3.2.3.3 Software Control of Data Aquisition

A computer programme was developed to control the strain input via the data aquisition unit, and to process this raw data to obtain estimates of crack length. The data processing involves the transfer of 4 buffers (60 readings each) to the computer where the limits are determined. A second and third channel on the data logger are used to read the current strain gauge excitation voltage and an output voltage from the temperature compensating gauge. The strain range ($\varepsilon_{max}$ - $\varepsilon_{min}$) is calculated using the previously determined limits and the instantaneous excitation voltage; any effects of temperature are then taken into account. The final value of the range of strain is then used to derive values of the crack length using equations 1 and 2 of section 3.2.3.1.

The entire cycle has a duration of 36 seconds. For approximately every 0.25 mm crack advancement, the values of crack length and time are stored in an array in the computer memory and printed on the internal printer of the computer, ensuring a hardcopy backup of the results. At the completion of a test, the arrayed data in the memory is stored on disk to await further analysis. A basic flowchart of the software operation is shown in fig. 3.15 and the listed programme is given in Appendix A.

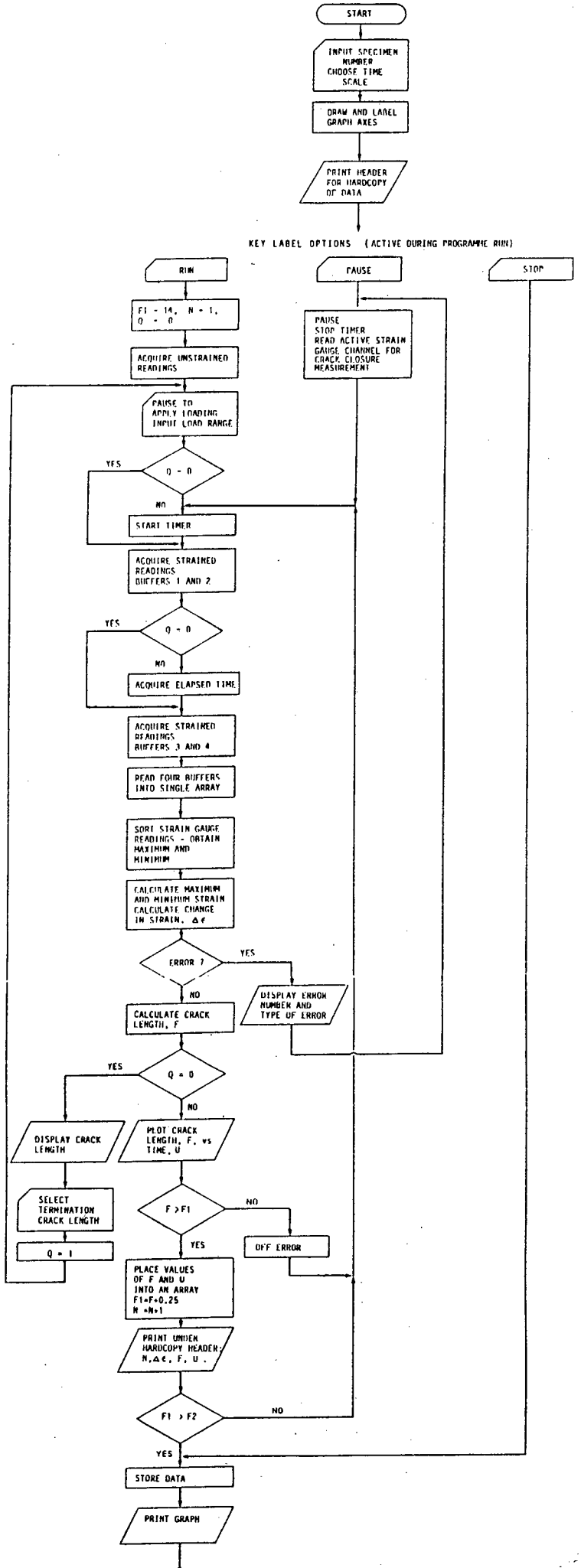
START
INPUT SPECIMEN NUMBER
CHOOSE TIME SCALE
DRAW AND LABEL GRAPH AXES
PRINT HEADER FOR HARDCOPY OF DATA
KEY LABEL OPTIONS (ACTIVE DURING PROGRAMME RUN)
RUN
PAUSE
STOP
F1 = 14, N = 1, Q = 0
ACQUIRE UNSTRAINED READINGS
PAUSE TO APPLY LOADING INPUT LOAD RANGE
Q = 0
YES
NO
START TIMER
ACQUIRE STRAINED READINGS BUFFERS 1 AND 2
Q = 0
YES
NO
ACQUIRE ELAPSED TIME
ACQUIRE STRAINED READINGS BUFFERS 3 AND 4
READ FOUR BUFFERS INTO SINGLE ARRAY
SORT STRAIN GAUGE READINGS - OBTAIN MAXIMUM AND MINIMUM
CALCULATE MAXIMUM AND MINIMUM STRAIN CALCULATE CHANGE IN STRAIN, Δε
ERROR ?
YES
NO
DISPLAY ERROR NUMBER AND TYPE OF ERROR
CALCULATE CRACK LENGTH, F
Q = 0
YES
NO
DISPLAY CRACK LENGTH
PLOT CRACK LENGTH, F, vs TIME, U
SELECT TERMINATION CRACK LENGTH
Q = 1
F > F1
NO
YES
OFF ERROR
PLACE VALUES OF F AND U INTO AN ARRAY F1=F+0.25 N =N+1
PRINT UNDER HARDCOPY HEADER: N, Δε, F, U .
F1 > F2
NO
YES
PAUSE
STOP TIMER
READ ACTIVE STRAIN GAUGE CHANNEL FOR CRACK CLOSURE MEASUREMENT
STORE DATA
PRINT GRAPH

### 3.2.4 Data Analysis

The data stored at the completion of each test is analysed using the 7 point polynomial technique of converting crack length a, as a function of number of cycles N, to fatigue crack growth rate da/dN, vs. stress intensity factor range $\Delta K$. The $\Delta K$ is calculated from the equation for CT specimens, given in reference 117. Another computer programme was developed for this operation. A listing of the programme is given in Appendix A along with an example of the data printout obtained from the analysis.

### 3.2.5 Reproducibility of FCGR Curves

To confirm the validity of the test method, data aquisition, and data analysis, a number of tests were repeated using mild steel specimens in air. The results, shown in figure 3.16, exhibited exceptional reproducibility for a procedure that is notorious for variability. These results served to increase confidence in the test methods employed in the investigation.

A further test, using mild steel in air, was repeated towards the completion of the test programme, after a major overhaul of the servo-hydraulic equipment. The results compared well with those of fig. 3.16.

Repeat tests were also performed on each test material in selected environments to check the reproducibility of the fatigue crack growth behaviour in aqueous environments. The results of these repeat tests will be presented and discussed along with the results of the primary tests in chapters 4 and 5.

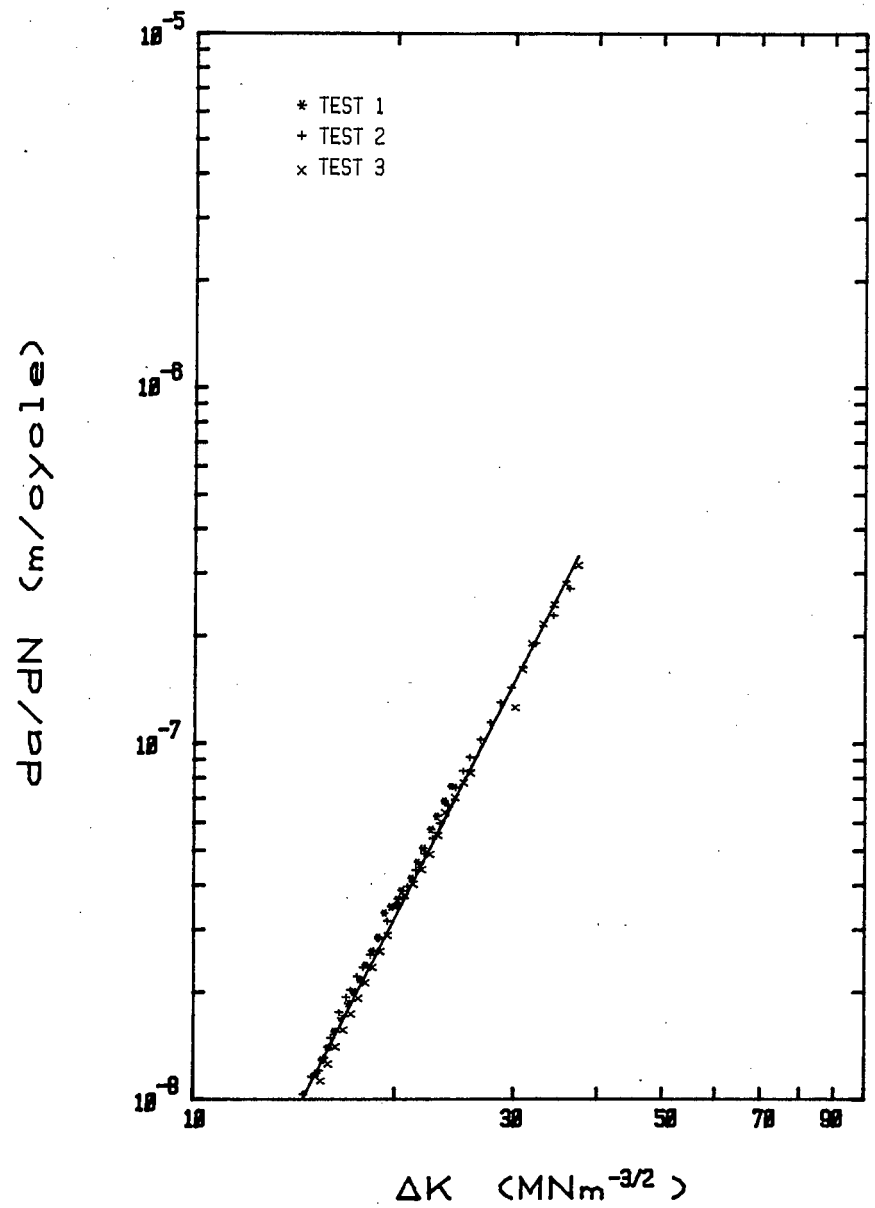


Figure 3.16 FCGR curves of three mild steel specimens tested in air, showing good reproducibility.

### 3.2.6 Crack Closure Measurements

Crack closure measurements were performed on all the repeat tests. Preliminary work was conducted on a mild steel specimen that contained a substantial crack, and showed evidence of plasticity on the polished sides of the specimen. The crack closure (plasticity induced) was measured conventionally by recording the crack opening displacement, by means of a calibrated clip gauge, versus the cyclic load.

This output was compared with that from the back face strain gauge (strain versus cyclic load) in an attempt to find an alternative means of estimating crack closure owing to the unsuitability of the existing environmental chamber to the use of a clip gauge.

Similar traces were obtained for both methods, figure 3.17, and equal estimates of the load at which the crack opened on the loading portion of the cycle were gained. Henceforth the BFS gauge was used to estimate the crack closure.

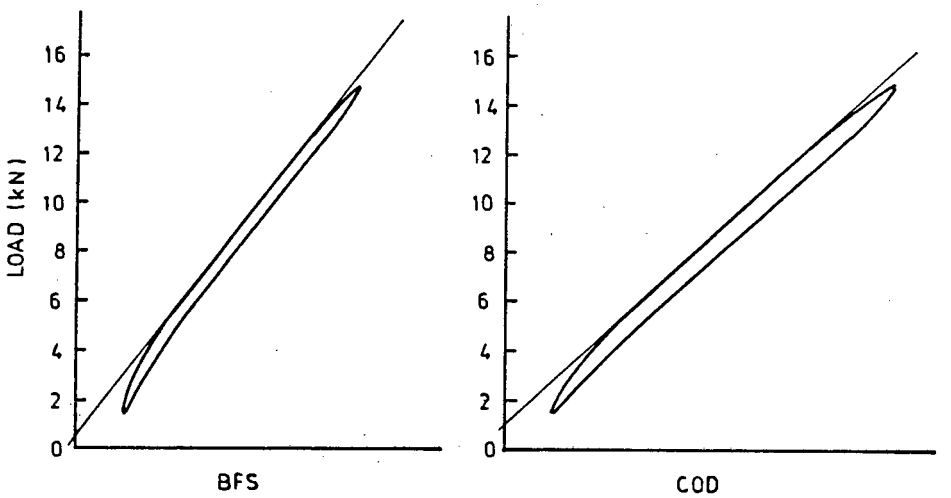


Figure 3.16 A comparison of the outputs from a BFS gauge and the crack opening displacement (COD) of a clip gauge as a function of load.

The crack closure measurements necessitated interrupting the cyclic loading in order to apply a ramp loading between loads of 1.5 and 16 kN whilst recording the strain output from the back face. Due to the possible onset of transient effects caused by the unloading, the number of interruptions was kept to a minimum and, as a result, an average of four closure measurements were carried out per test.

The degree of closure is reported as a 'Closure Index' which is the quotient of the maximum load, $P_{max}$ and the load at which the crack is deemed to have opened, $P_{cl}$.

### 3.2.7 Fracture Surface Preparation

A number of the tests performed in the aqueous solutions resulted in the deposition of dense layers of corrosion product onto the fracture surface which was not easily removed by treatment in the ultrasonic bath. In the initial stages of the programme,

# CHAPTER 4

# RESULTS

## 4.1 FATIGUE CRACK GROWTH RATES (FCGRs)

### 4.1.1 Fatigue in Air

A graph depicting the fatigue behaviour of the five materials tested in laboratory air at a frequency of 3 Hz is presented in fig. 4.1.

The martensitic Alloy 825 clearly exhibits less resistance to fatigue crack propagation than the other alloys. The greatest resistance to fatigue crack propagation was shown by 1210, in which the stress induced transformation of the metastable austenite to a nitrogen strengthened martensite takes place at the crack tip.

The differences in the FCGRs in mild steel, 3CR12 and AISI 431 become negligible as the cracks approach instability; the same could be said of a reasonable extrapolation of the 1210 data. It is interesting to note that the individual curves each possess a different slope (parameter 'n' of the Paris equation).

Linear, Stage II crack propagation behaviour is displayed by the steels that exhibit a moderate to good resistance to fatigue crack propagation, while the Stage II behaviour of Alloy 825 is sigmoidal. This should not to be confused with the sigmoidal nature of the characteristic FCGR curve that includes Stage I and stage III cracking.

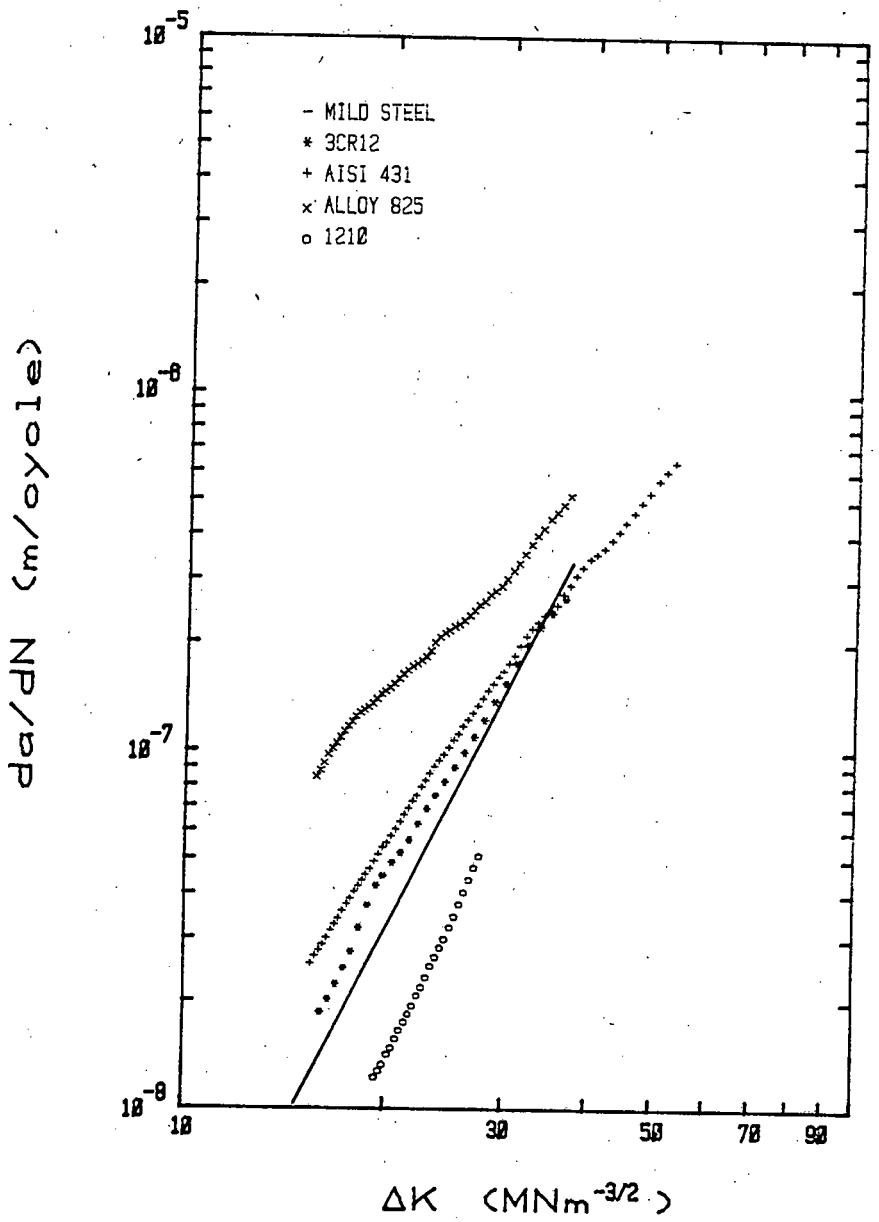


Figure 4.1 FCGR behaviour of the five steels tested in laboratory air.

### 4.1.2 Mild Steel in Aqueous Environments.

The FCGRs recorded for mild steel in the various aqueous environments, and the air fatigue line derived from figure 3.16 are illustrated in figure 4.2. The results generally indicate a decrease in FCGRs with a decrease in the chloride content of the electrolyte; a lower crack growth rate is also observed by the rest potential tests with respect to the polarised environment. The distilled water test, however,

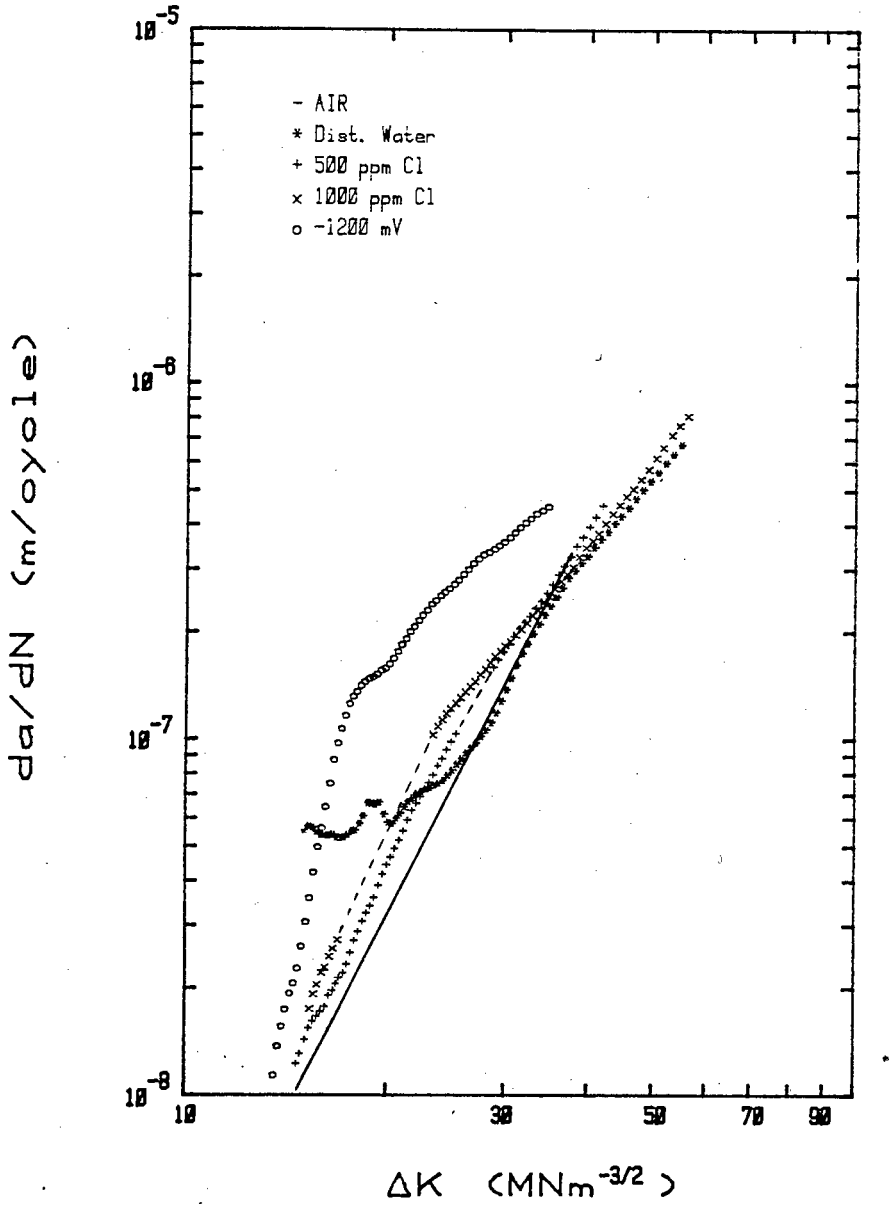


Figure 4.2 Influence of aqueous environments on the FCGR behaviour of mild steel. Note that the results obtained in the 1000 ppm chloride solution, held at -1200 mV are so called '-1200 mV' in the legends of all the figures pertaining to the FGCRs.

showed a FCGR plateau at a rate which was far in excess of the rates observed in the other environmental tests at corresponding ΔK levels. The dotted lines in figure 4.2 represent an extrapolatory connection between two sets of data in a region where data was lost due to interruptions during the test.

A repeat test performed in distilled water shows that tests in this environment are subject to some scatter which was not evident for tests in air (fig. 4.3).

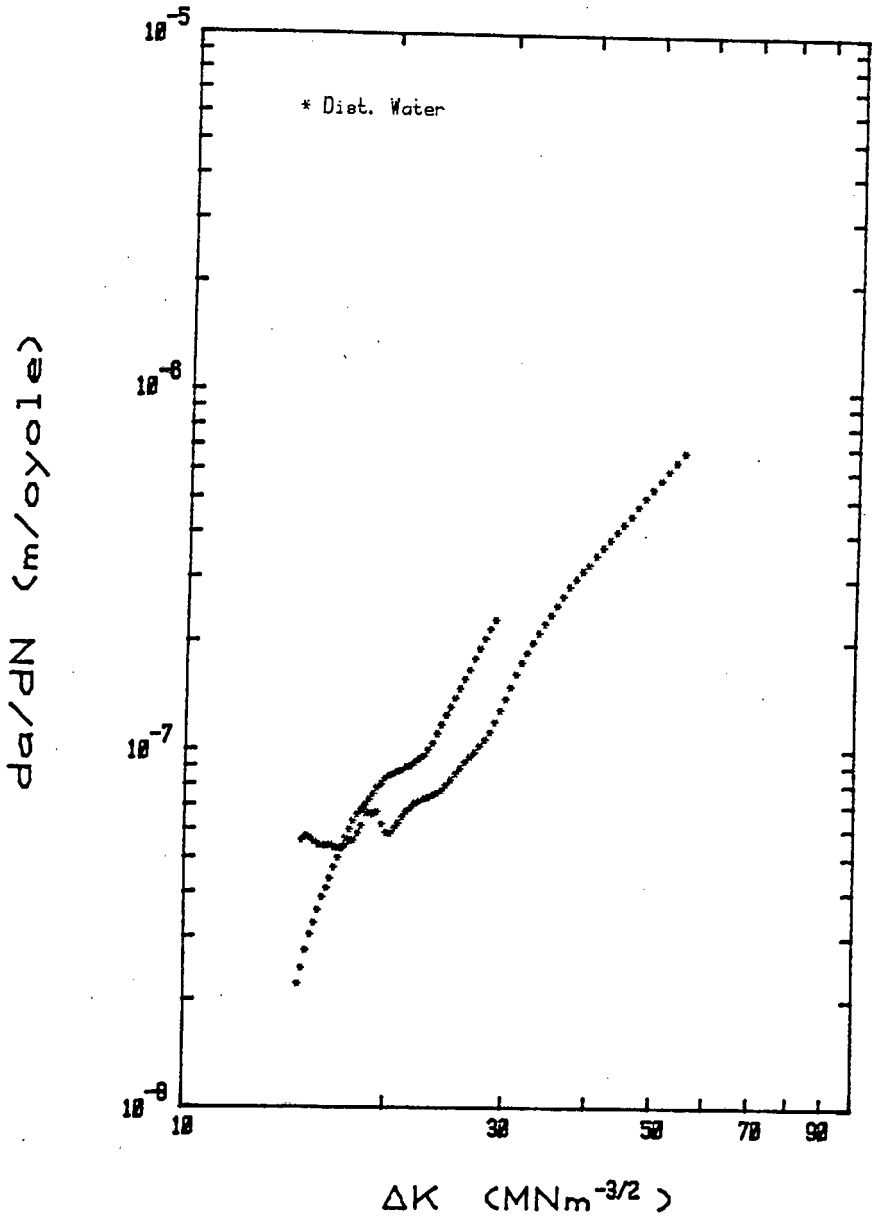


Figure 4.3 Reproducibility of FCGR testing of mild steel in distilled water.

A further repeat test was performed on mild steel in the 1000 ppm chloride solution at rest potential but was not completely successful. Results were obtained at low ΔK levels but were not adequate to be included in figure 4.3. However, it is sufficient to say that these results were also subject to some scatter, but lay within a band bounded by the initial results obtained from tests in distilled water and the 1000 ppm chloride solution at a rest potential.

### 4.1.3 3CR12 in Aqueous Environments.

The FCGR properties of 3CR12 tested in air and at free corrosion potentials in distilled water, 500 ppm chloride solution, and 1000 ppm chloride solution are shown in fig. 4.4. In addition, the data obtained from a specimen held at -1200 mV in the 1000 ppm chloride solution is presented. Similar FCGRs were obtained between stress intensities of about 15 and 25 $MNm^{-3/2}$ for the aqueous

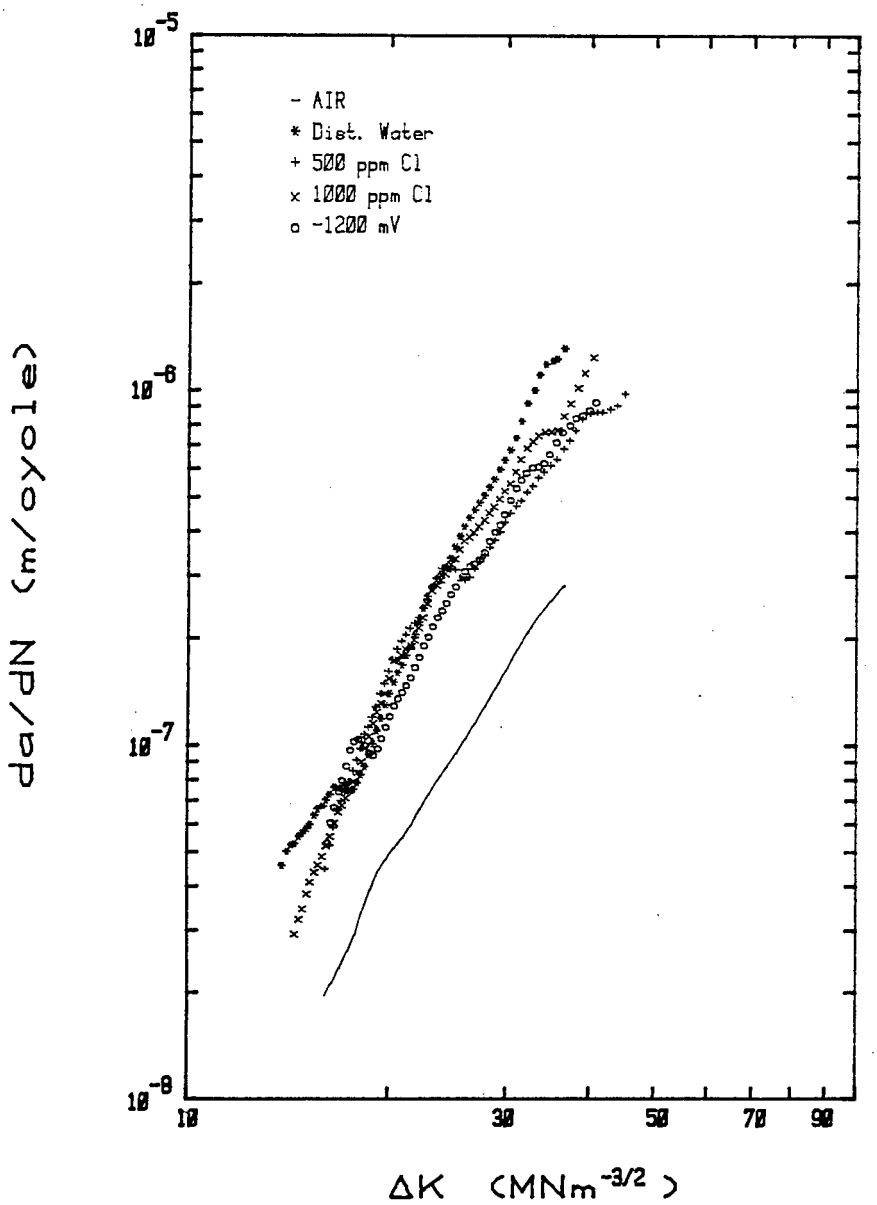


Figure 4.4 Influence of aqueous environments on the FCGR behaviour of 3CR12.

environmental tests. Differences in relative performance are seen above and below these values of stress intensity. In addition these FCGR curves exhibited a number of small 'plateaux'. The significance of these plateaux will be addressed in the next chapter.

A repeat test in the distilled water solution shows that there is quite good reproducibility for that particular system (fig. 4.5). Owing to the encompassment of all the environmental FCGR data within a narrow band, further repeat tests were not considered necessary.

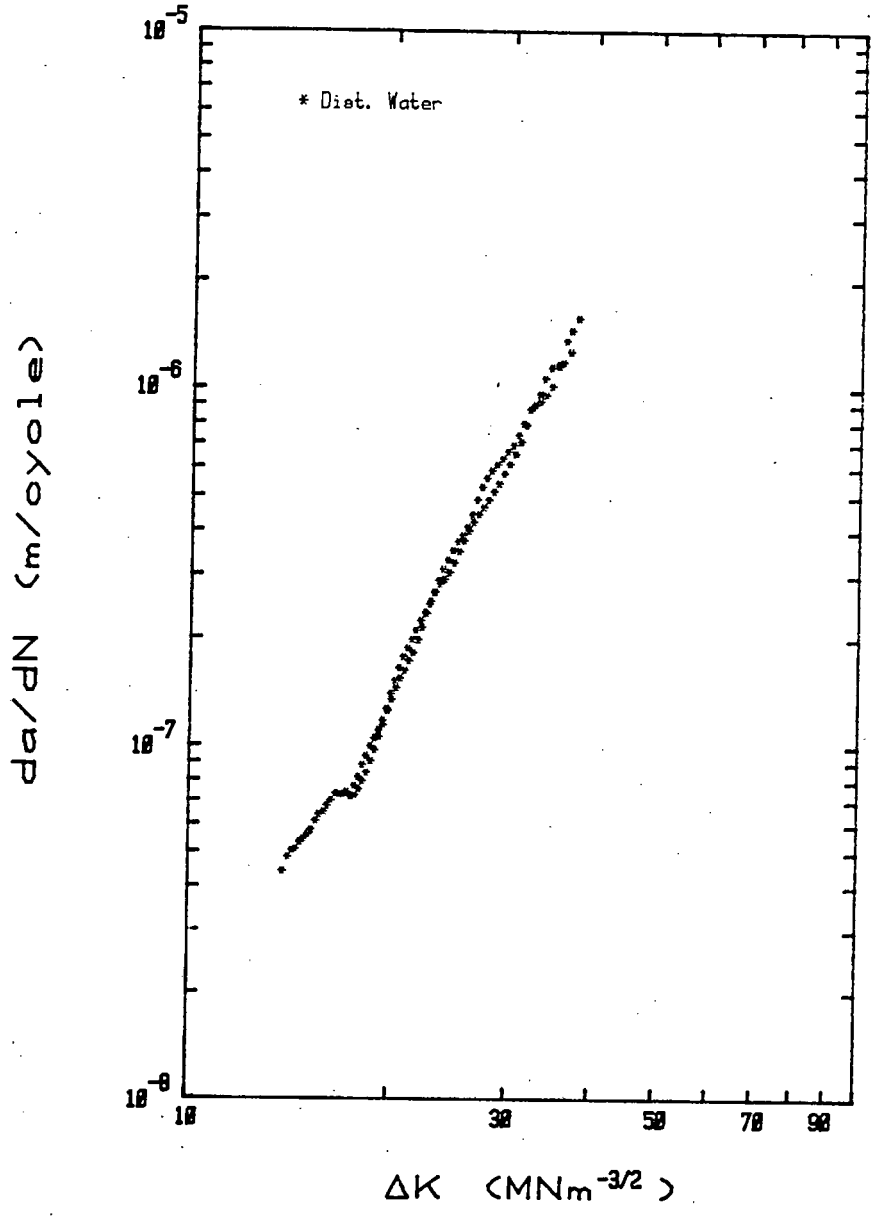


Figure 4.5 Reproducibility of FCGR testing of 3CR12 in distilled water.

### 4.1.4 AISI 431 in Aqueous Environments

The results obtained for AISI 431 tested at rest potentials in the aqueous solutions (fig. 4.6), exhibited a decrease in the FCGRs with an increase in the chloride content of the solutions; FCGRs were greatly enhanced with respect to the rate of fatigue crack propagation in air. The test in the 1000 ppm chloride solution held at -1200 mV exhibited the greatest rate of cracking.

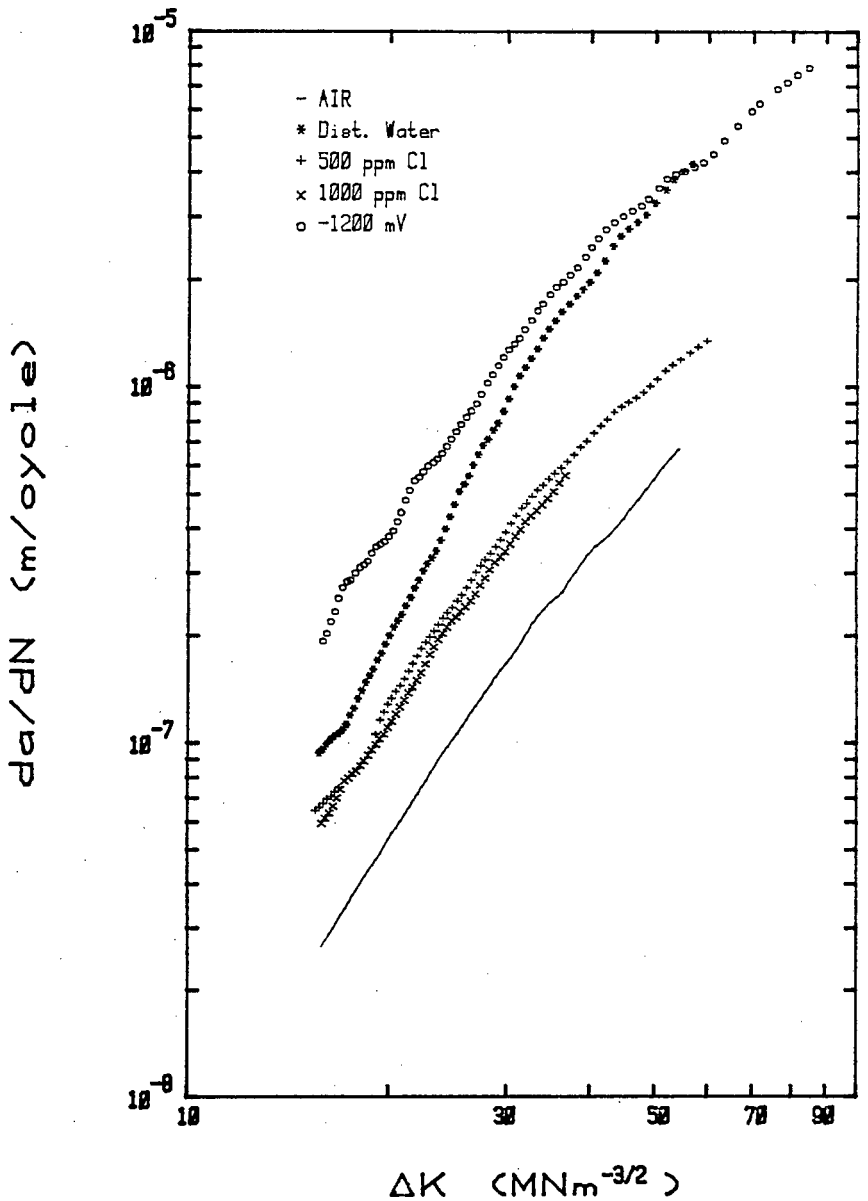


Figure 4.6 Influence of aqueous environments on the FCGR behaviour of AISI 431.

Repeat tests in distilled water and the 1000 ppm chloride solution are shown in fig. 4.7. It is clear that the distilled water results are quite reproducible whilst significant scatter is shown by the 1000 ppm chloride solution. Nevertheless it is safe to infer that the introduction of chloride ions into the solution has resulted in a dramatic decrease in FCGRs with respect to the distilled water results, particularly at high ΔK levels.

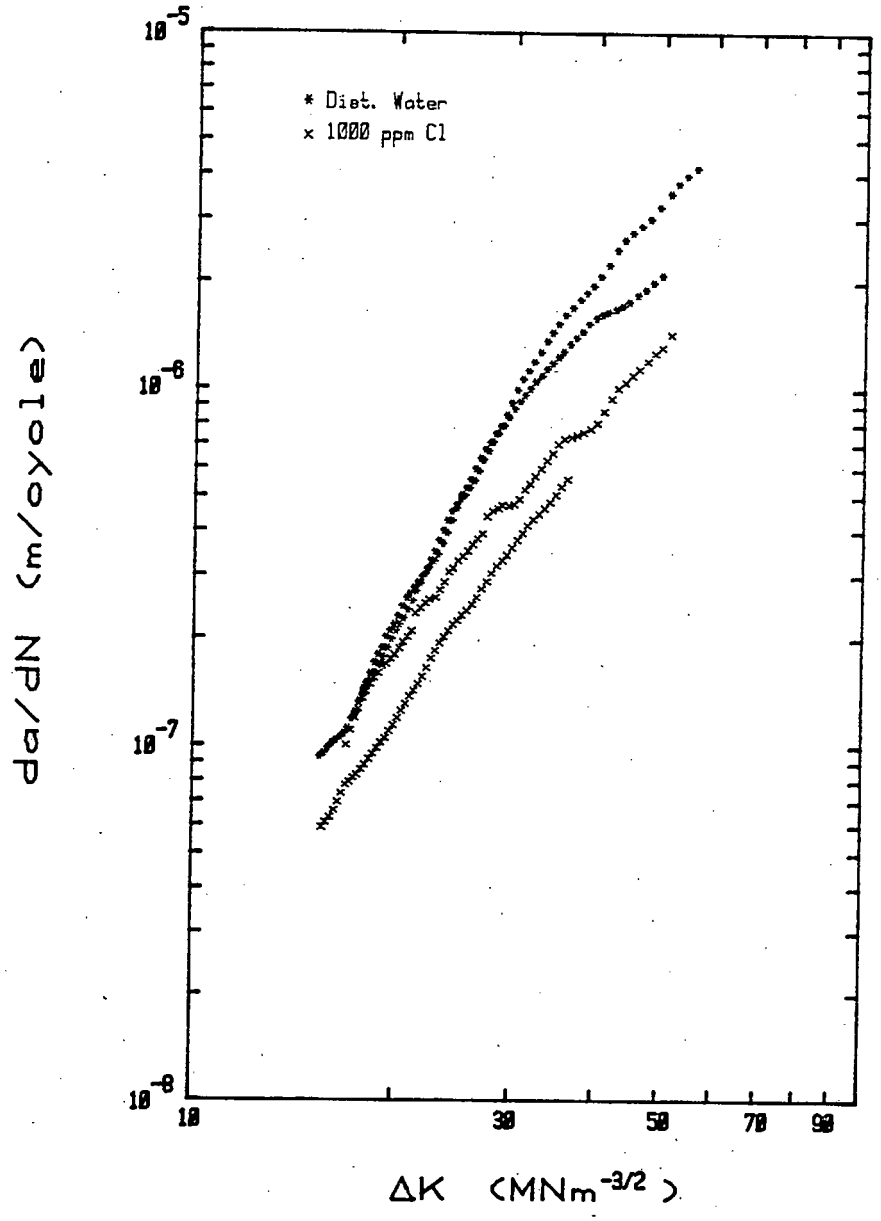


Figure 4.7 Reproducibility of FCGR testing of AISI 431 in distilled water and 1000 ppm chloride solution.

### 4.1.5 Alloy 825 in Aqueous Environments.

The FCGRs of Alloy 825 were significantly greater in the aqueous environments than in air (fig. 4.8). The alloy exhibited reduced FCGRs with an increase in chloride content of the aqueous solutions, although no significant difference between the FCGRs in distilled water and the 500 ppm chloride solution was observed; similarly no significant difference between the 1000 ppm chloride solutions (rest potential and -1200 mV) can be seen. The dotted line on the -1200 mV curve once again indicates an interruption during testing which resulted in the loss of data.

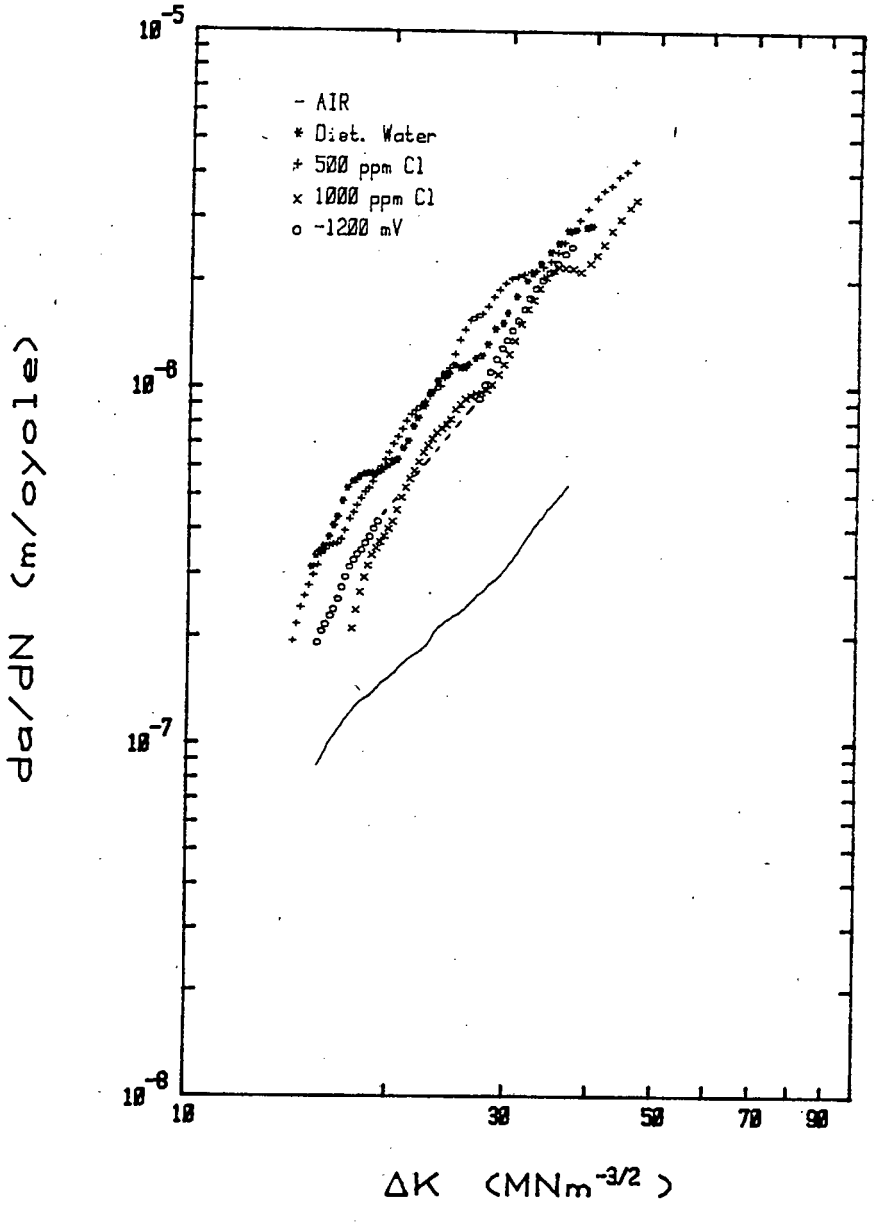


Figure 4.8 Influence of aqueous environments on the FCGR behaviour of Alloy 825.

Reproducibility tests on Alloy 825 were performed in distilled water and the 1000 ppm chloride solution and the results are shown in figure 4.9. The repeat test results differ to the initial results in that both repeat tests have resulted in a significant FCGR retardation with respect to the initial data. Two possible reasons can be forwarded for this occurrence: i) inherent variability of fatigue testing, and ii) differing batch heat treatments.

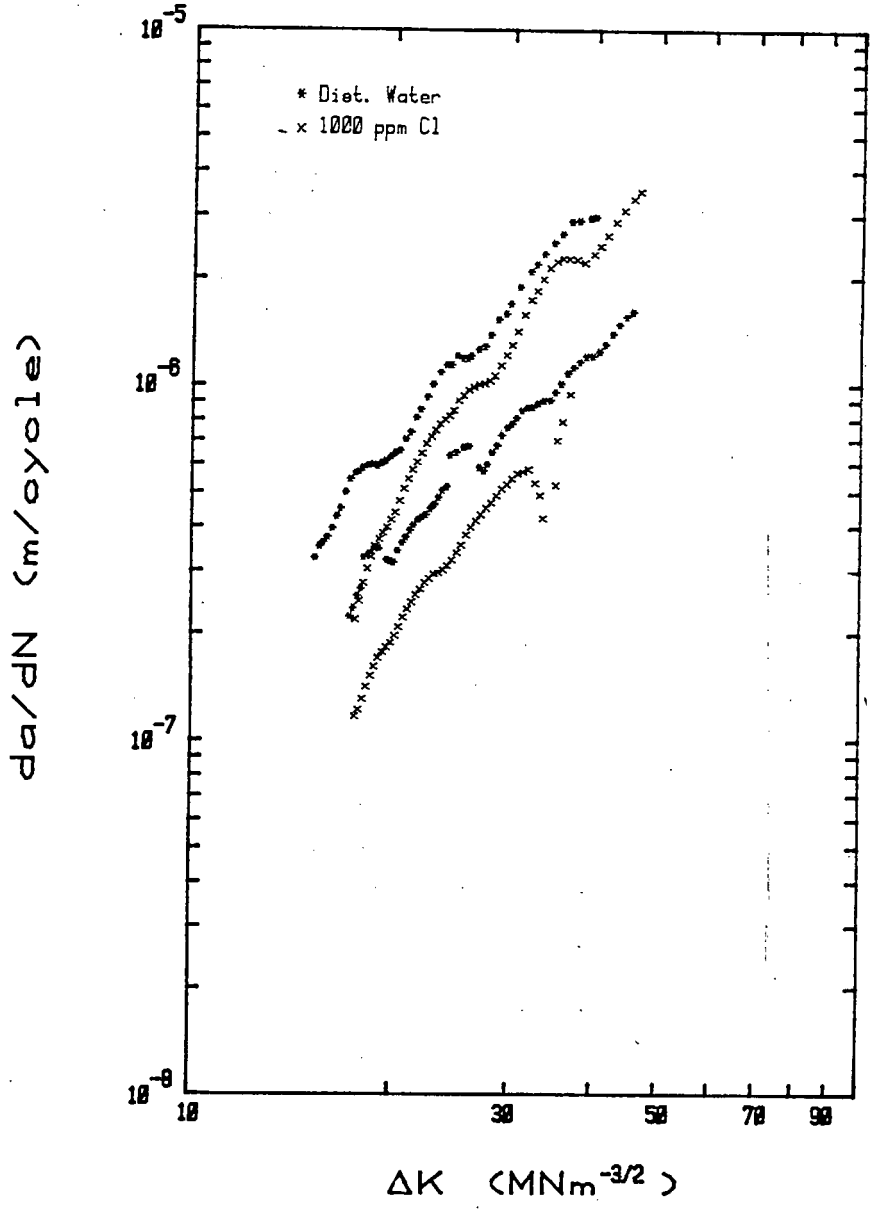


Figure 4.9 Reproducibility of FCGR testing of Alloy 825 in distilled water and 1000 ppm chloride solution.

### 4.1.6 1210 in Aqueous Environments.

The FCGR behaviour of 1210 in air and in the aqueous environments is depicted in figure 4.10. The aqueous environments have had a significant influence on the fatigue crack propagation behaviour of 1210, with FCGRs approaching 30 times those obtained in air at low ΔK levels. The data shows no direct trend that relates degree of enhancement with apparent aggressiveness of the environment. The

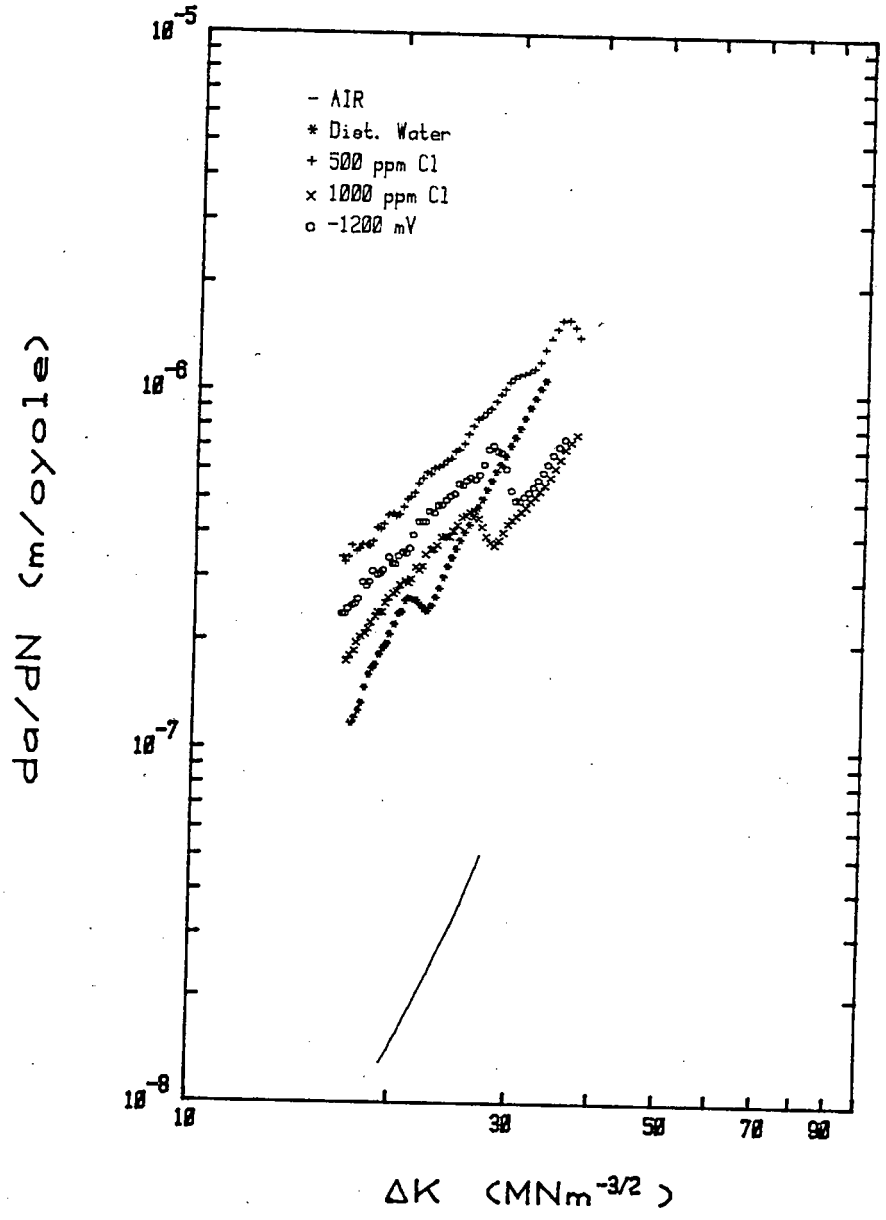


Figure 4.10 Influence on aqueous environments on the FCGR behaviour of 1210.

'apparent aggressiveness' refers to the expected degree of influence of the various environments on the corrosion fatigue behaviour, and is as follows: distilled water < 500 ppm chloride < 1000 ppm chloride < 1000 ppm chloride, -1200 mV. The FCGRs in the 500 ppm chloride solution were clearly greater than those obtained in distilled water and the 1000 ppm chloride solution at a rest potential; a slight increase in the FCGRs resulted from the test performed at -1200 mV, compared to the rest potential data. The FCGR curves show a significant drop at apparently random ΔK levels, after which the curves resume an upward trend with identical slopes to those exhibited prior to the drop; the exception is the 500 ppm chloride data, where the drop occurred near the termination of the test.

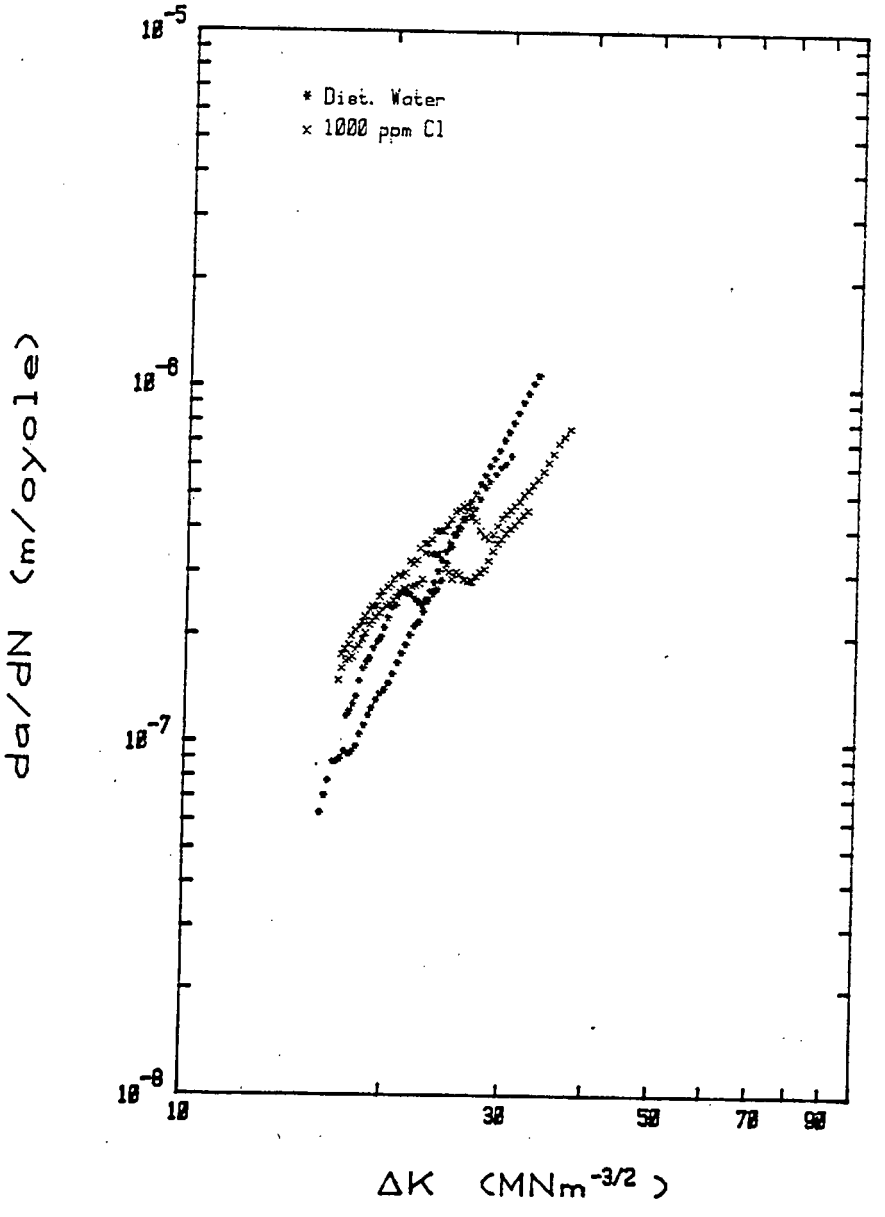


Figure 4.11 Reproducibility of FCGR testing of 1210 in distilled water and 1000 ppm chloride solution.

The repeat tests, presented in figure 4.11, indicate that there is not much variability in the FCGRs for this alloy in the environments used. The distilled water repeat test shows the most variability, where the rate of crack propagation at low ΔK levels is lower than that observed in the first test. The FCGRs of 1210 in the 1000 ppm chloride solution did not differ much, but the position of the FCGR discontinuity was displaced with respect to the initial data.

### 4.1.7 Relative Fatigue Crack Growth Rates.

The original aim of the project was to compare the relative behaviour of the five alloys in air and the aqueous environments. To simplify this task, and to make the results more meaningful to the layman, crack growth rates at two ΔK levels were calculated, relative to mild steel in air as follows:

$$(da/dN)_{relative} = \frac{(da/dN)_{alloy/environment}}{(da/dN)_{mild\ steel/air}}$$

The relative crack growth rates, or crack growth rate indices, were evaluated for ΔK levels of 16 and 35 $MNm^{-3/2}$ and provide an indication of the differences in FCGRs at low and high stress intensities. These results have been presented in the form of cluster bar charts, with two permutations for each ΔK level (figs. 4.12 and 4.13). Note that extrapolations of the FCGR data have been made where necessary. A number of trends can be observed at $\Delta K = 16\ MNm^{-3/2}$:

1. Mild steel exhibits the lowest overall growth rates while Alloy 825 shows the highest.
2. Distilled water is generally the most aggressive environment for the ferritic and martensitic alloys; the 500 ppm chloride solution is also particularly aggressive and clearly the most deleterious environment for 1210. The 1000 ppm chloride solution is the least deleterious of all the aqueous environments.
3. The crack growth rate indices of mild steel and AISI 431 under the polarised condition are greater than those indices obtained under rest potential conditions. Under the polarised conditions Alloy 825 and 1210 exhibit comparable crack growth rate indices to AISI 431 but these indices, in most cases, are less than those estimated for the materials under rest potential conditions.
4. The crack growth rate indices for the martensitic and austenitic alloys under the cathodically polarised conditions are unexpectedly low.

At a higher ΔK level many of these trends remain:

5. Mild steel continues to exhibit the lowest overall rate of cracking and Alloy 825 continues to exhibit the highest overall rate.

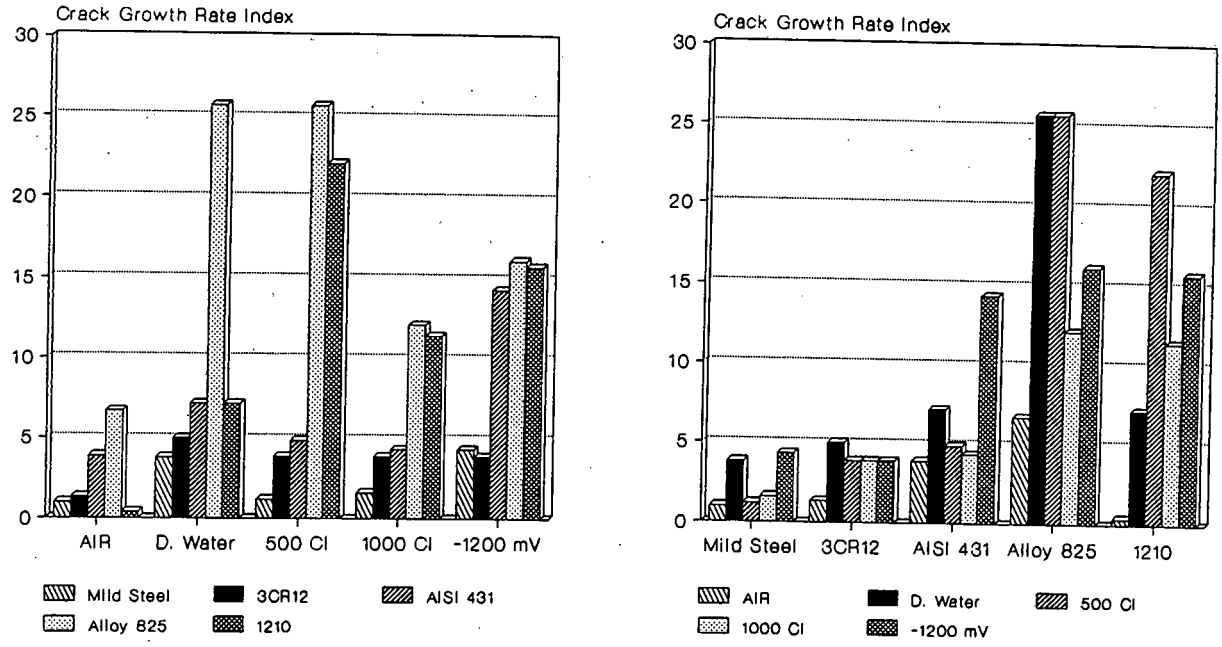


Figure 4.12 Crack growth rate indices at $\Delta K = 16\ MNm^{-3/2}$.

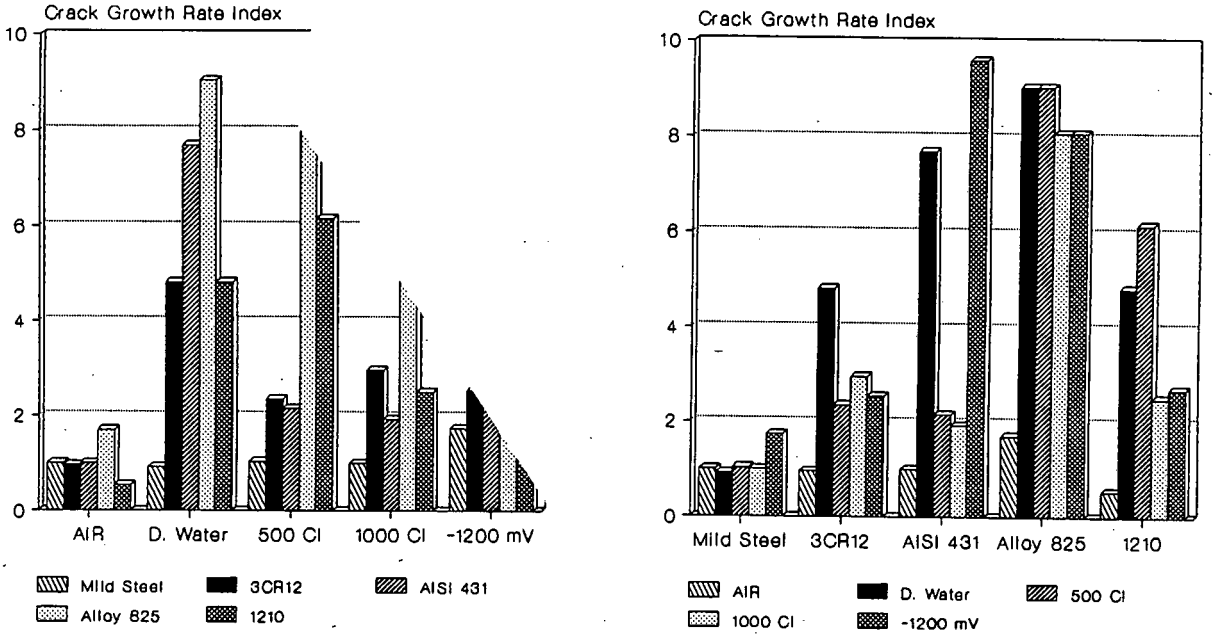


Figure 4.13 Crack growth rate indices at $\Delta K \cong 35\ MNm^{-3/2}$.

6. Distilled water remains the most aggressive environment. The effect of chloride additions is diminished in that the indices in the 1000 ppm chloride solutions at rest potential are comparable to those in the 500 ppm chloride solutions. The influence of the cathodic polarisation is more pronounced, with respect to the rest potential indices.

### 4.1.8 EAC Index

The data can be presented in terms of an Environmentally Assisted Cracking Index (so called EAC Index). This index is determined by relating the FCGRs of a material/environment system at a specific $\Delta K$ level to the FCGR for the same material in air, i.e. the indices of all alloys in air are unity.

The values are presented in figs. 4.14 and 4.15 for the two $\Delta K$ levels. When the indices of the different alloys are compared for each environment a number of trends become evident. At low $\Delta K$ levels:

1. The ferritic and martensitic alloys are all subject to a similar degree of crack growth enhancement while 1210 suffers a significantly larger degree of crack growth enhancement.
2. Cracking in mild steel was least influenced by the environment while cracking in 1210 was influenced to the greatest extent.
3. Distilled water results in the greatest environmental effect on the ferritic and martensitic alloys; the chloride containing solutions at rest potentials show similar indices for these alloys.
4. The EAC indices for the cathodically polarised tests are unexpectedly low.

At a higher $\Delta K$ level:

5. Mild steel continues to show the lowest EAC indices and 1210 continues to show the highest.
6. The differences between the f.c.c. 1210 and the other alloys is reduced.
7. The influence of distilled water on the ferritic and martensitic alloys is more pronounced at this higher $\Delta K$ level.
8. The degree of EAC of AISI 431 in distilled water and under the cathodically polarised condition is noticeably greater than that in the other environments and is greater than the degree of EAC observed at the lower $\Delta K$ level.

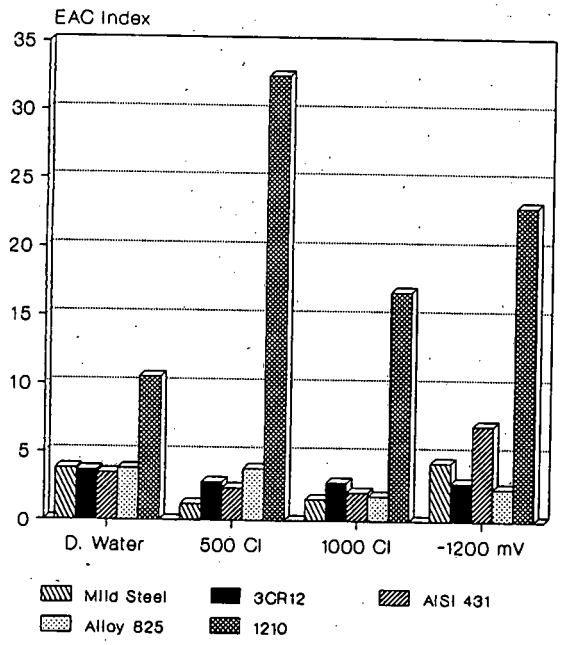


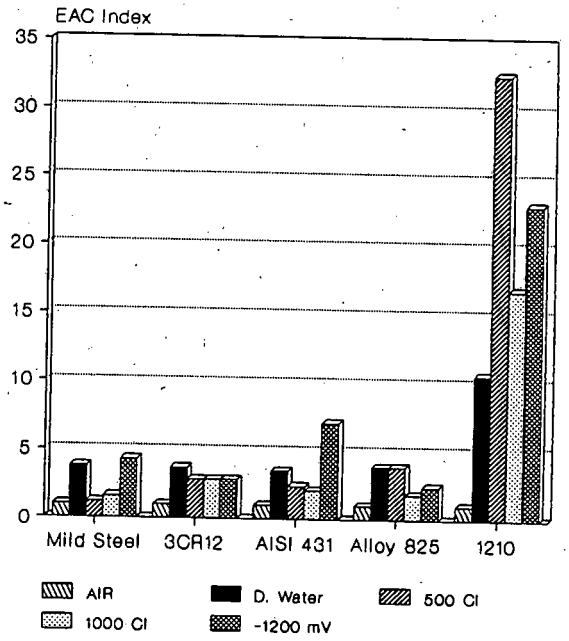


Figure 4.14 EAC indices for $\Delta K = 16\ MNm^{-3/2}$.

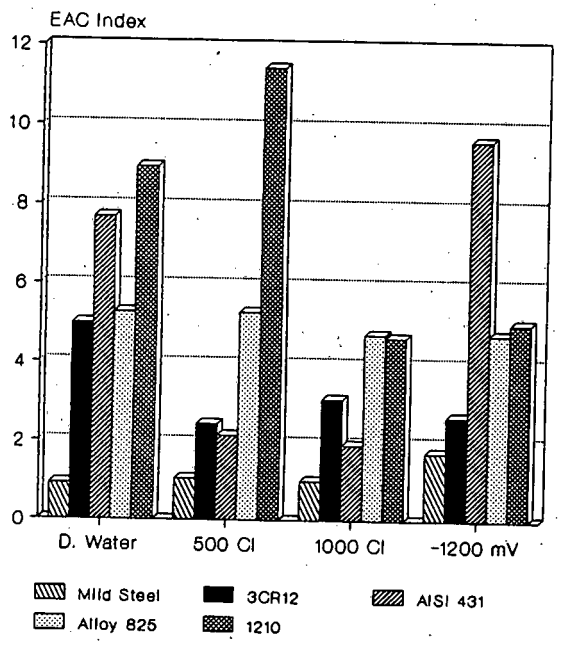


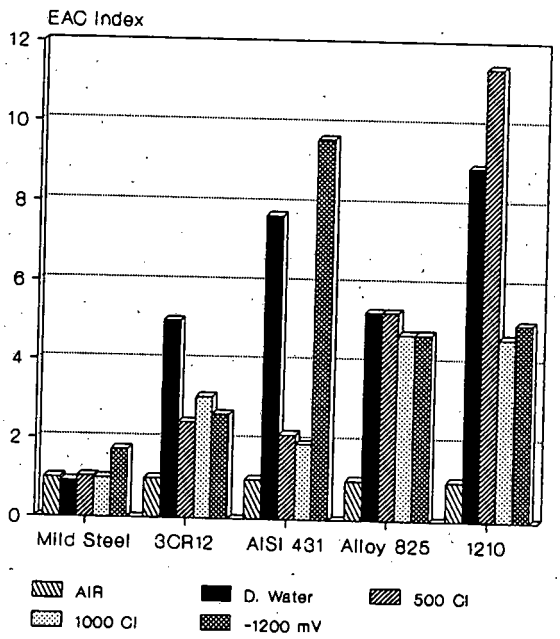


Figure 4.15 EAC indices for $\Delta K = 35\ MNm^{-3/2}$.

## 4.2 FRACTOGRAPHY

The fracture surfaces from each test specimen were studied using a SEM in an effort to relate fracture mode changes to changes in FCGR behaviour. In this section, the fracture surface morphologies of each alloy resulting from tests in air and the aqueous environments will be illustrated. Morphologies or fracture modes will be related to the FCGR behaviour in the next chapter.

Note that the figure captions of the fractographs include an approximate value for the corresponding $\Delta K$ level. The positions at which the fractographs were taken were carefully recorded using a calibrated specimen stage on the SEM. The quoted values of $\Delta K$ represent the approximate macroscopic $\Delta K$ at the point of recording corresponding to the macro crack length. The figures representing the fractography resulting from tests in the aqueous environments include a schematic illustration of the plan view of the fracture surfaces, indicating the relative locations at which the fractographs were recorded, and the crack front curvature at the completion of each test. These schematic illustrations are described in fig. 4.16. A second crack front in fig. 4.22 indicates a region where the environment was removed and the fatigue loading continued for a short period before the specimen was fully fractured. The macroscopic crack propagation direction for all fractographs is from top left to bottom right, as indicated in fig. 4.17, unless otherwise noted.

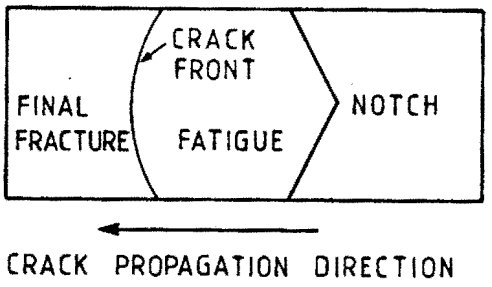


Figure 4.16 Schematic illustration of the plan view of a typical fracture surface.

It was considered likely that a certain amount of bias could occur in the fractographic analysis as a result of prior knowledge of the FCGR / $\Delta K$ relationship for each alloy and environment. To overcome the possibility of bias, fracture surfaces were examined in some detail before the FCGR curves were studied. However, a number of surfaces were re-examined to confirm or to search for trends that might provide explanation for anomalous FCGR behaviour.

During the fractographic examination a number of fracture modes were identified, namely: ductile transgranular cracking, striation formation, fantail cleavage, crystallographic cleavage, quasi-cleavage, and intergranular separation. These modes are illustrated in fig. 4.17.

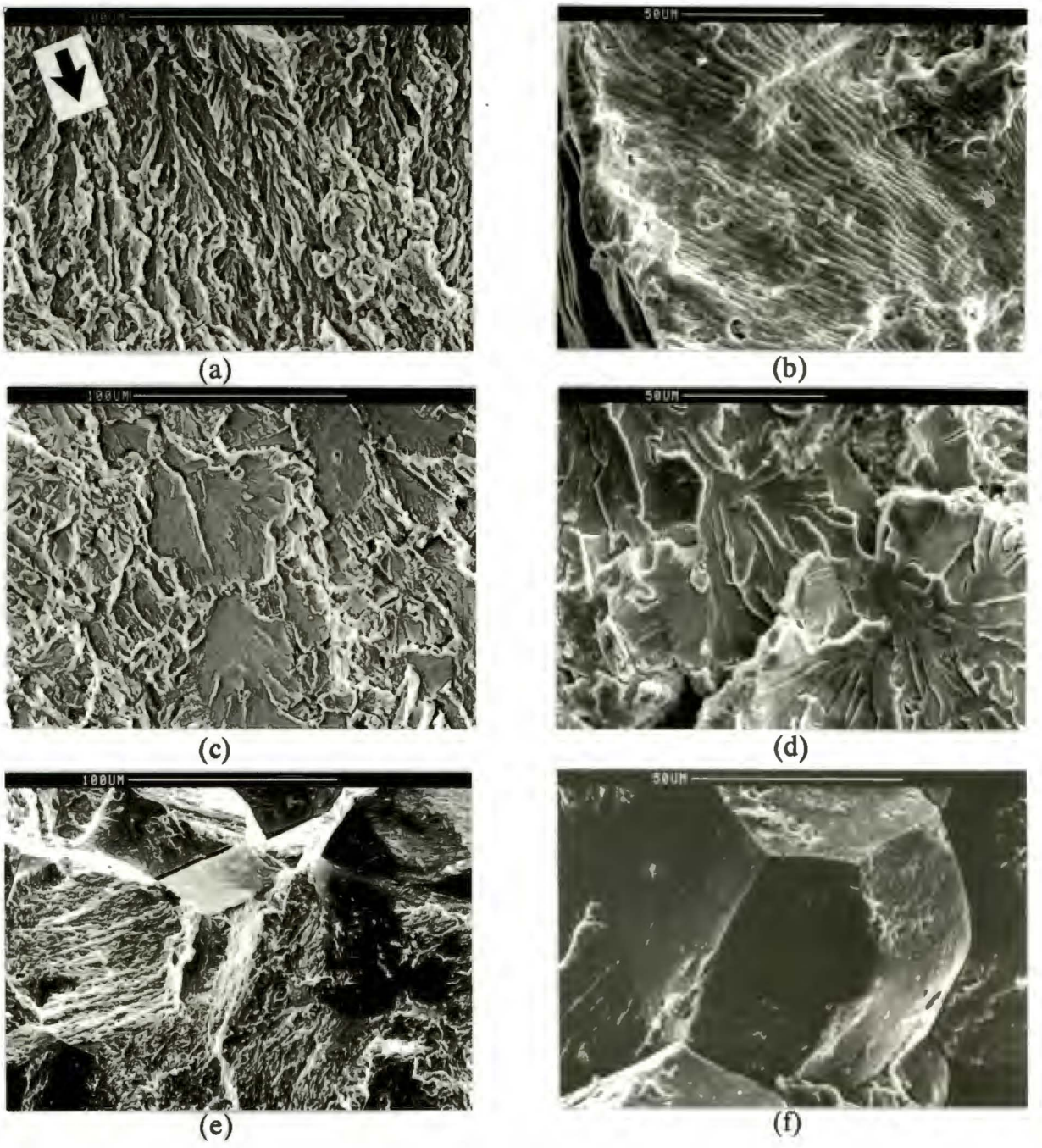


Figure 4.17 Modes of crack growth identified in this study: (a) feathery appearance of ductile transgranular cracking; (b) striation formation; (c) fantail cleavage; (d) crystallographic cleavage; (e) quasi-cleavage; (f) intergranular separation. The crack propagation direction is indicated by the arrow and is the same for all fractographs, unless otherwise stated.

Although the mechanism of the ductile transgranular cracking is expected to be identical to that giving rise to striation formation they are listed separately because the fracture appearances differ.

### 4.2.1 Mild Steel.

The fracture surface of mild steel tested in air is characterised by a ductile, uneven topography resulting from the propagation of microcracks in materials possessing numerous slip systems (fig. 4.18a). Fatigue striations became evident at high stress intensities where the crack advance per load cycle is expected to result in striations of a size readily resolvable in the SEM (fig. 4.18b).

There was an abrupt change in the morphology of the fracture at the onset of EAC in distilled water, where cracking occurred by a mixed intergranular and transgranular mode. Figure 4.19a shows the morphological change at the end of the precrack in air and the beginning of the crack propagated under the influence of distilled water. The intergranular facets (fig.4.19b) remained a dominant feature for a number of millimeters of fatigue crack propagation, after which the morphology gradually changed to a mixture of cleavage and transgranular cracking (Fig. 4.19c). The final stages of cracking resulted in a morphology showing a combination of ductile regions, cleavage and secondary cracking (fig. 4.19d). Note that the transgranular cracking observed at low $\Delta K$ levels had a "feathery" appearance (fig. 4.19a).

Environmentally assisted cracking of mild steel in the 500 ppm chloride solution resulted in a mixed intergranular and transgranular morphology (figs. 4.20a and b). Once again the transition from air fatigue (precrack) to EAC was sharp and clearly delineated on the fracture surface. This mixed mode cracking was dominant over the first two thirds of the fracture surface, after which there was a gradual change to transgranular cracking with a dispersion of isolated intergranular and "fantail" cleavage features (fig 4.20c) and an abundance of secondary cracking (fig. 4.20d).

The environmentally assisted fracture of the specimen tested in the 1000 ppm chloride solution was similar to that tested in the 500 ppm chloride solution. This was initially a mixed intergranular/transgranular mode ( figs. 4.21a and b) followed by ductile transgranular cracking with scattered incidences of cleavage (fig. 4.21c) and intergranular features, also with considerable secondary cracking (fig. 4.21d).

The onset of EAC in the 1000 ppm chloride solution held at -1200 mV manifested itself in the form of mixed intergranular / transgranular cracking (fig. 4.22a). This mode of cracking predominated only for a short while, after which the morphology changed to mixed transgranular cracking and "fantail" cleavage (figs. 4.22b and c).

The ratio of transgranular to cleavage changed through the specimen thickness; at the centre cracking was largely transgranular; at the edges cracking was almost entirely by cleavage. On removal of the environment, the cracking mechanism reverted back to a transgranular striation mode (fig. 4.22d).

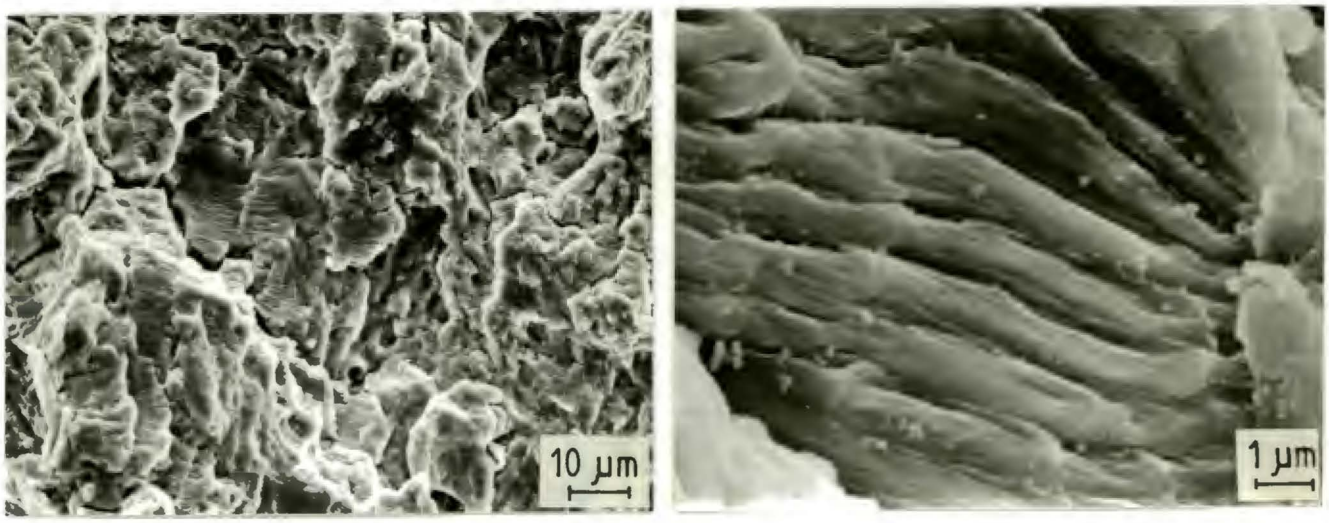


(a) (b)

Figure 4.18 Mild steel tested in laboratory air; (a) - general fracture surface, $\Delta K = 24$ MNm$^{-3/2}$; (b) - striations observed near the end of the fracture surface, $\Delta K = 42$ MNm$^{-3/2}$. Crack propagation is from bottom to top.